hexagon:2611.01076v1

Spectral Fluctuations and Occupation Memory in the Mass-Deformed SYK Model

Zhenyu Sun

November 19, 2026

Abstract

In the mass-deformed Sachdev–Ye–Kitaev model, fluctuations in the norms of the quadratic and quartic couplings change both the spectral width and the effective deformation. Fixing these norms removes the order-t^4 variance of the normalized, unfiltered trace. At fixed even $N \geq 14$ we compute the surviving t^6 coefficient and the t^8 coefficient at the quadratic endpoint. Nested sampling at $N = 14, 18$ gives a positive estimate of the radius-averaged directional fourth cumulant of the filtered trace at $\kappa = 4$ and $t = 4, 16$. Radial averaging gives a convolution in log coupling for scale-invariant observables, with a derivative bound sharp over all bounded responses. For the fixed-radius spacing ratio, the half-response coupling increases from 8.46 at $N = 10$ to 29.29 at $N = 22$.

For quadratic normal-mode charges, dephasing determines the conserved weight, and two exact frequency moments bound the Laplace-averaged inelastic memory. In an isolated-pair ensemble with a regular detuning density at resonance, the mean elastic deficit is asymptotic to a constant times κ^{-1}. The inelastic curvature time grows as $\kappa^{1/2}$, while the time to a fixed fractional loss is of order κ. In the full model at $N = 22$, summing the pair contributions gives 97.1% of the measured elastic deficit at $\kappa = 2048$. At $\kappa = 64$ the normalized inelastic memory differs from the pair prediction by about 0.20 at an intermediate time.

Contents

1 Introduction **3**
1.1 Spectral fluctuations at fixed coupling norms 3
1.2 Charge memory near the quadratic limit 4

2 Model and spectral observables **5**
2.1 Clifford normalization and symmetry blocks 5
2.2 Windows, traces, and reference quantities 6

3 Radial disorder and the effective interaction **7**
3.1 Exact change of variables 7
3.2 An exact smoothing law for crossover curves 8

4 Radial fluctuations and spectral cumulants **9**
4.1 Conditional covariance and fourth cumulants 9

5 The leading fluctuation after radial conditioning **11**
5.1 A closed radial contribution to the residual fourth cumulant 12
5.2 Direct check from the cubic spectral moment 13

6 Nested estimates of spectral cumulants **14**
6.1 Independent outer blocks and unbiased component estimates 14
6.2 Directional fourth cumulants after conditioning 15
6.3 Two-time conditional fluctuations 16

7 Spectral-moment refinement beyond the coupling radii **17**
7.1 A complete hierarchy of spectral residuals 17
7.2 Short-time order after moment conditioning 19
7.3 An exact quadratic endpoint and a joint limit 20
7.4 Independent projection onto smooth moments 21
7.5 What the held-out spectra resolve 22

8 Radial susceptibility and refined crossover curves **24**
8.1 Exact susceptibility and a variance bound 24
8.2 Response normalization and size comparison 25
8.3 A direct radial estimator 26
8.4 Refining the directional crossing grid 26
8.5 Results and finite-size interpretation 27

9 Quadratic charges and their initial time scale **29**

10 Quadratic charge memory and its conserved components **29**
10.1 Exact separation of conserved components 30
10.2 Numerical protocol and verification 31
10.3 Elastic weights and resolved losses of memory 32

11 Frequency moments and a monotone memory diagnostic **34**
11.1 Positive time averaging and moment bounds 36

12 Resolved resonances and the time scale of residual memory **38**
12.1 Exact pair weights and a local isolation criterion 38
12.2 An averaging theorem and two distinct time scales 39
12.3 Paired full-model tests and their limits 42

13 Discussion **44**

A Radial width fluctuations and short-time baselines **45**
A.1 Width fluctuations and their own crossover 45
A.2 Exact short-time spectral fluctuations 46
A.3 Several interaction orders 47

B Conditional means, cumulant estimators, and spectral covariance **47**
B.1 Conditional means and globally centered traces 47
B.2 Unbiased second- and fourth-order estimators 48
B.3 A common covariance measure for spectral statistics 50

C Exact initial state and operator scales **51**

D Spectral weights and conditional state references **54**
D.1 A common energy window for spectral and Fock observables 54
D.2 What a state Lanczos chain determines 56

E Finite-depth stability under changes of spectral weights **57**

F Baseline paired radius calculations **58**
F.1 Sampling design and estimators 58
F.2 The radial contribution at short times 59
F.3 Filtered spectral variance and fourth cumulants 60
F.4 Local spectral comparison and endpoint calibration 60
F.5 A conditional Gaussian control 62

G Independent numerical checks **63**

H Coarse-grid crossover and finite-size drift **63**
H.1 Paired computation and operational crossings 64
H.2 Radial spread relative to the directional width 66

I Directional drift and interpolation resolution **67**

J Nonresonant expansion of the elastic weight **67**

References **69**

1 Introduction

The mass-deformed Sachdev–Ye–Kitaev (SYK) Hamiltonian interpolates between random quartic and quadratic interactions. Even when the relative strength of the two interactions is fixed in the ensemble, each realization has its own spectral width and effective coupling. How much of the variation in a spectral trace comes from these two quantities? A second question arises near the quadratic limit, where the occupations of the quadratic normal modes are almost conserved: how long does the part of a charge orthogonal to its conserved component retain memory?

Level statistics and out-of-time-order correlators probe the chaotic–integrable crossover [Gar+18]. Unfolded and energy-filtered spectral form factors detect changes on different coupling scales [NRY18], and even the quadratic model exhibits an exponential ramp [WJS20]. In the quartic model, fluctuations of the overall density and its smooth modes contribute to long-range spectral correlations [JV20; Ber+21]. Higher moments of the spectral form factor also depend on fluctuations near the spectral edge [LT25]. These results make the choice of energy filter and the information held fixed important for interpreting a measured fourth cumulant.

1.1 Spectral fluctuations at fixed coupling norms

Write $H_\kappa = (A + \kappa B)/\sqrt{1+\kappa^2}$, with quartic part A and quadratic part B. Let R_4 and R_2 denote the norms of their Gaussian coefficient vectors in units of their root-mean-square norms.

The fixed-radius Hamiltonian H_u° uses the same directions and unit radii. Sample by sample,

$$H_\kappa = s_\kappa H^\circ_{\kappa R_2/R_4}, \qquad s_\kappa^2 = \frac{R_4^2 + \kappa^2 R_2^2}{1+\kappa^2}.$$

Dividing by s_κ removes the change of width. The shift $\eta = \log(R_2/R_4)$ in log coupling remains. For scale-invariant observables this gives a convolution with a known density. Its score, the logarithmic derivative of that density, expresses the slope of the ensemble response in terms of radial fluctuations at fixed directions (Theorem 8.1).

For the unfiltered trace, the random width accounts for the order-t^4 variance. Once the radii are fixed, two uncorrelated cubic Clifford invariants determine the t^6 coefficient for even $N \geq 14$. At the quadratic endpoint the cubic trace vanishes and the variance starts at order t^8. Both coefficients enter the limit $t = \theta/\kappa$, $\kappa \to \infty$, at fixed N. For a filtered trace, the energy window alone can produce variance at $t = 0$. We estimate its fourth cumulant by sampling independent angular directions at each of 192 radius pairs across two sizes. At $\kappa = 4$ and $t = 4, 16$, the pointwise 95% intervals for the mean conditional fourth cumulant lie above zero at both sizes. A separate regression on the third through sixth spectral moments explains about 84% and 89% of the held-out filtered-trace variance at $t = 0$ and $\kappa = 4$ for $N = 14, 18$, respectively. Its residual measures the error of that particular predictor.

For the central adjacent-gap ratio, we normalize the crossover by the measured quartic and quadratic endpoints. On the refined grid, the fixed-radius half-response couplings are $8.46, 11.85, 20.45, 29.29$ at $N = 10, 14, 18, 22$. The interquartile width in log coupling grows from 0.905 to 1.333 between $N = 10$ and 18. At $N = 22$ it is 1.339, and the interval for the last width difference includes zero.

1.2 Charge memory near the quadratic limit

A charge autocorrelation also depends on transition matrix elements. Fock-space models relate eigenstate structure to spectral statistics [Mon+21]. Delayed thermalization has been observed in mass-deformed SYK [Nan+22], and finite-size prethermalization in a number-conserving complex-fermion variant [DB23]. We follow the occupations of the quadratic normal modes in one parity block. Projection onto the Hamiltonian gives one conserved component [Maz69; Suz71]. Projection onto all energy-diagonal blocks gives the full time-averaged weight. After subtracting this weight, the second and fourth frequency moments bound the exponentially averaged memory.

Near a resonance, a small quartic matrix element can mix two occupations strongly enough to invalidate a fixed-sample perturbation expansion. We solve the isolated-pair problem and average over a detuning distribution under explicit hypotheses. Its normalized inelastic curvature time is of order $\sqrt{\kappa}$, while the first loss of any fixed fraction between zero and one takes time of order κ. We compare the sum of the pair predictions with full-model dephasing and dynamics on 672 disorder realizations. At $N = 22$, the predicted fraction of the elastic deficit increases from 0.886 at $\kappa = 64$ to 0.971 at $\kappa = 2048$. The dynamical comparison at $\kappa = 64$ still shows a discrepancy of 0.20 on the sampled time grid.

Appendices D and E give Haar-state references and finite-depth Lanczos estimates for comparing different choices of initial state. This dependence on the state is relevant to Krylov diagnostics of deformed SYK and quantum chaos [Bag+25; Cha+25; Che+25; BMW25; HJP24; Erd+26].

2 Model and spectral observables

2.1 Clifford normalization and symmetry blocks

Let $N \geq 10$ be even, and let

$$\{\chi_i, \chi_j\} = \delta_{ij}, \qquad \chi_i^\dagger = \chi_i.$$

The full Hilbert space has dimension $2^{N/2}$. Fermion parity is

$$\mathcal{P} = (-2i)^{N/2}\chi_1 \cdots \chi_N, \qquad P_\pm = (I \pm \mathcal{P})/2.$$

Both interaction terms preserve the two parity blocks. We work in one block of dimension $D = 2^{N/2-1}$, with

$$\mathrm{Tr}_D = \text{ordinary block trace}, \qquad \mathrm{tr}_D = D^{-1}\,\mathrm{Tr}_D, \qquad \|X\|_{\mathrm{HS}}^2 = \mathrm{tr}_D(X^\dagger X).$$

For increasing index sets define the Hermitian involutions

$$\Gamma_I^{(4)} = 4\prod_{i\in I}\chi_i, \qquad |I| = 4, \qquad \Gamma_J^{(2)} = 2i\prod_{j\in J}\chi_j, \qquad |J| = 2.$$

Products within either degree and between the two degrees have normalized block trace zero unless the two monomials coincide. Indeed, their symmetric difference has degree at most eight, and a nonidentity Clifford monomial has zero full trace. Its block trace can differ only when multiplication by $\mathcal{P}$ makes it the identity, which would require a symmetric difference of size N. Thus these monomials are orthonormal in either parity block.

With the independent standard Gaussian coefficients in (3.1), define

$$H_\kappa = \frac{A + \kappa B}{\sqrt{1+\kappa^2}}, \qquad 0 \leq \kappa < \infty, \qquad H_\infty = B. \tag{2.1}$$

The normalization gives $\mathbb{E}\,\mathrm{tr}_D\, A^2 = \mathbb{E}\,\mathrm{tr}_D\, B^2 = 1$. It is an ensemble normalization, leaving individual widths random.

For comparison with the conventional bare couplings

$$H_4^{(0)} = \sum_{i<j<k<l} J_{ijkl}\chi_i\chi_j\chi_k\chi_l, \quad H_2^{(0)} = i\sum_{i<j} K_{ij}\chi_i\chi_j,$$

with $\mathbb{E}J_{ijkl}^2 = 6J^2/N^3$ and $\mathbb{E}K_{ij}^2 = K^2/N$, the corresponding ensemble rms widths are

$$v_4^2 = \frac{J^2(N-1)(N-2)(N-3)}{64N^2}, \qquad v_2^2 = \frac{K^2(N-1)}{8}. \tag{2.2}$$

Our A, B have the same joint law as $H_4^{(0)}/v_4, H_2^{(0)}/v_2$. Consequently,

$$H_\kappa = \frac{H_4^{(0)} + \kappa_{\mathrm{bare}}H_2^{(0)}}{v_4\sqrt{1+\kappa^2}}, \qquad \kappa_{\mathrm{bare}} = \kappa v_4/v_2.$$

Times and temperatures must be converted by the same overall energy factor.

At $\kappa = 0$, the familiar N mod 8 classification gives GOE, GUE, GSE, and GUE for N mod $8 = 0, 2, 4, 6$, respectively, in the symmetry-resolved blocks [YLX17]. The Clifford antiunitary T satisfies

$$\mathsf{T}A\mathsf{T}^{-1} = A, \qquad \mathsf{T}B\mathsf{T}^{-1} = -B.$$

It maps H_κ to $H_{-\kappa}$, so it is generally not a symmetry of a fixed nonzero-κ sample. The classes $N \bmod 8 = 0, 4$ therefore have an additional symmetry crossover; protected quartic-endpoint doublets must not be removed after they split [NRY18]. The numerical sizes $10, 14, 18, 22$ all have a GUE quartic block and avoid that extra crossover. This symmetry classification specifies the chaotic reference class, not the actual level statistics of every deformed sample.

2.2 Windows, traces, and reference quantities

For ordered block eigenvalues $E_1 \le \cdots \le E_D$, define

$$r_j = \frac{\min(E_{j+1} - E_j, E_j - E_{j-1})}{\max(E_{j+1} - E_j, E_j - E_{j-1})}.$$

All three levels must lie in the chosen window. We average first within a sample and then over independent disorder samples. The principal numerical window is the central half by rank. It is invariant under an overall positive energy rescaling. Atas et al. give reference distributions for spacing ratios [Ata+13]. A finite-size comparison also depends on the window and symmetry block.

For a nonnegative spectral filter, the amplitude and its connected form factor are

$$Z_f(t) = \mathrm{Tr}_D[f(H)e^{-itH}], \qquad K_f^c(t) = \frac{\mathrm{Var}_{\mathbb{C}}\, Z_f(t)}{\mathbb{E}\,\mathrm{Tr}_D\, f(H)^2}. \tag{2.3}$$

The denominator is a population mean. This convention is kept fixed when taking higher moments. A physical Gaussian filter is $f(E) = \exp[-E^2/(2\sigma_f^2)]$; a sample-width filter instead uses $f(H/s_\kappa)$. Equations (3.5) and (4.11) specify their different radial transformations.

Long-range comparisons can use unfolded coordinates $x_j = \overline{\mathcal{N}}(E_j)$, provided the smooth counting function and its fitting scale are fixed independently of the claimed crossover. Number-variance centers are sampled independently of the eigenvalues, and the expected local count is retained if the unfolded mean density is not constant. Proposition B.4 gives the finite-window relation to spectral covariance. Our numerical results below avoid fitting a Thouless time and require no unfolding.

The exact quadratic trace provides another reference. In normal modes,

$$B = \sum_{a=1}^{N/2} \epsilon_a (n_a - \tfrac{1}{2}).$$

With parity orientation fixed consistently, its block traces are

$$Z_\pm(t) = \frac{1}{2}\left[\prod_a 2\cos\frac{\epsilon_a t}{2} \;\pm\; \prod_a 2i\sin\frac{\epsilon_a t}{2}\right]. \tag{2.4}$$

This follows by inserting $P_\pm$ and factorizing the occupation sums. For $f_{\mu,\Delta}(E) = \exp[-(E-\mu)^2/(2\Delta^2)]$,

$$Z_{\pm,f}(t) = \frac{\Delta}{\sqrt{2\pi}} \int_{\mathbb{R}} e^{-\Delta^2 u^2/2 + i\mu u} Z_\pm(t+u)\, du. \tag{2.5}$$

The Fourier representation of the Gaussian proves this identity by interchanging the finite spectral sum with the integral. The orientation sign in (2.4) changes if the normal-mode transformation reverses parity orientation. It has no effect on the full-space factorization, but it must be retained when assigning block labels.

3 Radial disorder and the effective interaction

The coefficients of a Gaussian Hamiltonian fluctuate both in direction and in length. In a homogeneous SYK ensemble the latter changes the overall energy scale. With two interaction orders, the two lengths also change their relative strength. This distinction remains relevant after each spectrum is divided by its own standard deviation.

3.1 Exact change of variables

Put $d_q = \binom{N}{q}$, and write

$$A = \frac{1}{\sqrt{d_4}} \sum_{|I|=4} g_I \Gamma_I^{(4)}, \qquad B = \frac{1}{\sqrt{d_2}} \sum_{|J|=2} h_J \Gamma_J^{(2)}, \tag{3.1}$$

where all g_I, h_J are independent standard real Gaussians. The Clifford monomials and the normalized block trace tr_D are specified in Section 2. Define

$$R_4^2 = \frac{1}{d_4} \sum_I g_I^2, \quad R_2^2 = \frac{1}{d_2} \sum_J h_J^2, \quad A^\circ = A/R_4, \quad B^\circ = B/R_2, \quad H_u^\circ = \frac{A^\circ + uB^\circ}{\sqrt{1+u^2}}. \tag{3.2}$$

All radii are positive almost surely. The superscript $\circ$ denotes the ensemble in which the two coupling vectors have fixed lengths.

Theorem 3.1 (Radial representation)**.** *Let $N \geq 10$ be even, and fix one parity block. The pair (R_4, R_2) is independent of (A°, B°), and*

$$d_q R_q^2 \sim \chi_{d_q}^2, \qquad q = 2, 4,$$

independently. For every realization with positive radii, an event of probability one, and $0 \leq \kappa < \infty$,

$$s_\kappa^2 := \mathrm{tr}_D\, H_\kappa^2 = \frac{R_4^2 + \kappa^2 R_2^2}{1+\kappa^2}, \qquad H_\kappa = s_\kappa H_{u_\kappa}^\circ, \qquad u_\kappa = \kappa R_2/R_4. \tag{3.3}$$

In particular, dividing by the sample width removes s_κ and leaves the random effective coupling u_κ.

Proof. Gaussian polar coordinates make each radius independent of its uniformly distributed direction on the corresponding Euclidean sphere. Independence between the two coupling families gives the joint assertion. Orthogonality of the degree-two and degree-four Clifford monomials in the block implies $\mathrm{tr}_D\, A^2 = R_4^2$, $\mathrm{tr}_D\, B^2 = R_2^2$, and $\mathrm{tr}_D\, AB = 0$. This proves the first identity. Substitution of $A = R_4 A^\circ$ and $B = R_2 B^\circ$, followed by division by $\sqrt{R_4^2 + \kappa^2 R_2^2}$, gives the remaining identities. □

The restriction on N ensures blockwise orthogonality without exceptional complementary Clifford monomials. The full-space version only requires the corresponding full-space trace identities. At the endpoints, $H_0 = R_4 A^\circ$ and $H_\infty = R_2 B^\circ$.

For a deterministic filter $f : \mathbb{R} \to \mathbb{C}$, introduce the sample-width-filtered amplitude

$$Z_{\kappa,f}^{\mathrm{sw}}(t) = \mathrm{Tr}_D\left[f(H_\kappa/s_\kappa) e^{-itH_\kappa}\right], \qquad Z_{u,f}^\circ(t) = \mathrm{Tr}_D\left[f(H_u^\circ) e^{-itH_u^\circ}\right]. \tag{3.4}$$

The sample identity is

$$Z^{\mathrm{SW}}_{\kappa,f}(t) = Z^{\circ}_{u_\kappa,f}(s_\kappa t). \tag{3.5}$$

For a fixed physical-energy filter, the corresponding identity instead uses $f_s(E) = f(s_\kappa E)$ on the right-hand side. Thus the filter convention and the time convention enter separately. Appendix F uses a fixed physical-energy Gaussian filter and also records unfiltered short-time amplitudes.

3.2 An exact smoothing law for crossover curves

An observable $O(H)$ is scale invariant if $O(cH) = O(H)$ for $c > 0$. Spacing ratios and spectral statistics defined by scale-equivariant unfolding have this property. A fixed physical-energy window generally does not. For $x \in \mathbb{R}$, set

$$F_{\mathrm{G}}(x) = \mathbb{E}O(H_{e^x}), \qquad F_\circ(x) = \mathbb{E}_\circ O(H^\circ_{e^x}), \qquad \eta = \log R_2 - \log R_4.$$

Theorem 3.2 (Random-coupling convolution)**.** *Whenever the displayed expectations exist,*

$$F_{\mathrm{G}}(x) = \mathbb{E}_\eta F_\circ(x + \eta). \tag{3.6}$$

The same η shifts the entire logarithmic-coupling curve of a paired sample. With the analytic logarithm chosen to vanish at zero, its cumulant generating function is

$$\log \mathbb{E}e^{z\eta} = \frac{z}{2}\log\frac{d_4}{d_2} + \log\frac{\Gamma((d_2+z)/2)}{\Gamma(d_2/2)} + \log\frac{\Gamma((d_4-z)/2)}{\Gamma(d_4/2)}, \qquad -d_2 < \operatorname{Re} z < d_4. \tag{3.7}$$

Writing ψ and ψ_1 for the digamma and trigamma functions,

$$m_\eta := \mathbb{E}\eta = \frac{1}{2}\left[\psi(d_2/2) - \log(d_2/2) - \psi(d_4/2) + \log(d_4/2)\right], \tag{3.8}$$

$$v_\eta := \operatorname{Var}(\eta) = \frac{1}{4}\left[\psi_1(d_2/2) + \psi_1(d_4/2)\right]. \tag{3.9}$$

If $F_\circ \in C^2(\mathbb{R})$ has bounded second derivative, then

$$\sup_x |F_{\mathrm{G}}(x) - F_\circ(x + m_\eta)| \le \frac{1}{2} v_\eta \|F_\circ''\|_\infty. \tag{3.10}$$

Moreover, convolution in (3.6) is injective on integrable response curves.

Proof. Scale invariance and Theorem 3.1 give $O(H_{e^x}) = O(H^\circ_{e^{x+\eta}})$. Conditioning on the independent radii proves (3.6). For $R_q^2 \sim \mathrm{Gamma}(d_q/2, 2/d_q)$,

$$\mathbb{E}R_q^z = (2/d_q)^{z/2}\frac{\Gamma((d_q+z)/2)}{\Gamma(d_q/2)}, \qquad \operatorname{Re} z > -d_q.$$

Multiplying $\mathbb{E}R_2^z$ and $\mathbb{E}R_4^{-z}$ proves (3.7); differentiating at zero proves (3.8)–(3.9). Taylor's theorem about $x+m_\eta$, followed by expectation, gives (3.10); the linear term has zero expectation. Finally, the characteristic function $\mathbb{E}e^{i\omega\eta}$ is a product of gamma factors and a nonzero phase. The gamma function has no zeros and has no poles at the arguments occurring here. The multiplier is therefore nonzero for every real ω. Fourier transformation and uniqueness of the Fourier transform on L^1 prove injectivity. □

Injectivity concerns exact response curves over the whole real line. It does not provide a stable numerical deconvolution from finitely many noisy values. For a bounded, locally absolutely continuous crossover curve with derivative in $L^1(\mathbb{R})$, the same Fourier argument applies to that derivative; a specified endpoint limit fixes the integration constant. The size of the random displacement is

$$v_\eta = \frac{1}{2d_2} + \frac{1}{2d_4} + O(d_2^{-2} + d_4^{-2}) = N^{-2} + O(N^{-3}). \tag{3.11}$$

Consequently, the rms displacement in $\log \kappa$ is of order N^{-1}. This term is fixed by the coupling ensemble and can be separated from the directional spectral response.

4 Radial fluctuations and spectral cumulants

The radial representation of Theorem 3.1 distinguishes fluctuations of the coupling norms from fluctuations of their directions. This distinction extends to the full distribution of a filtered spectral trace. We give exact second- and fourth-order identities for this extension, together with finite-sample estimators. The underlying Gaussian and cumulant identities are classical [Iss18; Bri69; Spe86]; their role here is to separate specific sources of fluctuations in the deformed SYK ensemble.

4.1 Conditional covariance and fourth cumulants

Let

$$Z(t) = \sum_{\alpha=1}^{D} f_\alpha e^{-itE_\alpha}, \qquad 0 \le f_\alpha \le 1, \tag{4.1}$$

in a fixed parity block. The weights may depend measurably on the sample, as they do for windows defined using the sample center and width. Consequently all moments used below exist at finite D. An overall deterministic normalization of Z does not affect the normalized quantities defined below.

For a centered complex random field $Y(t)$, define its covariance and pseudocovariance by

$$C_Y(t,u) = \mathbb{E}[Y(t)\overline{Y(u)}], \qquad P_Y(t,u) = \mathbb{E}[Y(t)Y(u)]. \tag{4.2}$$

The fourth joint amplitude cumulant associated with the two intensities is

$$\begin{aligned} Q_Y(t,u) = \mathbb{E}[|Y(t)|^2|Y(u)|^2] - C_Y(t,t)C_Y(u,u) \\ - |C_Y(t,u)|^2 - |P_Y(t,u)|^2. \end{aligned} \tag{4.3}$$

In particular,

$$Q_Y(t,t) = \mathbb{E}|Y(t)|^4 - 2C_Y(t,t)^2 - |P_Y(t,t)|^2. \tag{4.4}$$

The pseudocovariance is needed even at infinite temperature: a complex trace need not have a circularly symmetric distribution. For every centered jointly complex Gaussian field, including a noncircular one, the real Gaussian pairing formula gives $Q_Y(t,u) = 0$. Vanishing of the fourth cumulants is a necessary condition for this Gaussian description, and does not characterize the whole distribution.

Let $\mathcal{G}$ be a sub-σ-algebra representing specified coarse information about a disorder realization, and set

$$m_{\mathcal{G}}(t) = \mathbb{E}[Z(t) \mid \mathcal{G}], \qquad R(t) = Z(t) - m_{\mathcal{G}}(t). \tag{4.5}$$

Define the random conditional quantities

$$\begin{aligned} C_{\mathcal{G}}(t,u) &= \mathbb{E}[R(t)\overline{R(u)} \mid \mathcal{G}], \\ P_{\mathcal{G}}(t,u) &= \mathbb{E}[R(t)R(u) \mid \mathcal{G}], \qquad c_{\mathcal{G}}(t) = C_{\mathcal{G}}(t,t), \\ Q_{\mathcal{G}}(t,u) &= \mathbb{E}[|R(t)|^2|R(u)|^2 \mid \mathcal{G}] - c_{\mathcal{G}}(t)c_{\mathcal{G}}(u) \\ &\quad - |C_{\mathcal{G}}(t,u)|^2 - |P_{\mathcal{G}}(t,u)|^2. \end{aligned} \tag{4.6}$$

For a complex random variable V, write $\mathrm{Var}_{\mathbb{C}}(V) = \mathbb{E}|V - \mathbb{E}V|^2$.

Theorem 4.1 (Conditional decomposition of spectral fluctuations)**.** *Suppose $Z(t)$ and $Z(u)$ have finite fourth moments. Then*

$$C_R(t,u) = \mathbb{E}C_{\mathcal{G}}(t,u), \qquad P_R(t,u) = \mathbb{E}P_{\mathcal{G}}(t,u), \tag{4.7}$$

$$\begin{aligned} Q_R(t,u) &= \mathbb{E}Q_{\mathcal{G}}(t,u) + \mathrm{Cov}\big(c_{\mathcal{G}}(t), c_{\mathcal{G}}(u)\big) \\ &\quad + \mathrm{Var}_{\mathbb{C}}\big(C_{\mathcal{G}}(t,u)\big) + \mathrm{Var}_{\mathbb{C}}\big(P_{\mathcal{G}}(t,u)\big). \end{aligned} \tag{4.8}$$

At equal times this becomes

$$Q_R(t,t) = \mathbb{E}Q_{\mathcal{G}}(t,t) + 2\,\mathrm{Var}\big(c_{\mathcal{G}}(t)\big) + \mathrm{Var}_{\mathbb{C}}\big(P_{\mathcal{G}}(t,t)\big). \tag{4.9}$$

Proof. The tower property gives (4.7). Taking expectations in the definition of $Q_{\mathcal{G}}$ yields

$$\begin{aligned} \mathbb{E}[|R(t)|^2|R(u)|^2] &= \mathbb{E}Q_{\mathcal{G}}(t,u) + \mathbb{E}[c_{\mathcal{G}}(t)c_{\mathcal{G}}(u)] \\ &\quad + \mathbb{E}|C_{\mathcal{G}}(t,u)|^2 + \mathbb{E}|P_{\mathcal{G}}(t,u)|^2. \end{aligned}$$

Subtract the three products in (4.3), using (4.7). The resulting differences are exactly the covariance and the two complex variances in (4.8). At $t = u$, the covariance term and the variance of $C_{\mathcal{G}}(t,t)$ coincide. □

The theorem separates a conditional fourth cumulant from the effect of mixing conditional second moments. If the conditional field is Gaussian, then $Q_{\mathcal{G}} = 0$, but $Q_R(t,t)$ can be positive. Conversely, $Q_R(t,t) < 0$ excludes every description of $R(t)$ as a mixture of centered complex Gaussians with the stated conditioning. This one-sided statement concerns equal times; the covariance term in (4.8) can be negative for $t \neq u$. For a finite-dimensional random-matrix reference ensemble, its own fourth cumulant is retained when making numerical comparisons.

Corollary 4.2 (Radial specialization)**.** *Assume the radial representation*

$$H_\kappa = s_\kappa H^\circ_{u_\kappa}, \qquad u_\kappa = \kappa R_2/R_4, \tag{4.10}$$

of Theorem 3.1, where the directions defining H° are independent of (R_2, R_4). Suppose both ensembles use the same measurable weight function of the ordered spectrum, with auxiliary parameters fixed. The function has no additional explicit dependence on the nominal coupling or the radii and is invariant under a common positive rescaling of all energies. Let $C^\circ, P^\circ, Q^\circ$ be the centered directional-ensemble quantities at a fixed deformation parameter. With $\mathcal{G} = \sigma(R_2, R_4)$, the conditional quantities in Theorem 4.1 are exactly

$$\begin{aligned} C_{\mathcal{G}}(t,u) &= C^\circ(s_\kappa t, s_\kappa u; u_\kappa), \\ P_{\mathcal{G}}(t,u) &= P^\circ(s_\kappa t, s_\kappa u; u_\kappa), \\ Q_{\mathcal{G}}(t,u) &= Q^\circ(s_\kappa t, s_\kappa u; u_\kappa). \end{aligned} \tag{4.11}$$

In particular,

$$\begin{aligned} Q_R(t,t) = \mathbb{E}Q^\circ(s_\kappa t, s_\kappa t; u_\kappa) \\ + 2\,\mathrm{Var}\big(C^\circ(s_\kappa t, s_\kappa t; u_\kappa)\big) \\ + \mathrm{Var}_{\mathbb{C}}\big(P^\circ(s_\kappa t, s_\kappa t; u_\kappa)\big). \end{aligned} \tag{4.12}$$

Proof. Multiplication of $H^\circ_{u_\kappa}$ by $s_\kappa > 0$ multiplies every eigenvalue by s_κ and preserves each weight under the assumed window rule. Hence $Z_\kappa(t) = Z^\circ_{u_\kappa}(s_\kappa t)$ for each realization. Conditional on the radii, the only randomness is the independent directional randomness. This proves (4.11); the final identity follows from (4.9). □

Equation (4.12) is a finite-N identity. It involves both a random clock and a random effective deformation. It assumes no Gaussian law for the directional SYK traces. With a filter fixed in physical energy, the same statement holds after replacing the directional filter $f(E)$ by $f(s_\kappa E)$.

5 The leading fluctuation after radial conditioning

Fixing the coefficient radii removes the random quadratic spectral moment. The next fluctuation is determined by a cubic Clifford invariant. Its variance can be evaluated exactly, giving an analytic reference for the directional ensemble before any unfolding or choice of an energy window.

Theorem 5.1 (Directional cubic invariant)**.** *Let $N \geq 14$ be even, and use one parity block. For independent uniform coefficient directions A° and B°, define*

$$X = \mathrm{tr}_D[(A^\circ)^3], \qquad Y = \mathrm{tr}_D\big[A^\circ (B^\circ)^2\big], \qquad a_N = \frac{540\binom{N}{6}}{d_4(d_4+2)(d_4+4)}, \qquad b_N = \frac{12}{d_2(d_2+2)}.$$

Then $\mathrm{tr}_D[(A^\circ)^2 B^\circ] = \mathrm{tr}_D[(B^\circ)^3] = 0$ samplewise, $\mathbb{E}X = \mathbb{E}Y = \mathbb{E}XY = 0$, and

$$\mathbb{E}X^2 = a_N, \qquad \mathbb{E}Y^2 = b_N, \qquad \mathrm{Var}_\circ\big(\mathrm{tr}_D[(H^\circ_u)^3]\big) = \frac{a_N + 9u^4 b_N}{(1+u^2)^3}. \tag{5.1}$$

Consequently the normalized unfiltered trace satisfies

$$C^\circ_z(t) = \frac{t^6}{36}\frac{a_N + 9u^4 b_N}{(1+u^2)^3} + O(t^8). \tag{5.2}$$

Proof. Write $A^\circ = \sum_I u_I \Gamma^{(4)}_I$ and $B^\circ = \sum_J v_J \Gamma^{(2)}_J$, where u and v are independent uniform unit vectors. Products of total degree at most twelve have no complementary contribution to the parity trace for $N \geq 14$. Thus the trace of three quartic monomials can be nonzero only if their index sets satisfy $I \triangle J = K$. The three sets are then distinct, their pairwise intersections have size two, and their union has six elements. Each six-element union has fifteen partitions into three unordered pairs. The unions of pairs specify fifteen unordered triples $\{I, J, K\}$. The three monomials commute pairwise, so all six orders in the cubic trace have the same sign. Hence X is a sum of $15\binom{N}{6}$ distinct monomials of the form $\pm 6 u_I u_J u_K$.

The expectation of a product of two different such terms vanishes by coordinate sign symmetry. For three different coordinates of a uniform vector in $\mathbb{R}^{d_4}$,

$$\mathbb{E}(u_I^2 u_J^2 u_K^2) = \frac{1}{d_4(d_4+2)(d_4+4)}.$$

This proves the formula for a_N. For each quartic index set, the degree-four coefficient of $(B^\circ)^2$ is the sum over its three pairings, with coefficients $\pm 2v_J v_L$. Distinct pairings have zero cross expectation, giving squared mean $12/[d_2(d_2+2)]$ for that coefficient. Averaging $u_I u_K = \delta_{IK}/d_4$ then gives $\mathbb{E}Y^2 = b_N$.

A degree-two coefficient in $(A^\circ)^2$ would require two quartic sets to share three indices. Those monomials anticommute and cancel in the square. The same argument excludes the degree-two coefficient of $(B^\circ)^2$, proving the two vanishing traces. Oddness in u gives $\mathbb{E}X = \mathbb{E}Y = 0$. In XY, the three different u coordinates in a term of X cannot all be paired with the single extra coordinate from Y; the fourth spherical moment therefore vanishes. The cubic trace of H_u° is consequently $(X + 3u^2Y)/(1+u^2)^{3/2}$, proving (5.1). Finally, the centered trace has leading term $it^3 \operatorname{tr}_D[(H_u^\circ)^3]/6$. Its order-four term is real, so it has no order-seven contribution to the modulus squared. Bounded fixed-radius matrix norms justify the stated remainder. □

For fixed nonzero u, the mixed invariant controls the leading size dependence: $a_N \sim 10368N^{-6}$ and $b_N \sim 48N^{-4}$. The two numerator contributions in (5.1) are equal at

$$u_3 = \left(\frac{a_N}{9b_N}\right)^{1/4} \sim 24^{1/4}N^{-1/2}. \tag{5.3}$$

This scale is a property of directional cubic-trace fluctuations. Its constant differs from the width-fluctuation scale in (A.3). At the pure quadratic endpoint the cubic trace vanishes identically and the t^6 coefficient is zero.

5.1 A closed radial contribution to the residual fourth cumulant

Let $\mathcal{G} = \sigma(R_4, R_2)$ and set $\zeta(t) = z_\kappa(t) - \mathbb{E}[z_\kappa(t) \mid \mathcal{G}]$. In this subsection $C_{\mathcal{G},z}$, $P_{\mathcal{G},z}$ and $Q_{\mathcal{G},z}$ denote the conditional cumulants of the normalized unfiltered trace. The unconditional fourth cumulant of ζ is Q_ζ. This keeps the trace normalization separate from that of the filtered amplitudes in Section 4.

Corollary 5.2 (Residual covariance mixing)**.** *Under the hypotheses of Theorem 5.1, define*

$$V_3(R_4, R_2) = \frac{a_N R_4^6 + 9\kappa^4 b_N R_4^2 R_2^4}{(1+\kappa^2)^3}. \tag{5.4}$$

Then $\mathbb{E}[\operatorname{tr}_D(H_\kappa^3) \mid \mathcal{G}] = 0$ *and* $\operatorname{Var}(\operatorname{tr}_D(H_\kappa^3) \mid \mathcal{G}) = V_3$*. In particular,*

$$C_{\mathcal{G},z}(t) = \frac{t^6}{36}V_3 + O(t^8), \qquad P_{\mathcal{G},z}(t) = -\frac{t^6}{36}V_3 + O(t^8), \tag{5.5}$$

$$\mathbb{E}V_3 = \frac{540\binom{N}{6}/d_4^3 + 108\kappa^4/d_2^2}{(1+\kappa^2)^3}, \tag{5.6}$$

$$Q_\zeta(t,t) - \mathbb{E}Q_{\mathcal{G},z}(t,t) = \frac{t^{12}}{432}\operatorname{Var}(V_3) + O(t^{14}). \tag{5.7}$$

The remainder in the first line is integrable over the radii to every fixed finite power needed in the last line.

Proof. Substitution of $A = R_4 A^\circ$ and $B = R_2 B^\circ$ into the cubic trace gives (5.4). The leading centered amplitude is purely imaginary, which accounts for the minus sign in the

pseudocovariance. The symmetry $(A^\circ, B^\circ) \mapsto (-A^\circ, -B^\circ)$ removes its possible order-seven term. Gamma moments give (5.6). The equal-time conditional-cumulant identity (4.9) gives $Q_\zeta - \mathbb{E}Q_{\mathcal{G},z} = 2\,\mathrm{Var}(C_{\mathcal{G},z}) + \mathrm{Var}_{\mathbb{C}}(P_{\mathcal{G},z})$. Inserting the first line yields $3t^{12}\,\mathrm{Var}(V_3)/36^2$. Finite Gaussian matrix moments justify expectation of the Taylor remainders; the same sign symmetry removes odd powers through order thirteen. □

The coefficient in (5.7) has a closed form. Put $M_q(j) = \mathbb{E}(R_q^2)^j = \prod_{\ell=0}^{j-1}(1 + 2\ell/d_q)$, $\alpha = a_N/(1+\kappa^2)^3$, and $\beta = 9\kappa^4 b_N/(1+\kappa^2)^3$. Independence gives

$$\begin{aligned}\mathrm{Var}(V_3) = \alpha^2\{M_4(6) - M_4(3)^2\} \\ + \beta^2\{M_4(2)M_2(4) - M_2(2)^2\} \\ + 2\alpha\beta M_2(2)\{M_4(4) - M_4(3)\}.\end{aligned} \tag{5.8}$$

Thus even after subtracting the conditional mean, a calculable fourth-order contribution remains from the varying conditional variance. The nested experiment below measures the additional directional fourth cumulant itself, including at times outside this Taylor expansion.

5.2 Direct check from the cubic spectral moment

The saved paired spectra give $\mathrm{tr}_D\, H^3$ without a time fit. We estimate its second moment using its exact zero ensemble mean and resample complete disorder draws 1,000 times. Figure 1 compares both predictions in (5.1) and (5.6) with 4,096 paired samples at $N = 14$ and 1,024 at $N = 18$. The pure quadratic cubic trace is zero to numerical precision and is excluded from the ratio plot. All finite-coupling comparisons use the same samples as the original radius comparison; they are a check of a new analytic coefficient, rather than additional independent disorder data.

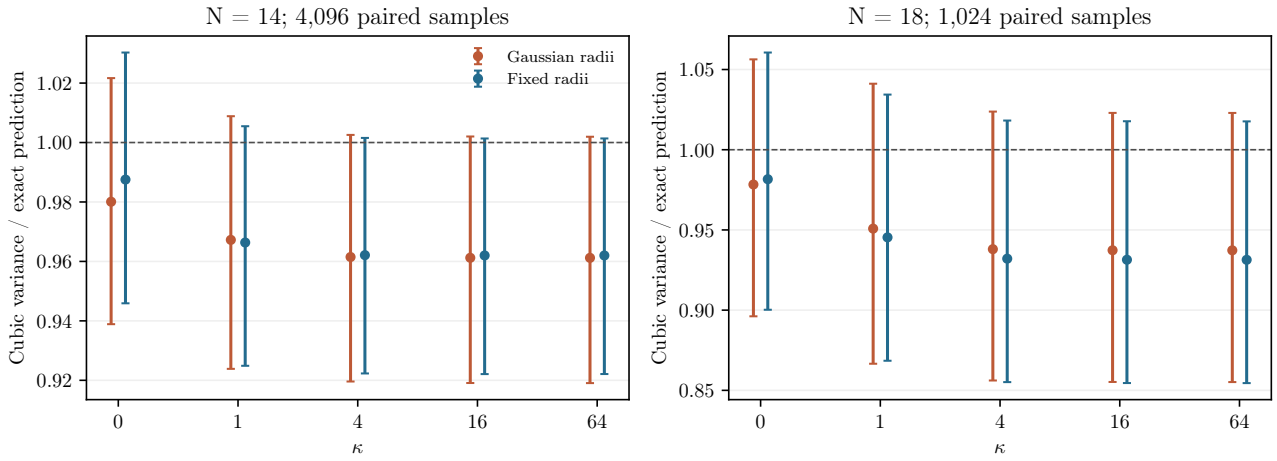


Figure 1: Second moment of the cubic spectral trace divided by its exact prediction. Error bars are pointwise 95% whole-draw bootstrap intervals. The fixed-radius prediction is (5.1); the Gaussian-radius prediction is (5.6). The latter is also the directional variance averaged over radii because the conditional cubic mean vanishes.

6 Nested estimates of spectral cumulants

We now evaluate the conditional decomposition itself. The coarse information is exactly $\mathcal{G} = \sigma(R_2, R_4)$, and the remaining randomness is the pair of independent coupling directions. We retain the fixed physical-energy filter $f(E) = \exp[-E^2/(2\sigma_f^2)]$, $\sigma_f = 0.5$, and the unnormalized trace in the even-parity block. The sampled physical times are

$$0,\ 0.25,\ 0.5,\ 1,\ 2,\ 4,\ 8,\ 16,\ 32,\ 64,\ 128.$$

The time variable is common to all samples. Conditional on the radii, the exact directional representation uses the time $s_\kappa t$, coupling $u_\kappa = \kappa R_2/R_4$, and filter $f(s_\kappa E)$. All three dependencies are retained by directly diagonalizing the physical Hamiltonian.

6.1 Independent outer blocks and unbiased component estimates

At each size we draw independent pairs of radii. At every pair, two independent batches of angular Hamiltonians are generated. The directions are independent across outer blocks as well. Within each inner draw the same directions are used at $\kappa = 0, 4, \infty$ and at every time. The sample counts are

N	Outer blocks B	Inner draws per batch M	Directional draws	Block spectra
14	128	256	65,536	196,608
18	64	128	16,384	49,152

These are 192 independent outer observations; conditional replicates sharing a radial pair are retained as one cluster in unconditional inference.

Let $\widehat{c}_b^{(j)}, \widehat{p}_b^{(j)}, \widehat{q}_b^{(j)}$ be the unbiased covariance, pseudocovariance, and fourth-cumulant estimates in batch $j = 1, 2$ of outer block b. They use Theorem B.2. At a fixed time, write $\langle v \rangle_B = B^{-1} \sum_b v_b$ and define

$$\begin{aligned}
\widehat{D} &= \left\langle (\widehat{q}^{(1)} + \widehat{q}^{(2)})/2 \right\rangle_B, & \widehat{c}_R &= \left\langle (\widehat{c}^{(1)} + \widehat{c}^{(2)})/2 \right\rangle_B, \\
\widehat{V}_C &= \frac{B}{B-1} \left[\langle \widehat{c}^{(1)} \widehat{c}^{(2)} \rangle_B - \langle \widehat{c}^{(1)} \rangle_B \langle \widehat{c}^{(2)} \rangle_B \right], \\
\widehat{V}_P &= \frac{B}{B-1} \operatorname{Re} \left[\langle \widehat{p}^{(1)} \overline{\widehat{p}^{(2)}} \rangle_B - \langle \widehat{p}^{(1)} \rangle_B \overline{\langle \widehat{p}^{(2)} \rangle_B} \right], \\
\widehat{Q}_R &= \widehat{D} + 2\widehat{V}_C + \widehat{V}_P.
\end{aligned} \tag{6.1}$$

Their expectations are respectively $\mathbb{E}Q_{\mathcal{G}}$, $\mathbb{E}c_{\mathcal{G}}$, $\mathrm{Var}(c_{\mathcal{G}})$, $\mathrm{Var}_{\mathbb{C}}(P_{\mathcal{G}})$, and Q_R. The proof is the independent-batch argument in Proposition B.3. The variance-component estimators can be negative at finite sample size; we retain those values.

To estimate the globally centered cumulant Q_Y, independent products must use distinct outer blocks. The following construction uses all inner data while preserving this requirement. For the four labeled variables $(X_1, X_2, X_3, X_4) = (Z, \overline{Z}, Z, \overline{Z})$ and a nonempty subset $A \subset \{1, 2, 3, 4\}$, set

$$\widehat{M}_b(A) = \frac{1}{2M} \sum_{j=1}^{2M} \prod_{\ell \in A} X_{bj,\ell},$$

where the inner observations are pooled from the two batches. For a partition $\pi = \{A_1, \dots, A_r\}$, define

$$\widehat{U}_\pi = \frac{1}{B(B-1)\cdots(B-r+1)} \sum_{b_1,\dots,b_r \text{ distinct}} \prod_{a=1}^{r} \widehat{M}_{b_a}(A_a).$$

Proposition 6.1 (Unconditional cumulants from independent outer blocks)**.** *For $B \geq 4$, the estimator*

$$\widehat{Q}_Y = \sum_{\pi \in \mathcal{P}_4} (-1)^{|\pi|-1}(|\pi|-1)!\, \widehat{U}_\pi \tag{6.2}$$

is unbiased for the globally centered fourth cumulant. The corresponding two-variable formula is unbiased for C_Y and P_Y.

Proof. For each block of the partition, $\mathbb{E}\widehat{M}_b(A) = \mathbb{E}\prod_{\ell \in A} X_\ell$ by conditional expectation. Independence of distinct outer blocks makes $\mathbb{E}\widehat{U}_\pi$ the product of these population moments. The ordinary moment–cumulant identity proves the assertion. This is a cluster implementation of the partition formula for cumulants [Spe86], with one independent outer observation assigned to each factor in a moment product. □

We evaluate the sums using inclusion–exclusion over coincident outer indices, with a common translation of all traces for numerical stability. A finite distribution with unequal conditional means and variances permits an exact check: enumeration of all 4,096 configurations of four outer blocks gives an absolute bias below 2.5×10^{-14}. The same code agrees with the ordinary joint k-statistic when each outer block has one observation. The total conditional-mean correction is estimated by $\widehat{Q}_Y - \widehat{Q}_R$. In particular, no unconditional estimator treats all inner observations as independent disorder samples.

All intervals use 800 resamples of complete outer blocks, retaining both batches and all coupling/time pairings. They are pointwise 95% percentile intervals. The principal normalized directional quantity is

$$q_{\mathrm{dir}}(t) = \frac{\mathbb{E}Q_{\mathcal{G}}(t,t)}{(\mathbb{E}c_{\mathcal{G}}(t))^2}. \tag{6.3}$$

It is a ratio of disorder expectations, not the average of a conditional ratio. Its sample estimate retains ratio bias. We also retain every unnormalized component and its confidence interval.

6.2 Directional fourth cumulants after conditioning

Table 1 gives representative estimates. At $\kappa = 4$, the directional fourth cumulant remains positive and resolved at $t = 4$ and $t = 16$ for both sizes. It therefore survives conditioning on both coefficient norms. At $t = 64$ the pointwise intervals contain zero. These statements concern the specified physical times and filter; the calculation does not align time by a fitted Heisenberg or Thouless scale.

At $N = 14, \kappa = 4, t = 4$, the three contributions to Q_R, divided by $(\mathbb{E}c_{\mathcal{G}})^2$, are approximately

$$0.8098\ [0.7352, 0.8900], \qquad 0.00494\ [0.00256, 0.00764], \qquad 0.00359\ [0.00185, 0.00529],$$

for the directional term, covariance mixing, and pseudocovariance mixing, respectively. Both mixing terms are resolved here, and their magnitude is small compared with the directional fourth cumulant. At $N = 18$ several mixing-component intervals contain zero; their negative point estimates are reported as sampling fluctuations of the unbiased estimator. The resolved

κ	t	q_{dir}, $N = 14$	q_{dir}, $N = 18$
4	0	1.805 [1.453, 2.214]	1.556 [1.228, 1.936]
4	4	0.810 [0.735, 0.890]	1.088 [0.916, 1.286]
4	16	0.264 [0.231, 0.301]	1.176 [0.921, 1.446]
4	64	−0.008 [−0.023, 0.009]	0.014 [−0.017, 0.050]
∞	16	2.980 [2.834, 3.141]	7.963 [6.641, 9.386]
∞	64	3.023 [2.898, 3.149]	8.735 [7.587, 10.025]

Table 1: Directional fourth cumulant divided by the square of the mean conditional covariance. Brackets give pointwise 95% outer-bootstrap intervals. All times are in the same ensemble-normalized physical units.

directional average quantifies a departure from conditional Gaussian fourth-moment factorization. It does not identify a thermodynamic phase or equate finite-dimensional non-Gaussianity with integrability.

The quadratic endpoint retains a much larger directional excess at the sampled later times. At $t = 64$, its estimates are approximately 3.02 for $N = 14$ and 8.73 for $N = 18$. The pure quartic data give much smaller values on the same physical grid. Two sizes and one energy filter do not specify a large-N law; the accompanying tables give the estimates and pointwise intervals.

The covariance scales explain why global and conditional fourth cumulants must be kept separate. At $\kappa = 4, t = 0$, the estimates are

$$\begin{aligned} N = 14: &\quad \mathbb{E}c_{\mathcal{G}} = 0.06715, &\quad C_Y = 2.31998, \\ N = 18: &\quad \mathbb{E}c_{\mathcal{G}} = 0.19528, &\quad C_Y = 21.08620. \end{aligned}$$

The random conditional mean supplies most of the global variance in this filtered early-time comparison. The fourth-order mean correction has much larger uncertainty. For example, at $N = 14, \kappa = 4, t = 0$,

$$\widehat{Q}_R = 0.00819\ [0.00658, 0.01012], \qquad \widehat{Q}_Y - \widehat{Q}_R = -0.666\ [-4.475, 3.057].$$

Here Q_R is the cumulant of the conditionally centered trace. Its interval lies above zero. The interval for the total conditional-mean correction includes zero at $N = 14$. At $N = 18$ and the same t and κ, that correction is -356.1 with interval $[-713.6, -90.5]$, in the unnormalized trace units of the larger block.

6.3 Two-time conditional fluctuations

The same saved traces provide the full two-time identity (4.8) at $t, u \in \{0, 1, 4, 16, 64\}$. We estimate $\mathrm{Cov}(c_{\mathcal{G}}(t), c_{\mathcal{G}}(u))$ by symmetrizing the two independent batches, and estimate the covariance and pseudocovariance variance terms by the corresponding complex cross-products. The diagonal agrees with the separate equal-time calculation to absolute error below 7.3×10^{-12} across both sizes.

Figure 3 displays the directional and residual fourth cumulants divided by $\mathbb{E}c_{\mathcal{G}}(t)\,\mathbb{E}c_{\mathcal{G}}(u)$. At $N = 18$ and $\kappa = 4$, the normalized directional component at $(t, u) = (4, 16)$ is 0.06175 (95% interval $[0.03355, 0.08633]$). The complete conditionally centered quantity is 0.06265 (95%

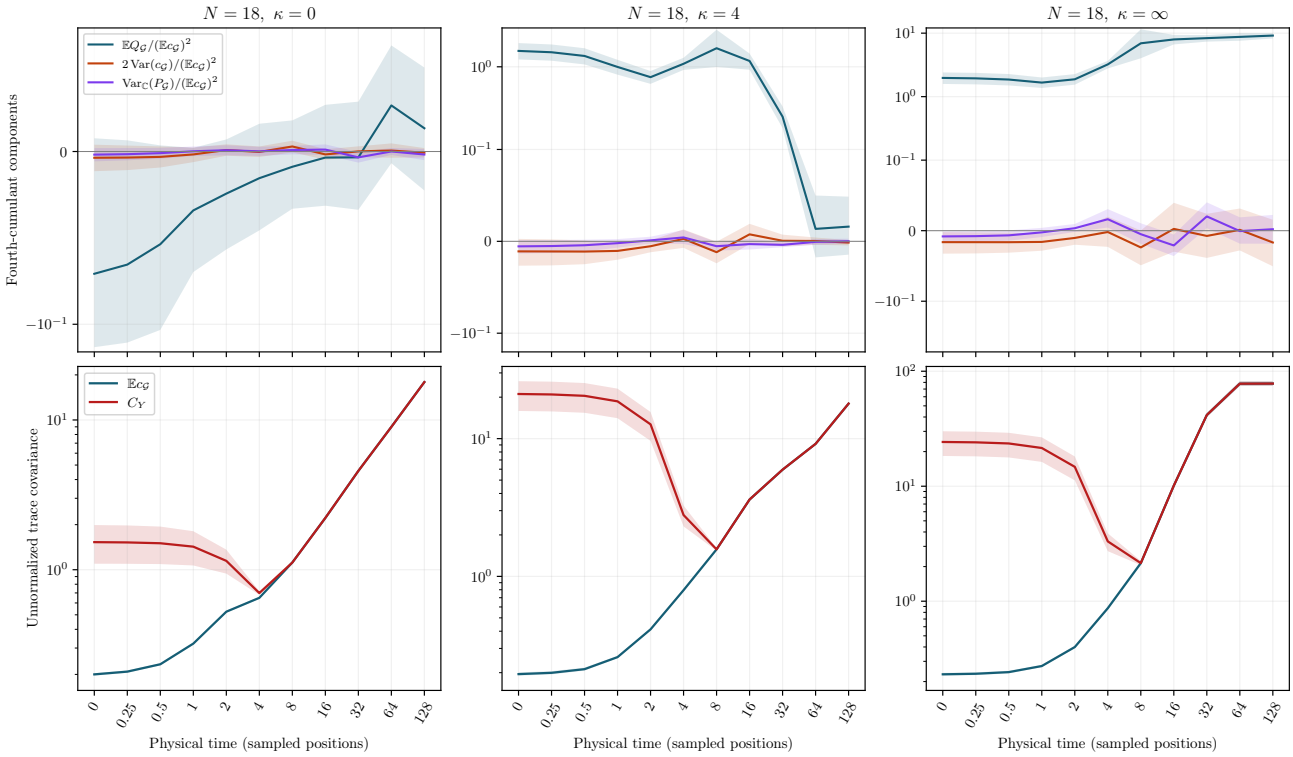


Figure 2: Nested decomposition at $N = 18$. Upper panels show $\mathbb{E}Q_{\mathcal{G}}$, $2\,\mathrm{Var}(c_{\mathcal{G}})$, and $\mathrm{Var}_{\mathbb{C}}(P_{\mathcal{G}})$, each divided by $(\mathbb{E}c_{\mathcal{G}})^2$. Lower panels retain the unnormalized conditional and global covariances. Shading denotes pointwise 95% outer-bootstrap intervals. Horizontal positions enumerate the stated physical times. Upper axes use a symmetric logarithmic scale with a linear neighborhood of zero, so negative unbiased estimates remain visible.

interval $[0.03551, 0.08555]$). The analogous directional interval at $N = 14$ contains zero. These are pointwise comparisons on a preassigned time grid; the markers in the figure do not represent a simultaneous hypothesis test over the map. The calculation adds temporal fourth-order information while preserving the distinction between directional non-Gaussianity, conditional covariance mixing, and the global conditional-mean terms.

7 Spectral-moment refinement beyond the coupling radii

At fixed radii the second spectral moment is deterministic. Conditioning on successive higher moments removes further variance from the trace. The corresponding fourth-cumulant difference also involves mixed terms. To examine these fluctuations numerically, we predict the trace from a finite set of moments and measure the residual on independent samples.

7.1 A complete hierarchy of spectral residuals

At fixed N and κ, work in the fixed-radius ensemble and put

$$m_j = \mathrm{tr}_D[(H_\kappa^\circ)^j], \qquad \mathcal{F}_p = \sigma(m_3, \dots, m_p), \qquad R_p(t) = Z(t) - \mathbb{E}[Z(t) \mid \mathcal{F}_p], \quad p \geq 2. \tag{7.1}$$

Here $\mathcal{F}_2$ is trivial because $m_1 = 0$ and $m_2 = 1$ are deterministic. The trace Z may be filtered or unfiltered. This construction can also start from random radii by adjoining $\sigma(R_4, R_2)$ to every

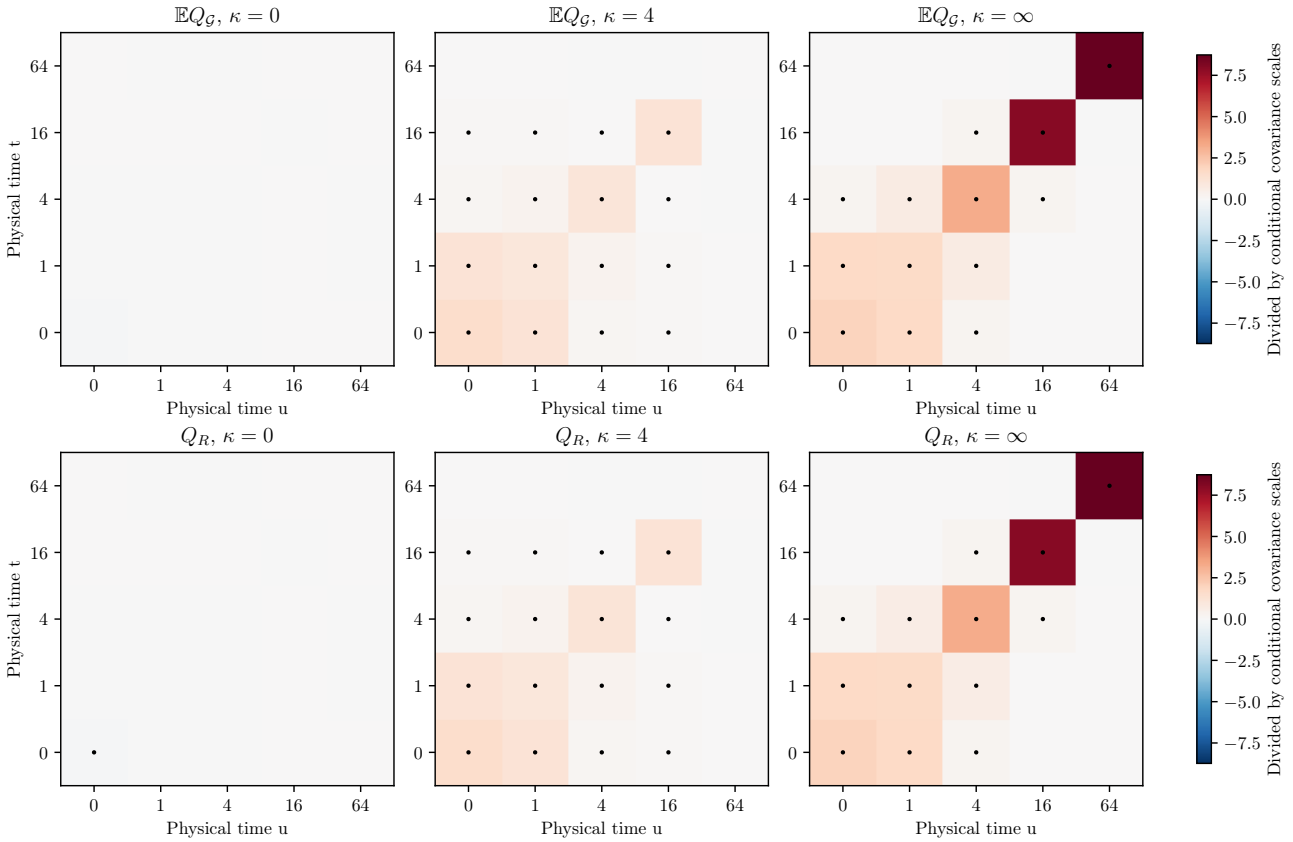


Figure 3: Two-time conditional fourth cumulants at $N = 18$. The upper row shows $\mathbb{E}Q_{\mathcal{G}}(t, u)$ and the lower row $Q_R(t, u)$, both divided by $\mathbb{E}c_{\mathcal{G}}(t)\mathbb{E}c_{\mathcal{G}}(u)$. Each row uses a common color scale across the three couplings. Black dots mark entries whose pointwise 95% outer-bootstrap interval excludes zero; no multiplicity adjustment is applied. These maps concern conditional residuals and do not include the additional random-mean contribution to Q_Y.

$\mathcal{F}_p$.

Proposition 7.1 (Refinement identities)**.** *For $q \geq p$, let $\Delta_{pq}(t) = \mathbb{E}[Z(t) \mid \mathcal{F}_q] - \mathbb{E}[Z(t) \mid \mathcal{F}_p]$. Then*

$$\begin{aligned} C_{R_p}(t, u) &= C_{R_q}(t, u) + C_{\Delta_{pq}}(t, u), \\ P_{R_p}(t, u) &= P_{R_q}(t, u) + P_{\Delta_{pq}}(t, u). \end{aligned} \tag{7.2}$$

In particular, $C_{R_q}(t, t) \leq C_{R_p}(t, t)$. At a single time set $U = \Delta_{pq}$ and

$$c_q = \mathbb{E}[|R_q|^2 \mid \mathcal{F}_q], \quad P_q = \mathbb{E}[R_q^2 \mid \mathcal{F}_q], \quad T_q = \mathbb{E}[R_q|R_q|^2 \mid \mathcal{F}_q].$$

With the bilinear covariance from Appendix B.1, the exact fourth-order difference is

$$Q_{R_p} - Q_{R_q} = Q_U + 4\,\mathrm{Cov}(|U|^2, c_q) + 2\,\mathrm{Re}\,\mathrm{Cov}_b(\overline{U}^2, P_q) + 4\,\mathrm{Re}\,\mathbb{E}[\overline{U}T_q]. \tag{7.3}$$

If the trace weights are measurable functions of the unordered spectrum (with eigenvalues listed in increasing order), then $R_p = 0$ for $p \geq D$.

Proof. The tower property gives $R_p = \Delta_{pq} + R_q$ and $\mathbb{E}[R_q \mid \mathcal{F}_q] = 0$, while Δ_{pq} is $\mathcal{F}_q$-measurable. The mixed second moments therefore vanish, which proves (7.2). Expanding $|U + R_q|^4$ conditionally and subtracting $2C^2 + |P|^2$ gives (7.3), equivalently (B.3) with $A = U$. Finally, the power sums through degree D determine the characteristic polynomial by Newton's identities. They therefore determine the unordered spectrum and any measurable function of it, including Z. □

There is no general fourth-cumulant ordering under refinement. For example, let $Z = S + G$, where G is a standard real Gaussian independent of the centered variable S. Refining the trivial information to $\sigma(S)$ leaves the residual G, whose fourth cumulant vanishes. If S takes the values ± 1 with equal probability, the original cumulant is -2. If S takes each of $\pm\sqrt{5}$ with probability $1/10$ and is zero otherwise, it is 2. In both cases $\operatorname{Var} S = 1$, so normalizing by squared variance preserves the opposite signs. For a spectrum-measurable trace at fixed dimension, the residual eventually vanishes by Proposition 7.1.

7.2 Short-time order after moment conditioning

For the normalized unfiltered trace $z(t) = \operatorname{tr}_D e^{-itH_\kappa^\circ}$, write $R_{p,z} = z - \mathbb{E}[z \mid \mathcal{F}_p]$ and

$$U_{p+1} = m_{p+1} - \mathbb{E}[m_{p+1} \mid \mathcal{F}_p], \qquad v_p = \operatorname{Var}(m_{p+1} \mid \mathcal{F}_p).$$

Let $Q_{\mathcal{F}_p,z}$ denote the conditional fourth cumulant of $R_{p,z}$.

Proposition 7.2 (Leading conditional moment)**.** *For fixed finite N, κ, and $p \geq 2$,*

$$R_{p,z}(t) = \frac{(-it)^{p+1}}{(p+1)!} U_{p+1} + O_{L^r}(t^{p+2}), \qquad 1 \leq r \leq \infty, \tag{7.4}$$

$$C_{R_{p,z}}(t,t) = \frac{t^{2p+2}}{((p+1)!)^2} \mathbb{E} v_p + O(t^{2p+4}), \tag{7.5}$$

$$Q_{R_{p,z}}(t,t) = \frac{t^{4p+4}}{((p+1)!)^4} \left\{ \mathbb{E} U_{p+1}^4 - 3(\mathbb{E} U_{p+1}^2)^2 \right\} + O(t^{4p+6}), \tag{7.6}$$

$$Q_{R_{p,z}}(t,t) - \mathbb{E} Q_{\mathcal{F}_p,z}(t,t) = \frac{3t^{4p+4}}{((p+1)!)^4} \operatorname{Var}(v_p) + O(t^{4p+6}). \tag{7.7}$$

The leading coefficients may vanish, in which case a higher order is required.

Proof. For every realization, $\|H_\kappa^\circ\| \leq (\sqrt{d_4} + \kappa\sqrt{d_2})/\sqrt{1+\kappa^2} \leq L := \sqrt{d_4 + d_2}$. After Taylor expansion through degree $p+1$, the absolute remainder of z is at most $e^{|t|L}(|t|L)^{p+2}/(p+2)!$. Subtracting its conditional expectation multiplies this bound by at most two. All terms of degree at most p are $\mathcal{F}_p$-measurable, which proves (7.4). The next real spectral moment carries an extra factor $-i$, so its cross term in the squared modulus vanishes. More generally, $R_{p,z}(-t) = \overline{R_{p,z}(t)}$, making the covariance and diagonal fourth cumulant even analytic functions of t. Their leading terms give (7.5) and (7.6). Conditionally, the leading covariance is $t^{2p+2} v_p/((p+1)!)^2$ and the leading pseudocovariance is $(-1)^{p+1}$ times this expression. Substitution in (4.9) yields the factor three in (7.7). The uniform Taylor bound justifies all averages and remainders. □

Thus radial conditioning raises the possible leading covariance from order t^4 to at least order t^6, and exact conditioning on the cubic moment raises it to at least order t^8. Further conditioning has a specified analytic effect at each order. These statements concern the unfiltered trace; a fixed physical filter is a function of all spectral moments and does not have the same order of vanishing at $t = 0$.

7.3 An exact quadratic endpoint and a joint limit

The vanishing cubic invariant at the quadratic endpoint permits an additional closed calculation. It provides a model-specific coefficient for the next level of the hierarchy.

Theorem 7.3 (Quadratic fourth-moment fluctuation)**.** *Let $N > 8$ be even and let B° have a uniformly distributed unit coefficient vector in its $d = d_2 = \binom{N}{2}$ quadratic Clifford coordinates. In either parity block,*

$$\mathbb{E}m_4(B^\circ) = 3 - \frac{2(2N-1)}{d+2},$$
$$v_{4,N} := \mathrm{Var}(m_4(B^\circ)) = \frac{128(N-3)(N-2)(N+1)(N+2)}{(N^2-N+4)^2(N^2-N+8)(N^2-N+12)}. \tag{7.8}$$

Consequently,

$$C^\circ_{z,\infty}(t) = \frac{v_{4,N}}{576}t^8 + O(t^{10}). \tag{7.9}$$

Proof. In canonical coordinates write $B^\circ = \sum_{a=1}^{N/2} \lambda_a Q_a$, with commuting involutions Q_a and $\sum_a \lambda_a^2 = 1$. Products of total Clifford degree at most eight have no complementary parity contribution for $N > 8$. Expansion then gives

$$m_4(B^\circ) = 3 - 2s_4, \qquad s_4 = \sum_a \lambda_a^4. \tag{7.10}$$

To average s_4, let G be the real antisymmetric matrix whose entries g_{ij} above the diagonal are independent standard Gaussians, and put $S = \sum_{i<j} g_{ij}^2$ and $W = \frac{1}{2}\operatorname{Tr} G^4$. Radial independence gives $W = S^2 s_4$, with S independent of s_4. Gaussian contraction yields

$$\mathbb{E}W = d(2N-1), \qquad \mathrm{Var}\, W = 24d(3d+1). \tag{7.11}$$

For completeness, view the d independent entries as edges of the complete graph. With $h = d(N-2)$ unordered adjacent edge pairs, $\ell = 2(N-2)$ pairs incident to each edge, and oriented four-cycle signs ϵ_γ, one has

$$W = \sum_e g_e^4 + 2\sum_{\{e,f\}\,\text{adjacent}} g_e^2 g_f^2 + 4\sum_{\gamma\,\text{four-cycle}} \epsilon_\gamma \prod_{e\in\gamma} g_e.$$

The first two summands have means $3d$ and $2h$; the third has mean zero and is orthogonal to both. The variance is

$$96d + 128h + 8d\ell(\ell-1) + 48\binom{N}{4} = 24d(3d+1).$$

This proves (7.11) using only independent Gaussian moments. Since $\mathbb{E}S^2 = d(d+2)$ and $\mathbb{E}S^4 = d(d+2)(d+4)(d+6)$, division of $\mathbb{E}W$ and $\mathbb{E}W^2 = d^2(2N-1)^2 + 24d(3d+1)$ by these radial moments gives $\mathbb{E}s_4$ and $\mathbb{E}s_4^2$. Simplification in (7.10) gives (7.8). Finally $m_3(B^\circ) = 0$, so the centered normalized trace starts with $t^4(m_4 - \mathbb{E}m_4)/24$. The next term has the opposite real/imaginary parity, proving (7.9). □

An exact enumeration of all 105 Wick pairings for $(\operatorname{Tr} G^4)^2$, with the 16 antisymmetric covariance orientations per pairing, independently reproduces (7.11). The saved fixed-radius spectra also check the angular variance directly:

N	Samples	Measured $\mathrm{Var}(m_4)$ [95% interval]	Exact $v_{4,N}$
10	2048	0.010679 [0.009976, 0.011384]	0.0107125
14	4096	0.003178 [0.003001, 0.003370]	0.00317990
18	1024	0.001194 [0.001083, 0.001309]	0.00121654

These estimates reuse the original independent disorder samples and 1,000 whole-sample bootstrap draws. They add a check of an analytic coefficient, rather than independent evidence about a crossover.

Corollary 7.4 (Joint small-time and quadratic limit)**.** *For fixed even $N \geq 14$ and θ in a compact real interval,*

$$\lim_{\kappa\to\infty} \kappa^8 C_z^\circ(\theta/\kappa) = \frac{b_N}{4}\theta^6 + \frac{v_{4,N}}{576}\theta^8, \tag{7.12}$$

uniformly in θ, where b_N is defined in Theorem 5.1.

Proof. With $Y = \mathrm{tr}_D[A^\circ(B^\circ)^2]$, the cubic formula gives $m_3(H_\kappa^\circ) = 3Y/\kappa + O_{L^\infty}(\kappa^{-3})$. Also $m_4(H_\kappa^\circ) = m_4(B^\circ) + O_{L^\infty}(\kappa^{-1})$. The bounded matrix Taylor expansion therefore implies

$$\kappa^4\{z_\kappa(\theta/\kappa) - \mathbb{E}z_\kappa(\theta/\kappa)\} \longrightarrow \frac{i\theta^3}{2}Y + \frac{\theta^4}{24}\{m_4(B^\circ) - \mathbb{E}m_4(B^\circ)\}$$

in L^2, uniformly on compact θ intervals. The two terms are respectively imaginary and real, so their modulus-squared cross term is zero samplewise. Taking second moments proves (7.12). □

The endpoint has an order-t^8 covariance, whereas each finite large κ retains an order-t^6 term suppressed by κ^{-2}. Equation (7.12) specifies how these terms coexist on $t = \theta/\kappa$; it is a finite-N asymptotic statement, not a criterion for a thermodynamic transition.

7.4 Independent projection onto smooth moments

Exact conditioning on continuously distributed moments requires their conditional spectral law. A finite regression addresses a different, well-defined question: which fluctuations can be predicted by a chosen set of smooth moment features? The relation between the two questions has a useful exact bound.

Proposition 7.5 (Prediction error relative to exact conditioning)**.** *Let M be a vector of spectral moments, let $\mathcal{T}$ be training data independent of a fresh disorder sample, and let $\widehat{h}_{\mathcal{T}}(M)$ be the trained predictor. Then*

$$\begin{aligned}\mathrm{Var}_{\mathbb{C}}(Z - \widehat{h}_{\mathcal{T}}(M) \mid \mathcal{T}) = \mathbb{E}\,\mathrm{Var}_{\mathbb{C}}(Z \mid M) \\ + \mathrm{Var}_{\mathbb{C}}(\mathbb{E}[Z \mid M] - \widehat{h}_{\mathcal{T}}(M) \mid \mathcal{T}).\end{aligned} \tag{7.13}$$

Thus the population variance of the fitted residual is an upper bound on the exact conditional residual variance, for each fixed training set. There is no corresponding fourth-cumulant ordering.

Proof. Write the residual as $Z - \mathbb{E}[Z \mid M] + \mathbb{E}[Z \mid M] - \widehat{h}_{\mathcal{T}}(M)$. The two terms are orthogonal conditionally on $\mathcal{T}$ because the first has zero conditional mean given $M, \mathcal{T}$. Independence makes its variance $\mathbb{E}\,\mathrm{Var}_{\mathbb{C}}(Z \mid M)$. □

We evaluate $Z_f(t) = \mathrm{Tr}_D[f(H_\kappa^\circ)e^{-itH_\kappa^\circ}]$ with the original physical Gaussian filter $\sigma_f = 0.5$, at $t = 0, 4, 16, 64$ and $\kappa = 0, 4, 16, 64, \infty$. The independent fixed-radius samples number 4096 at $N = 14$ and 1024 at $N = 18$. A declared random split assigns 1365 and 341 samples, respectively, to training; the remaining 2731 and 683 form the held-out sets. The same split is used for all couplings, times, and models, retaining the pairing of the original disorder directions across κ.

The three predetermined feature spaces contain: (i) m_3, m_4; (ii) m_3, m_4, m_5, m_6; and (iii) these four moments and all their pairwise products. We fit ordinary least squares after training-only standardization, respecting $H \mapsto -H$: even features and an intercept predict the real trace, and odd features predict the imaginary trace. Odd moments are centered at their exact zero ensemble mean. An identically vanishing moment is inactive. No fit or choice of feature space uses the held-out response. The analysis program records the split indices, training-set standardization, coefficients, ranks and held-out residuals when run on the sample spectra.

For each fixed fitted predictor, the held-out residuals are independent draws of $Z - \widehat{h}_{\mathcal{T}}(M)$. We use the unbiased second- and fourth-cumulant estimators of Theorem B.2, retaining the complex pseudocovariance. The 1,000 bootstrap resamples each resample an entire held-out direction pair across every coupling, time, and model. The reported 95% intervals are pointwise percentile intervals conditional on the fixed training fit. Ratios of estimated cumulants are not unbiased. Five further declared splits provide a separate descriptive sensitivity check; they are not pooled as independent observations.

To separate variance removal from a change of scale, report all three quantities

$$\eta = \frac{C_{\mathrm{res}}}{C_Z}, \qquad \xi = \frac{Q_{\mathrm{res}}}{C_Z^2}, \qquad q_{\mathrm{res}} = \frac{Q_{\mathrm{res}}}{C_{\mathrm{res}}^2}, \qquad \xi = \eta^2 q_{\mathrm{res}}. \tag{7.14}$$

Here C_Z is estimated on the same held-out samples before projection. These are cumulants of the fitted residual. They do not estimate $\mathbb{E}Q_{\mathcal{F}_6}$ or the cumulant of the exact $\mathcal{F}_6$-centered trace.

7.5 What the held-out spectra resolve

Table 2 and Figure 4 show a substantial contribution of the chosen smooth moments to the nonoscillatory filtered trace. At $t = 0$, quadratic features in $m_3, \ldots, m_6$ remove approximately 84% and 89% of its variance at $\kappa = 4$ for $N = 14, 18$. At the quadratic endpoint the removed fractions are 88% and 98%. This is a large effect on the trace of the smooth filter $f(H)$ even though the coupling radii were already fixed.

The distinction between the last two normalizations matters. At $N = 18$, $\kappa = \infty$, and $t = 0$, the residual fourth cumulant on the original variance scale is only $\xi = 0.00310$, but $q_{\mathrm{res}} = 6.87$ because the residual variance is much smaller. Before projection the same held-out sample has $Q_Z/C_Z^2 = 1.63$. An increased variance-normalized fourth cumulant therefore need not mean that an absolute fourth-order fluctuation became larger.

The same feature spaces explain little of the later-time variance. At $\kappa = 4$, the quadratic fit leaves positive fourth cumulants at $t = 4$ and $t = 16$. For the latter time, ξ equals 0.225 $[0.089, 0.380]$ at $N = 14$ and 1.234 $[0.576, 1.939]$ at $N = 18$. The sign is time dependent: at $N = 18$, $\kappa = 4$, and $t = 64$, $\xi = -0.143$ $[-0.263, -0.020]$, while the corresponding $N = 14$ interval includes zero. At the quadratic endpoint, positive fourth excess remains through $t = 64$ after the same projection. Across the five additional splits, the endpoint $t = 64$ estimates of ξ range from 2.83 to 3.51 at $N = 14$ and from 7.40 to 8.00 at $N = 18$; at $t = 16$ the $N = 18$ range

N	κ	t	η [95% interval]	ξ [95% interval]	q_{res} [95% interval]
14	4	0	0.163 [0.148, 0.179]	0.018 [0.006, 0.035]	0.686 [0.250, 1.239]
14	4	4	0.919 [0.902, 0.936]	0.725 [0.474, 1.011]	0.858 [0.557, 1.196]
14	∞	0	0.121 [0.108, 0.137]	0.127 [0.045, 0.256]	8.665 [3.682, 16.198]
14	∞	64	1.000 [0.998, 1.002]	3.493 [2.925, 4.120]	3.495 [2.929, 4.123]
18	4	0	0.110 [0.092, 0.129]	0.0001 [−0.0036, 0.0040]	0.011 [−0.296, 0.335]
18	4	4	0.954 [0.921, 0.994]	1.309 [0.508, 2.141]	1.437 [0.554, 2.327]
18	∞	0	0.021 [0.017, 0.026]	0.0031 [0.0010, 0.0067]	6.868 [3.135, 10.777]
18	∞	64	1.037 [1.005, 1.076]	6.930 [5.451, 8.297]	6.443 [5.112, 7.751]

Table 2: Held-out cumulants after the quadratic projection in $m_3, \ldots, m_6$, with the three normalizations in (7.14). Every confidence interval conditions on the independently trained predictor. The statistical target is the cumulant of this fitted residual.

is wider, from 4.03 to 9.24. This sensitivity and the different training sample counts preclude assigning an asymptotic size exponent to these fourth-order data.

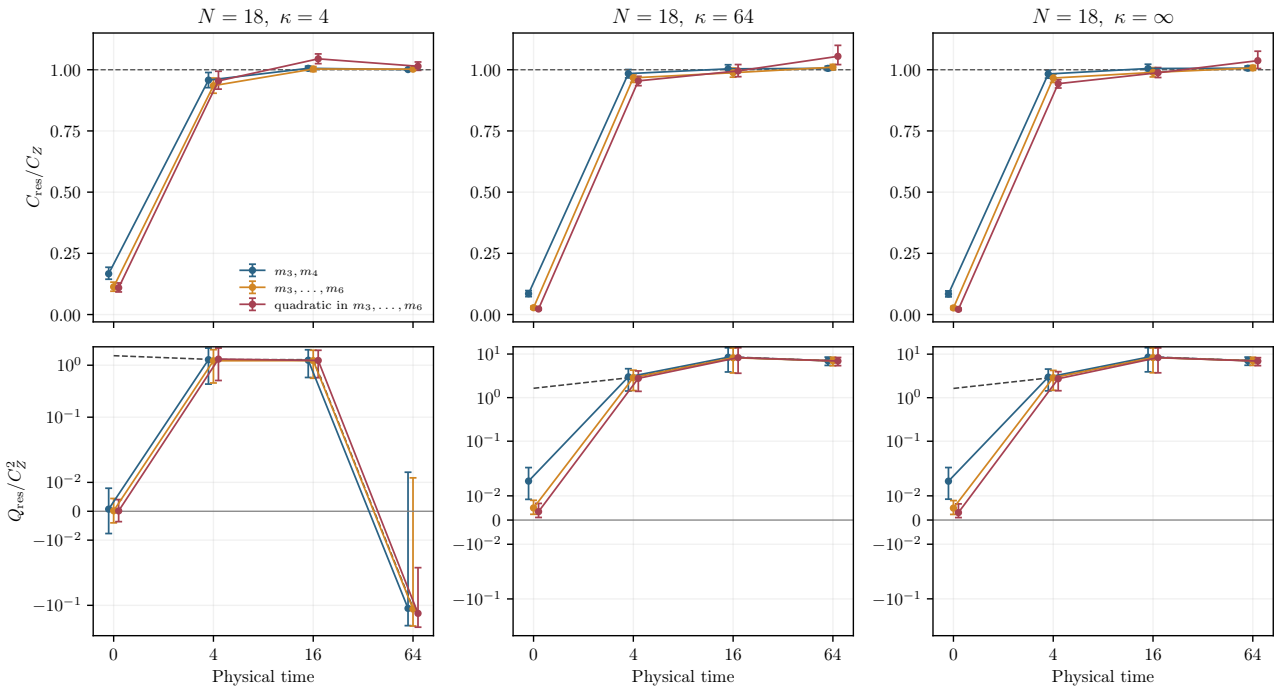


Figure 4: Independent smooth-moment projection at $N = 18$. The top row shows the retained variance η; the bottom row shows the residual fourth cumulant ξ on the original variance scale. The three curves use the predetermined linear and quadratic feature spaces described in Section 7.4. Dashed curves show unity above and the unprojected Q_Z/C_Z^2 below. Error bars are pointwise 95% held-out bootstrap intervals conditional on the fitted predictor. Sampled times have equally spaced plotting positions; connecting lines only guide the eye. The lower vertical axes use a symmetric logarithmic scale. The supplement tabulates both sizes.

Some held-out variance fractions exceed one, including the $N = 18$ endpoint at $t = 64$. We retain these values: a finite fitted predictor can increase variance on independent data, and the discrepancy is not an exact orthogonal-projection gain. The supported conclusion is that these

declared low-degree smooth-moment predictors account for much of the $t = 0$ fluctuation but do not account for the observed later-time fourth excess. This does not exclude prediction by more general functions of the same moments. Equation (7.13) provides an upper bound on the exact conditional residual variance; neither that bound nor the regression supplies a lower bound on the exact conditional fourth cumulant. Such a cumulant requires sampling or reconstructing the conditional law, as distinct from fitting its mean in a finite feature space.

8 Radial susceptibility and refined crossover curves

The radial convolution permits differentiation even when no differentiability of the angular observable is assumed. This supplies an exact susceptibility formula and a relation between crossover steepness and radial fluctuations. We use the same representation to evaluate radial averages directly, thereby removing the angular interpolation from that calculation. The differentiation principle is the standard likelihood-ratio or score-function method [Gly90]; the explicit chi-ratio kernels, their Fisher coefficient, and their use in this spectral decomposition are the specialization developed here.

8.1 Exact susceptibility and a variance bound

Let ω denote the two coupling directions, and write $r_\omega(x) = O(H^\circ_{e^x}(\omega))$ for a bounded measurable, real-valued, scale-invariant observable. Its Gaussian-ensemble mean is

$$G(x) = \mathbb{E}_{\omega,\eta} r_\omega(x + \eta), \qquad \eta = \log R_2 - \log R_4.$$

Set $a = d_2/2$, $b = d_4/2$, and $c = d_2/d_4$. The density of η and a convenient transformed variable are

$$p_\eta(z) = \frac{2c^a e^{2az}}{B(a,b)(1 + ce^{2z})^{a+b}}, \qquad w(z) = \frac{ce^{2z}}{1 + ce^{2z}}. \tag{8.1}$$

Under this density $w(\eta)$ has the Beta(a, b) distribution. Define the density score and its second derivative kernel by

$$\begin{aligned} S_\eta(z) &= 2\{a - (a+b)w(z)\}, \\ T_\eta(z) &= S_\eta(z)^2 - 4(a+b)w(z)\{1 - w(z)\}. \end{aligned} \tag{8.2}$$

Theorem 8.1 (Radial susceptibility and fluctuation bound)**.** *For every bounded measurable angular response, G is smooth and*

$$\begin{aligned} G'(x) &= -\mathbb{E}\big[r_\omega(x + \eta) S_\eta(\eta)\big], \\ G''(x) &= \mathbb{E}\big[r_\omega(x + \eta) T_\eta(\eta)\big]. \end{aligned} \tag{8.3}$$

Both score kernels have zero expectation. Consequently any bounded $c_\omega(x)$ independent of η, conditional on ω, may be subtracted from $r_\omega(x+\eta)$ in either identity. The score Fisher information is

$$\mathcal{I}_\eta = \mathbb{E} S_\eta(\eta)^2 = \frac{4ab}{a + b + 1} = \frac{2d_2 d_4}{d_2 + d_4 + 2}. \tag{8.4}$$

In particular,

$$|G'(x)|^2 \le \mathcal{I}_\eta \, \mathbb{E}_\omega \operatorname{Var}_\eta[r_\omega(x + \eta)]. \tag{8.5}$$

The coefficient is sharp over all bounded measurable response functions r_ω. Moreover, G extends holomorphically to the strip $|\operatorname{Im} x| < \pi/2$.

Proof. The $F(d_2, d_4)$ density of $e^{2\eta}$ gives (8.1). Its logarithmic derivative is S_η, and $p''_\eta/p_\eta = T_\eta$. All derivatives of p_η are integrable: each is p_η times a polynomial in the bounded variable w. Write $G(x) = \int F(y)p_\eta(y-x)\,dy$, where $F(y) = \mathbb{E}_\omega r_\omega(y)$. Differentiation of this convolution gives (8.3), with the stated signs. The integrals of p'_η and p''_η vanish, proving the centering assertion. The mean and variance of the beta variable give $\mathbb{E}S_\eta = 0$ and (8.4).

Choose $c_\omega(x) = \mathbb{E}_\eta r_\omega(x+\eta)$ and apply Cauchy–Schwarz over (ω, η). This proves (8.5). At a fixed x_0, a response of the form $r_\omega(y) = c_0 + c_1 S_\eta(y - x_0)$, independent of ω, attains equality. Since the score is bounded, nonzero c_1 can be chosen small enough to put this response in any prescribed nontrivial bounded interval.

For the last assertion, use the principal branch of $(1 + ce^{2z})^{-(a+b)}$ in $|\operatorname{Im} z| < \pi/2$. Its denominator never vanishes there, and for $r \geq 0$,

$$|1 + re^{-2iv}| \geq \cos(v)(1+r), \qquad |v| < \pi/2.$$

Thus on every closed smaller strip, $|p_\eta(y-z)|$ is bounded by a constant times $p_\eta(y - \operatorname{Re} z)$. The convolution with bounded F converges locally uniformly and is holomorphic. □

The right-hand side of (8.5) is the variance generated by changing the radii at fixed coupling directions. Thus a steep Gaussian response requires a minimum amount of radial within-direction variance. Since $\mathcal{I}_\eta \sim N^2$, the lower bound scales as $N^{-2}|G'|^2$. If $r_\omega \in [L, U]$, the same theorem gives

$$|G'(x)| \leq \frac{U-L}{2}\sqrt{\mathcal{I}_\eta}.$$

For example, if a Gaussian spacing response has endpoint span $\Delta r > 0$ and logarithmic interquartile width W_{G}, the mean-value theorem yields a point ξ between its two crossings such that

$$\mathbb{E}_\omega \operatorname{Var}_\eta[r_\omega(\xi+\eta)] \geq \frac{(\Delta r)^2}{4\mathcal{I}_\eta W_{\mathrm{G}}^2}. \tag{8.6}$$

These identities concern the Gaussian mean and its radial susceptibility; they do not require smoothness of an individual spacing-ratio curve. The holomorphic strip does not provide a bound uniform in N: the proof contains the factor $\cos(v)^{-(d_2+d_4)/2}$ on the line $\operatorname{Im} x = v$. Finite-size radial analyticity therefore does not exclude a singular limit as N tends to infinity.

8.2 Response normalization and size comparison

The spacing observable is the adjacent-gap ratio averaged over the central 50% of levels by rank, with every level triple entirely inside the window. We use even-parity dimensions $D = 16, 64, 256, 1024$ for $N = 10, 14, 18, 22$, respectively; all four quartic blocks have the same unitary symmetry class. The independent angular sample counts are $2048, 2048, 512, 128$. Each sample retains the same two directions across all couplings. With measured finite-size endpoints define

$$p_N(\kappa) = \frac{\bar{r}^\circ_N(0) - \bar{r}^\circ_N(\kappa)}{\bar{r}^\circ_N(0) - \bar{r}^\circ_N(\infty)}, \qquad W_N = \log\frac{\kappa_{0.75,N}}{\kappa_{0.25,N}}.$$

We clip the estimated response to $[0,1]$, apply equal-weight isotonic regression to the interior grid with fixed endpoints, and locate the three response crossings by linear interpolation in $\log\kappa$. This defines an operational curve; the unprojected means are also retained. Endpoints and the normalizing denominator are re-estimated in every bootstrap draw. The quadratic endpoint is measured rather than replaced by a Poisson reference. Appendix H records the original grid, raw-threshold sensitivity, and derivative bounds for comparison with the refinement below.

8.3 A direct radial estimator

We reconstruct all $4,736$ direction pairs from the independent four-size scan in Appendix H. For each direction we generate four independent uniforms U_j and use the eight exact shifts

$$\eta_j = \tfrac{1}{2}\log F^{-1}_{d_2,d_4}(U_j), \qquad \eta_{j+4} = \tfrac{1}{2}\log F^{-1}_{d_2,d_4}(1-U_j), \qquad j = 1,\dots,4.$$

Every shifted Hamiltonian is diagonalized. These radii are independent of the radii in the original Gaussian sample. The radial average is therefore estimated without interpolating an angular curve. Pairing each uniform with its complement preserves the exact marginal law; only the four pairs are independent conditional on the direction.

Let h^+_{bj} and h^-_{bj} be the two shifted spacing ratios in pair j of angular sample b, let $J = 4$, and put $g_{bj} = (h^+_{bj} + h^-_{bj})/2$. The per-direction radial average and variance estimators are

$$\begin{aligned} \widehat{m}_b &= \frac{1}{J}\sum_j g_{bj}, \\ \widehat{v}_b &= \frac{1}{2J}\sum_j \{(h^+_{bj})^2 + (h^-_{bj})^2\} - \frac{(\sum_j g_{bj})^2 - \sum_j g_{bj}^2}{J(J-1)}. \end{aligned} \tag{8.7}$$

Conditional on the direction, their expectations are the exact radial mean and variance. The variance formula uses distinct independent pairs for the product of means; it accommodates the antithetic dependence inside each pair. Score derivatives are estimated from (8.3), subtracting the unshifted ratio as the radius-independent control. We also compare $\widehat{m}_b$ with the original Gaussian ratio at the same direction; this uses independent radial samples on the two sides.

We evaluate $\kappa = 8, 12, 16$ at $N = 10, 14$, $\kappa = 16, 24, 32$ at $N = 18$, and $\kappa = 32$ at $N = 22$. The $1,000$ whole-direction bootstrap resamples retain the original coupling pairings and all fresh antithetic pairs. Intervals are pointwise. The susceptibility-efficiency statistic

$$\frac{\widehat{G}'(x)^2}{\mathcal{I}_\eta\,\widehat{\mathbb{E}_\omega v_\omega(x)}}$$

is reported with its propagated interval; its finite-sample ratio and squared numerator are not unbiased estimators.

8.4 Refining the directional crossing grid

For every size we add three equally spaced points in $\log\kappa$ inside each of the three coarse intervals containing the previously measured quarter, half, and three-quarter crossings. This adds nine couplings per size while retaining all original angular draws and endpoint spectra. The refined intervals are $(4,8),(8,12),(12,16)$ at $N = 10$; $(4,8),(8,12),(16,24)$ at $N = 14$; $(8,12),(16,24),(32,48)$ at $N = 18$; and $(16,24),(24,32),(64,96)$ at $N = 22$. The computation retains the fine-grid spectra and generates each radial shift from its sample index and seed.

The selected refinement intervals are held fixed in inference. The same endpoint normalization, isotonic projection, and log-linear crossing definition are applied to the combined grid. Reusing the angular draws allows a paired comparison between the coarse and refined estimates. We separately report shape-preserving cubic interpolation on the refined grid. These interpolation comparisons do not enter the sampling interval as an additional probabilistic error. The bootstrap does not repeat the data-driven grid selection and should not be interpreted as a post-selection coverage guarantee for the complete adaptive procedure.

N	Directions	$\kappa_{0.5}$ [95% interval]	W_N [95% interval]	σ_η/W_N
10	2048	8.461 [8.045, 8.901]	0.9052 [0.8629, 0.9541]	0.1296
14	2048	11.849 [11.553, 12.147]	1.1255 [1.0947, 1.1558]	0.0691
18	512	20.450 [19.582, 21.349]	1.3332 [1.2755, 1.3894]	0.0441
22	128	29.286 [27.712, 31.053]	1.3386 [1.2129, 1.4536]	0.0354

Table 3: Refined fixed-radius crossover estimates. The intervals are percentile intervals from 1,000 whole-direction resamples, with the selected coupling grid and crossing rule held fixed. The last column compares the exact radial log-coupling standard deviation with the measured directional width.

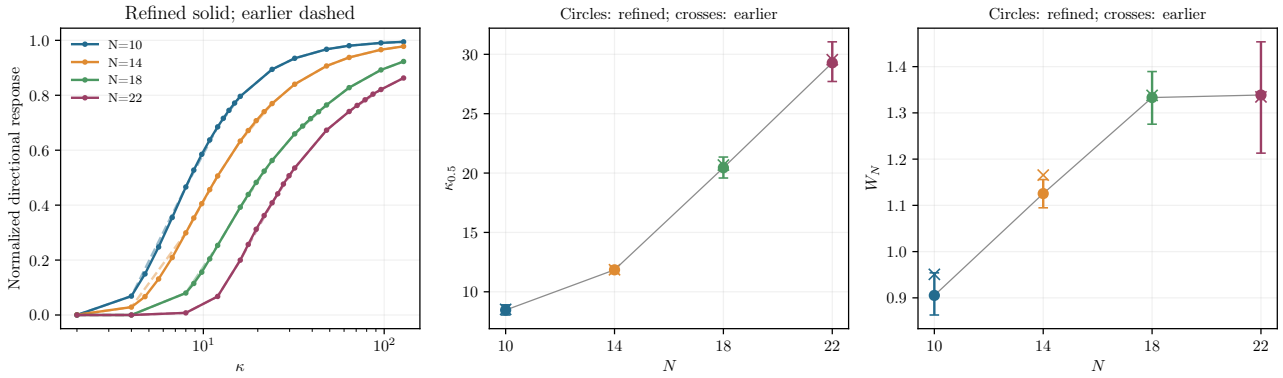


Figure 5: Directional crossover after local grid refinement. Left: the isotonic response on the combined grid, with the earlier coarse-grid interpolation dashed. Middle and right: refined half-response couplings and logarithmic widths, with pointwise 95% bootstrap intervals; crosses mark the earlier estimates. All comparisons reuse the same angular realizations.

8.5 Results and finite-size interpretation

Table 3 and Figure 5 give the refined directional estimates. Relative to the coarse grid, the logarithmic widths decrease by 0.04556 at $N = 10$ and 0.04004 at $N = 14$; the paired 95% intervals are $[-0.06412, -0.02699]$ and $[-0.05286, -0.02834]$. The changes at $N = 18, 22$ are much smaller, -0.00471 and $+0.00407$. On the refined grid, replacing log-linear interpolation by PCHIP changes the widths by $-0.00064, -0.00320, -0.00058, -0.00084$, respectively. These differences measure sensitivity to the interpolation rule on the chosen grid. The continuum-grid error is unknown.

The refined successive width differences are 0.2202 $[0.1643, 0.2718]$, 0.2077 $[0.1449, 0.2721]$, and 0.0055 $[-0.1282, 0.1312]$. Thus the widening from $N = 10$ to 18 survives refinement, while the change from 18 to 22 is unresolved. The half-response coupling moves to the right at every size. Neither these four sizes nor the last unresolved width difference select a thermodynamic scaling law. The declining σ_η/W_N ratio supports the more limited conclusion that the measured broad crossover persists after both radial degrees of freedom are removed.

The direct radial calculation resolves a different numerical issue. At all ten evaluated size–coupling pairs, the fresh radial correction $G(\log \kappa) - F(\log \kappa)$ is positive and its pointwise 95% interval excludes zero. These are pointwise statements, without a simultaneous multiple-comparison coverage claim. At eight of those pairs, the paired interval for the earlier piecewise-linear convolution minus the direct radial mean excludes zero. The most transparent example

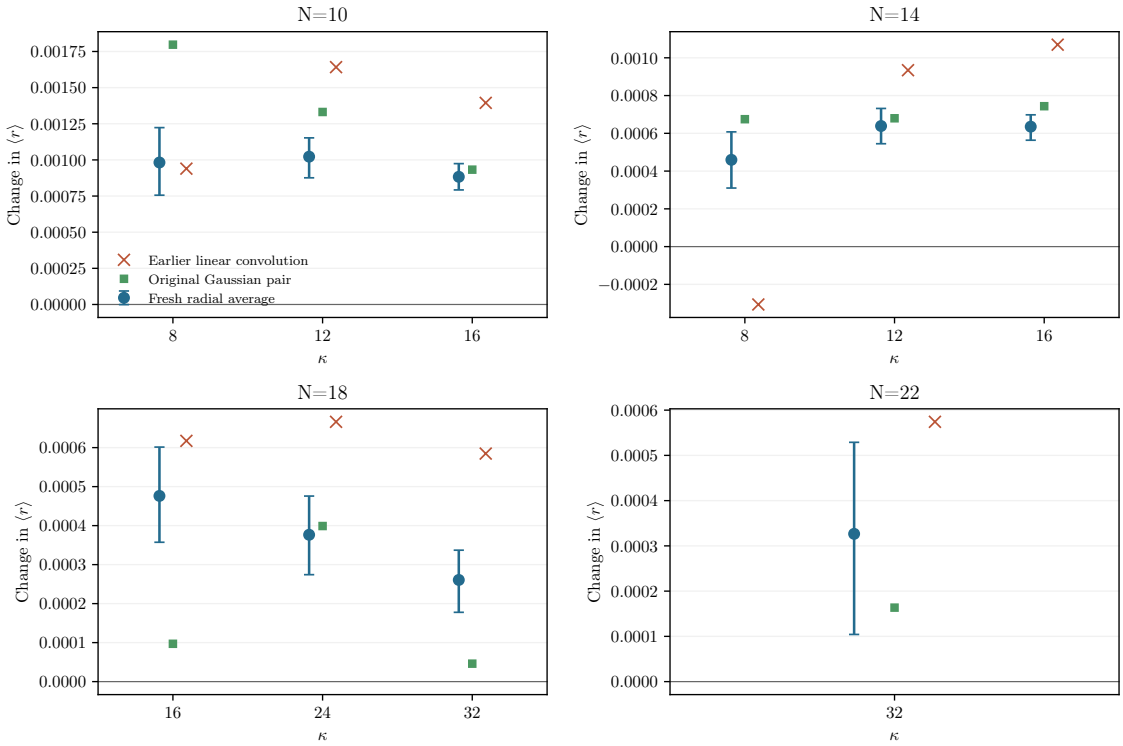


Figure 6: Radial changes in the mean spacing ratio at fixed bare coupling. Blue circles use fresh independent antithetic radius batches and direct diagonalization, with whole-direction pointwise 95% intervals. Red crosses use the earlier piecewise-linear convolution. Green squares are the original paired Gaussian-minus-directional estimates; their uncertainty is included in the paired-contrast data supplied with the paper. Points at the same coupling are displaced horizontally for readability.

is $N = 14$, $\kappa = 8$: the earlier interpolated correction was -3.0647×10^{-4}, whereas the direct estimate is 4.5965×10^{-4} with interval $[3.1023, 6.0769] \times 10^{-4}$. The interpolation changes even the sign. At $N = 22$, $\kappa = 32$, the direct correction is 3.2658×10^{-4} $[1.0425, 5.2888] \times 10^{-4}$, compared with the earlier interpolated value 5.7420×10^{-4}.

Every paired interval comparing the original Gaussian mean with the fresh directly shifted mean includes zero. This is a consistency check using independent radial samples; the two estimators share their angular realizations. It supports the implementation of the exact radial transform and identifies coupling interpolation as the relevant earlier numerical error. It is not an additional statistical argument for the identity itself, which already holds exactly.

Finally, the exact score estimator connects the mean response to its within-direction radial variance without numerical differentiation. Table 4 reports representative couplings near the crossover. The quantity $\mathcal{E} = G'^2/(\mathcal{I}_\eta V_{\mathrm{rad}})$, where $V_{\mathrm{rad}} = \mathbb{E}_\omega \operatorname{Var}_\eta r_\omega$, is bounded by one in the population. Its estimates range from 0.266 to 0.614 at the four reported points. Thus the rigorous susceptibility bound accounts for a substantial fraction of the measured radial variance, while leaving room for fluctuations not fixed by the slope of the mean. The four entries correspond to different normalized response levels.

All new spectra have unit second moment to within 4.0×10^{-15}. The stored radii reconstruct exactly, the checked base spacing ratios agree exactly with the earlier scan, and all bootstrap crossings are finite. Independent scalar quadrature verifies the score signs and Fisher coefficient,

N	κ	$-G'$ [95% interval]	$10^4 V_{\mathrm{rad}}$ [95% interval]	$\mathcal{E}$ [95% interval]
10	8	0.0920 [0.0838, 0.1005]	4.331 [4.009, 4.677]	0.266 [0.229, 0.303]
14	12	0.1009 [0.0956, 0.1065]	1.166 [1.089, 1.243]	0.525 [0.493, 0.558]
18	24	0.0757 [0.0673, 0.0835]	0.357 [0.314, 0.403]	0.551 [0.489, 0.611]
22	32	0.0834 [0.0661, 0.1026]	0.253 [0.195, 0.317]	0.614 [0.482, 0.759]

Table 4: Interpolation-free susceptibility and within-direction radial variance. Derivatives are with respect to $\log \kappa$. The variance estimator uses independent antithetic pairs, and the bootstrap resamples complete angular samples. The efficiency is a finite-sample ratio of estimators, with both numerator and denominator recomputed inside each resample.

with relative Fisher errors below 3×10^{-12} and derivative-identity errors below 3×10^{-14} for a smooth bounded test response. The supplement tabulates the pointwise estimates and paired contrasts.

9 Quadratic charges and their initial time scale

We study dynamics in the same fixed-radius ensemble used for the directional spectral observables. An oriented real normal form of the quadratic coupling defines $m = N/2$ commuting charges $Q_a = 2n_a - 1 = 2i\widetilde{\chi}_{2a-1}\widetilde{\chi}_{2a}$, with $Q_a^2 = I$ and $B^\circ = \sum_a \lambda_a Q_a$. The signed coefficients satisfy $\sum_a \lambda_a^2 = 1$; retaining their signs preserves the chosen parity block. Conditional on this quadratic normal frame, the independent quartic coefficient vector remains uniform on its unit sphere.

For each charge define $C_a(t) = \mathrm{tr}_D(e^{itH_\kappa^\circ} Q_a e^{-itH_\kappa^\circ} Q_a)$. Counting quartic monomials that meet the selected mode pair in exactly one index gives

$$\mathbb{E}_u \|[H_\kappa^\circ, Q_a]\|_{\mathrm{HS}}^2 = \frac{32(N-4)}{N(N-1)(1+\kappa^2)} = \tau_{N,\kappa}^{-2}. \tag{9.1}$$

Since $1 - \cos x \le x^2/2$, the spectral expansion of C_a implies

$$C_a(t) \ge 1 - \frac{t^2}{2}\|[H_\kappa^\circ, Q_a]\|_{\mathrm{HS}}^2, \qquad \mathbb{E}_u C_a(t) \ge 1 - \frac{t^2}{2\tau_{N,\kappa}^2}.$$

Consequently the first loss of a fraction ε of the angular-averaged memory is bounded below by $\sqrt{2\varepsilon}\,\tau_{N,\kappa}$. These statements hold for even $N \ge 10$ in either parity block. Appendix C proves the exact samplewise commutator identity and the associated state and operator Lanczos coefficients. The following sections determine the conserved component, the inelastic frequency moments, and an explicit near-resonant mechanism that separates this curvature scale from relaxation.

10 Quadratic charge memory and its conserved components

The component of a charge along the Hamiltonian contributes a time-independent term to its autocorrelation. Further conserved components may be present. Complete dephasing gives their total weight and determines the normalization of the remaining inelastic memory.

10.1 Exact separation of conserved components

Let $m = N/2$, work in one parity block of dimension D, and use the normalized trace tr_D. In the quadratic normal-mode basis, write the fixed-radius Hamiltonian as

$$H = H_\kappa^\circ = \frac{A^\circ + \kappa B^\circ}{\sqrt{1+\kappa^2}}, \qquad B^\circ = \sum_{a=1}^{m} \lambda_a Q_a, \qquad Q_a = 2n_a - 1, \qquad \sum_a \lambda_a^2 = 1. \tag{10.1}$$

The signs of the λ_a are retained when an oriented normal form is used. For $N > 8$, the Clifford trace relations give $\mathrm{tr}_D H = 0$, $\|H\|_{\mathrm{HS}} = 1$, $(Q_a|Q_b) = \delta_{ab}$, and $(A^\circ|Q_a) = 0$. For one realization set

$$\overline{C}(t) = \frac{1}{m}\sum_{a=1}^{m} \mathrm{tr}_D(Q_a(t)Q_a), \qquad g^2 = \frac{1}{m}\sum_a \|[H, Q_a]\|_{\mathrm{HS}}^2. \tag{10.2}$$

Let P_e be the spectral projections of H and define

$$\mathcal{D}_H(X) = \sum_e P_e X P_e, \qquad p_\infty = \frac{1}{m}\sum_a \|\mathcal{D}_H(Q_a)\|_{\mathrm{HS}}^2. \tag{10.3}$$

The sum over e runs over distinct energies, so dephasing retains every matrix element within a degenerate eigenspace.

Proposition 10.1 (Conserved components and charge memory)**.** *For every realization in* (10.1)*,*

$$p_\infty \geq p_E := \frac{1}{m}\sum_a |(H|Q_a)|^2 = \frac{\kappa^2}{m(1+\kappa^2)}. \tag{10.4}$$

The time average of $\overline{C}$ is p_∞. More precisely, there is a symmetric probability measure μ_Q such that

$$\overline{C}(t) = \int_{\mathbb{R}} \cos(\omega t)\, \mu_Q(d\omega), \qquad \mu_Q(\{0\}) = p_\infty, \qquad \int \omega^2\, \mu_Q(d\omega) = g^2. \tag{10.5}$$

For $p \in \{p_E, p_\infty\}$ with $p < 1$, the normalized residual

$$C_p(t) = \frac{\overline{C}(t) - p}{1-p} \tag{10.6}$$

is the cosine transform of the probability measure $(\mu_Q - p\delta_0)/(1-p)$ and obeys

$$1 - C_p(t) \leq \frac{g^2 t^2}{2(1-p)}. \tag{10.7}$$

In particular, $\overline{C}(t) \geq 2p_\infty - 1$ at every time.

If the spectrum in the block is simple, let $P_{b\alpha} = |\langle b|E_\alpha\rangle|^2$ in the quadratic occupation basis. Then

$$\begin{aligned} 1 - p_\infty &= \frac{4}{mD}\sum_{\alpha,a} \mathrm{Var}_{E_\alpha}(n_a) \\ &= \frac{2}{mD}\sum_{\alpha,b,c} P_{b\alpha}P_{c\alpha}\, d_H(b,c), \end{aligned} \tag{10.8}$$

where $d_H(b,c)$ is the Hamming distance between the two occupation strings.

Proof. The overlap with the Hamiltonian is $(H|Q_a) = \kappa\lambda_a/\sqrt{1+\kappa^2}$, so summing its square proves the last identity in (10.4). The map $\mathcal{D}_H$ is the orthogonal projection onto the commutant of H in Hilbert–Schmidt space. Its range contains H, which has unit norm, giving $\|\mathcal{D}_H(Q_a)\|_{\mathrm{HS}}^2 \geq |(H|Q_a)|^2$. The identity component vanishes because $\mathrm{tr}_D\, Q_a = 0$. This is the conserved-operator projection underlying the usual memory bounds [Maz69; Suz71].

In an orthonormal energy basis define

$$\mu_Q = \frac{1}{mD}\sum_{a,j,k} |(Q_a)_{jk}|^2 \delta_{E_j - E_k}.$$

Hermiticity makes the measure symmetric, and $Q_a^2 = I$ gives total mass one. The zero-frequency mass is exactly (10.3); the second moment is g^2. Every nonzero-frequency cosine has zero Cesàro mean. Removing the nonnegative mass $p\delta_0$ and using $1 - \cos x \leq x^2/2$ proves (10.7). The inequality $\overline{C}(t) \geq 2p_\infty - 1$ follows from $\cos x \geq -1$.

For simple spectrum, $p_\infty = (mD)^{-1}\sum_{\alpha,a} |\langle E_\alpha|Q_a|E_\alpha\rangle|^2$. Since $Q_a = 2n_a - 1$ and $n_a^2 = n_a$, $1 - \langle Q_a\rangle_\alpha^2 = 4\,\mathrm{Var}_\alpha(n_a)$. Alternatively, expand the square of $\sum_b P_{b\alpha}Q_a(b)$ and use $\sum_a Q_a(b)Q_a(c) = m - 2d_H(b,c)$. These give the two forms of (10.8). □

Equation (10.8) gives the elastic weight as the mean squared polarization of the modes in the energy eigenstates. The difference $p_\infty - p_E$ is the projection weight on conserved operators orthogonal to H. At simple spectrum, all such conserved operators are functions of H; a degenerate eigenspace can also support nonscalar conserved operators.

Let $C(t) = \mathbb{E}\,\overline{C}(t)$ and $\pi_\infty = \mathbb{E}p_\infty$. The collective energy-orthogonal and inelastic memories used in the figures are

$$\mathcal{C}_E(t) = \frac{C(t) - p_E}{1 - p_E}, \qquad \mathcal{C}_{\mathrm{inel}}(t) = \frac{C(t) - \pi_\infty}{1 - \pi_\infty}. \tag{10.9}$$

These are ratios formed after averaging over disorder. In particular, $\mathcal{C}_{\mathrm{inel}}$ is not the disorder mean of the separately normalized sample curves. The exact angular mean of the commutator gives

$$\tau_{N,\kappa} = \left[\frac{N(N-1)(1+\kappa^2)}{32(N-4)}\right]^{1/2}, \qquad \mathbb{E}g^2 = \tau_{N,\kappa}^{-2}. \tag{10.10}$$

Whenever $\pi_\infty < 1$, the inherited inelastic bound is

$$1 - \mathcal{C}_{\mathrm{inel}}(t) \leq \frac{t^2}{2\tau_{N,\kappa}^2(1-\pi_\infty)}, \qquad \tau_{\mathrm{inel}} = \tau_{N,\kappa}\sqrt{1-\pi_\infty}. \tag{10.11}$$

Subtracting and normalizing the conserved component therefore changes the initial curvature scale as well as the late-time average.

10.2 Numerical protocol and verification

We use 256, 256, 128, and 32 independent fixed-radius realizations at $N = 10, 14, 18, 22$, respectively, and evaluate $\kappa = 0, 4, 16, 64$ on the same direction pairs. All calculations use one parity block and all m parity-preserving normal-mode charges. A real Schur decomposition of the quadratic single-particle matrix is corrected to determinant $+1$; this avoids exchanging the parity blocks. Conditional orthogonal invariance permits the independent quartic direction to

be sampled directly in this normal frame. The program records the quartic directions and the ordered signed quadratic frequencies. The latter can differ across Schur implementations at the same seed. The quartic direction is sampled in that frame, so a change of ordering or sign can change the individual Hamiltonian while preserving its ensemble law.

For each Hamiltonian we compute the full spectral decomposition and the matrix elements of every Q_a. The memory is evaluated from its finite cosine measure, and p_∞ from the zero-frequency blocks. No time interval is fitted to estimate this elastic contribution. The dimensionless grid $x = t/\tau_{N,\kappa}$ runs from zero to 128, with logarithmic resolution at short and long times and a linear grid between 0.1 and 5. Because $\tau_{N,\kappa}$ is deterministic, all realizations at a given (N, κ) correspond to the same physical time. The distinct sample curvature times are retained in the data but do not set the averaging grid.

The charges satisfy $Q_a^2 = I$, zero trace, mutual commutation, and $[B^\circ, Q_a] = 0$. Their direct even-Clifford representation was also checked against the occupation-basis implementation. Across the complete data, the spectral second moments agree with the commutator norms to relative error below 1.3×10^{-13}, and the largest apparent violation of the samplewise quadratic lower bound is below 3×10^{-15}. The finite-difference curvature check agrees to relative error below 1.7×10^{-5}. No unresolved eigenvalue degeneracies were found in the sampled blocks. At $\kappa = \infty$ the result is imposed analytically: $C(t) = p_\infty = 1$ for every physical time, and the normalized inelastic memory is undefined because it has zero weight.

Uncertainty is estimated using 2000 paired bootstrap resamples of the disorder labels. All charges are averaged within each realization before resampling. For every bootstrap replicate we recompute the ratios in (10.9). We report the first resolved crossing of the ensemble curve at $C = 1-\epsilon$, for $\epsilon = 0.1, 0.5$. Crossings are linearly interpolated between adjacent saved times, and the bracketing times are retained to expose the grid resolution. Replicates without a crossing are right censored beyond $x = 128$; their censoring is retained in the bootstrap intervals.

10.3 Elastic weights and resolved losses of memory

Figure 7 and Table 5 show a substantial separation between the local curvature and the time needed for a prescribed loss of memory. At the quartic endpoint, the first resolved loss of 0.1 occurs near $x = 0.46$ at all four sizes, close to its lower bound $\sqrt{0.2}$. The larger-loss time and the intermediate-coupling curves have a stronger size dependence. At $N = 22, \kappa = 64$, a loss of 0.1 occurs at $x = 6.48$, with a paired-bootstrap 95% interval $[5.90, 7.19]$, approximately 14.5 times the curvature lower bound. A loss of 0.5 is not resolved on the sampled interval; the conserved-weight bound below gives a stronger explanation for its absence in the realized ensemble. These statements concern the ensemble curve, rather than the mean of individual realization crossing times.

The elastic contribution increases strongly with the quadratic deformation and decreases with N over the sizes studied. At $\kappa = 64$ the estimates of π_∞ are 0.9737, 0.9342, 0.8840, and 0.8131. For $N = 22$ its 95% interval is $[0.7987, 0.8256]$, while the exact linear-energy contribution is only $p_E = 0.09089$. Removing that contribution leaves an elastic weight 0.7944 in $\mathcal{C}_E$. At the same size and $\kappa = 4$, the energy-orthogonal elastic weight is 0.02424. Figure 8 displays these two levels of conserved overlap. Their size dependence is reported directly, without extrapolating a localization threshold from four sizes.

The all-time bound in Proposition 10.1 is also informative after averaging over a fixed set of realizations: $\widehat{C}(t) \geq 2\widehat{\pi}_\infty - 1$ for every t. At $N = 22, \kappa = 64$ this lower bound is 0.6261, so a raw loss of 0.5 is impossible for that finite-ensemble curve at any time, not merely absent

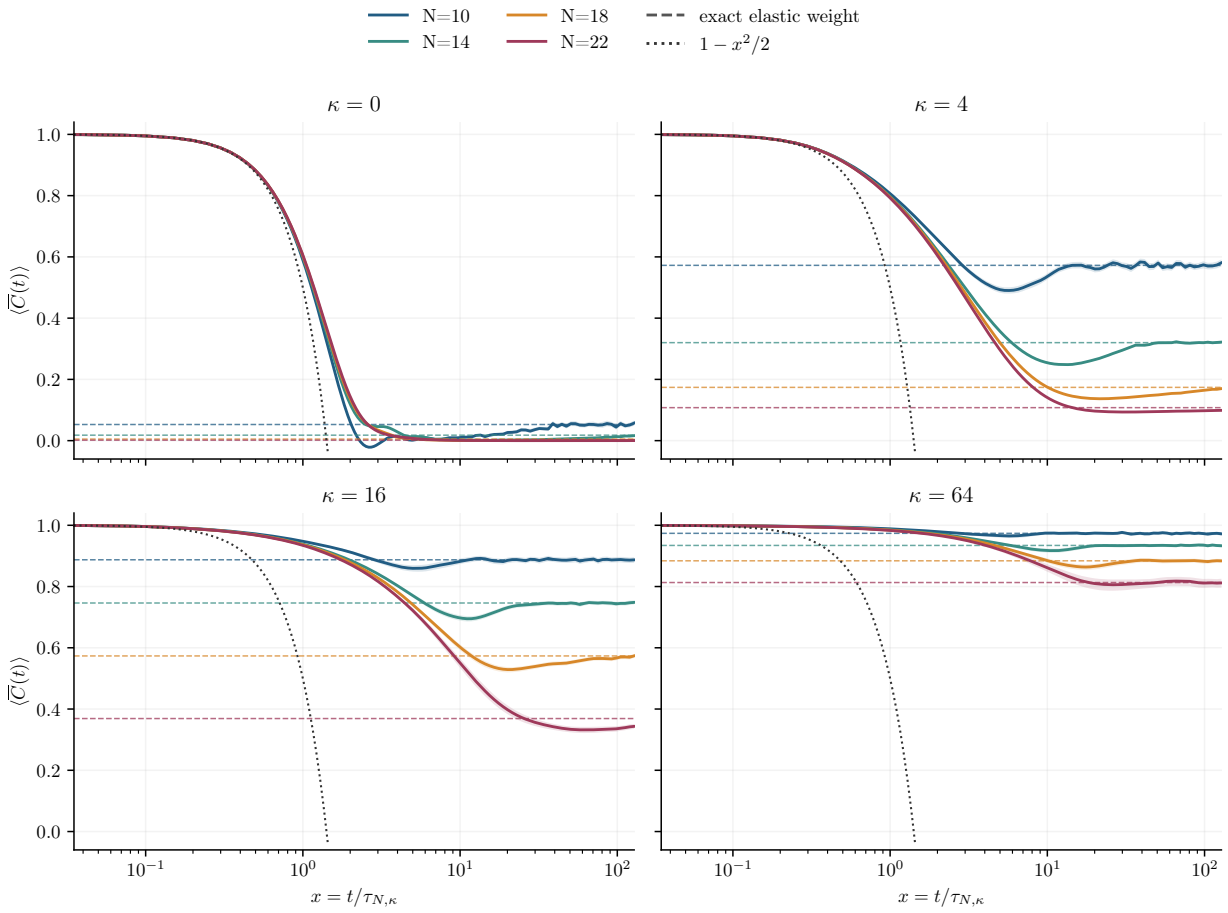


Figure 7: Ensemble-averaged quadratic charge memory in the fixed-radius ensemble. Bands are pointwise 95% bootstrap intervals. Dashed colored lines show the independently computed elastic weights; they need not equal the memory at the last plotted time. The dotted curve is the analytic ensemble lower bound $1 - x^2/2$.

from the sampled interval. All four $\kappa = 64$ finite-ensemble means have $\widehat{\pi}_\infty > 0.75$ and hence the same obstruction to a 0.5 loss. At $N = 10, \kappa = 64$, the lower bound (approximately 0.9474) also excludes a 0.1 loss. These are exact consequences of the computed finite-ensemble elastic weights, up to numerical roundoff. The corresponding population statements retain the disorder-estimation uncertainty; the crossing data preserve their operational grid-censoring flags.

Subtracting the dephased component removes the zero-frequency atom. The curves in Figure 9 retain a measurable finite-time dependence despite the high original elastic weight. At $N = 22$, $\kappa = 64$, the first half-loss on the interpolated inelastic curve occurs at $x = 5.99$ with pointwise bootstrap interval $[5.63, 6.34]$. Using the plug-in scale $\tau_{N,\kappa}\sqrt{1 - \widehat{\pi}_\infty}$ gives a half-loss time of 13.85 with bootstrap interval $[13.02, 14.74]$. The corresponding population lower bound is one in units of τ_{inel}. The zero Cesàro mean of the residual follows directly from the dephasing projection.

The observed scale separation has two identifiable contributions: the weight retained by conserved energy-diagonal components and the frequency distribution of the remaining charge matrix elements. The exact cosine representation measures both within the same spectral

N	κ	p_E	$\widehat{\pi}_\infty$ [95% CI]	$x_{0.1}$	$x_{0.5}$
10	0	0.000	0.0527 [0.0516, 0.0539]	0.46	1.14
10	4	0.188	0.5724 [0.5666, 0.5783]	0.56	4.56
10	16	0.199	0.8874 [0.8806, 0.8938]	2.38	∞^*
10	64	0.200	0.9737 [0.9694, 0.9778]	∞^*	∞^*
14	0	0.000	0.0179 [0.0177, 0.0180]	0.46	1.16
14	4	0.134	0.3200 [0.3177, 0.3222]	0.55	2.99
14	16	0.142	0.7462 [0.7402, 0.7518]	1.71	> 128
14	64	0.143	0.9342 [0.9297, 0.9387]	> 128	∞^*
18	0	0.000	0.005131 [0.005100, 0.005164]	0.46	1.17
18	4	0.105	0.1739 [0.1731, 0.1748]	0.55	2.84
18	16	0.111	0.5734 [0.5668, 0.5795]	1.62	> 128
18	64	0.111	0.8840 [0.8771, 0.8902]	7.87	∞^*
22	0	0.000	0.001501 [0.001492, 0.001509]	0.46	1.18
22	4	0.086	0.1077 [0.1073, 0.1082]	0.55	2.74
22	16	0.091	0.3689 [0.3597, 0.3773]	1.54	12.14
22	64	0.091	0.8131 [0.7987, 0.8256]	6.48	∞^*

Table 5: Exact energy-projection weight p_E, estimated full elastic weight, and first resolved losses of the ensemble-averaged charge memory. Here $x_\epsilon = t_\epsilon/\tau_{N,\kappa}$. The plateau is obtained from spectral dephasing, rather than from the final plotted time. The symbol ∞^* certifies that $2\widehat{\pi}_\infty - 1 > 1 - \epsilon$, excluding the crossing at every time for the realized finite ensemble; this is not a population certainty. The symbol > 128 records only grid censoring. Crossing brackets, operational censoring flags, and paired-bootstrap intervals are supplied in the numerical data.

decomposition. A long-lived total memory can consequently be examined together with its elastic weight and its residual dynamics, with no identification of a finite-time shoulder as an additional thermodynamic phase.

11 Frequency moments and a monotone memory diagnostic

The nonnegative symmetric frequency measure in Section 10 connects the initial commutator bound to the full autocorrelation. Its fourth moment gives a further exact constraint, while a positive time average provides a relaxation diagnostic with a unique crossing. Throughout this section, averages include all $m = N/2$ normal-mode charges. The expectation over the quartic direction is taken at fixed normalized quadratic Hamiltonian $B^\circ = \sum_a \lambda_a Q_a$, $\sum_a \lambda_a^2 = 1$.

Theorem 11.1 (Fourth Liouvillian moment)**.** *For even $N \geq 10$, put*

$$d = \binom{N}{4}, \qquad M = 2\binom{N-2}{3}, \qquad K = 4\binom{N-4}{3} + 4(N-4).$$

The second and fourth frequency moments are

$$\gamma_2(N,\kappa) := \mathbb{E}_u \frac{1}{m}\sum_a \|[H_\kappa^\circ, Q_a]\|_{\mathrm{HS}}^2 = \frac{32(N-4)}{N(N-1)(1+\kappa^2)},$$
$$\gamma_4(N,\kappa) := \mathbb{E}_u \frac{1}{m}\sum_a \|[H_\kappa^\circ, [H_\kappa^\circ, Q_a]]\|_{\mathrm{HS}}^2 = \frac{\alpha_N + \kappa^2\beta_N}{(1+\kappa^2)^2}, \tag{11.1}$$

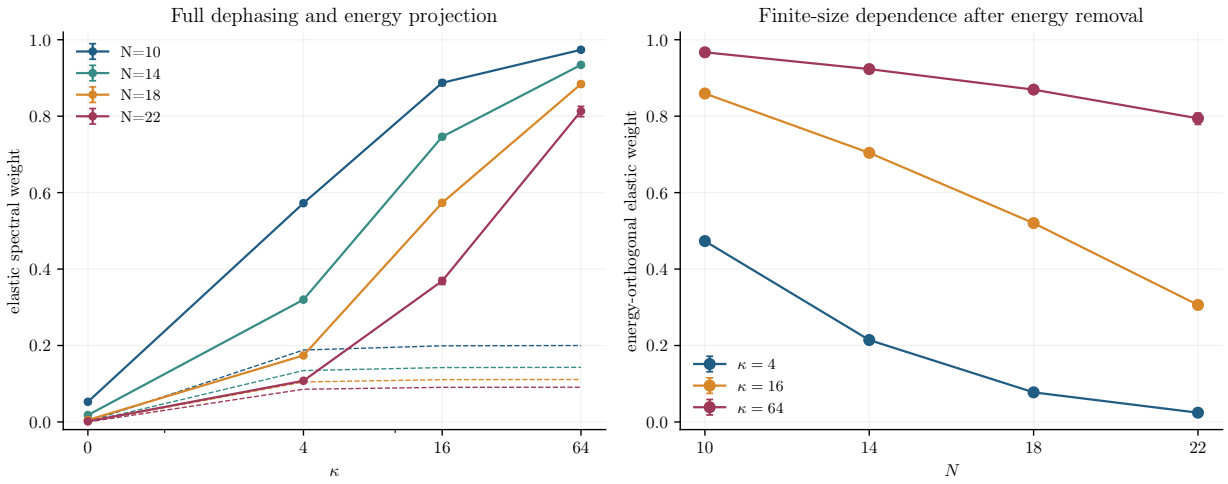


Figure 8: Left: the full elastic weight with 95% bootstrap intervals (solid lines) and the exact projection onto the Hamiltonian (dashed lines). Right: the residual elastic weight $(\pi_\infty - p_E)/(1 - p_E)$ after removing the Hamiltonian component. All weights come from spectral projections.

$$\alpha_N = \frac{16(3M^2/2 + MK)}{d(d+2)}, \qquad \beta_N = \frac{512(N-4)(2N-9)}{N^2(N-1)(N-3)}. \tag{11.2}$$

After averaging over the quartic direction and the charges, these moments are independent of the individual quadratic singular values. They hold in either parity block and in the full normalized trace.

Proof. The second-moment identity was proved in Theorem C.1. Write $L_I = [\Gamma_I, \cdot]$, $L_A = \sum_I u_I L_I$, and $L_B = [B^\circ, \cdot]$. Since $L_B Q_a = 0$,

$$[H_\kappa^\circ, [H_\kappa^\circ, Q_a]] = \frac{L_A^2 Q_a + \kappa L_B L_A Q_a}{1 + \kappa^2}.$$

The mixed scalar product has zero angular expectation by $u \mapsto -u$. The fourth spherical moment of u is the sum of three Kronecker pairings divided by $d(d+2)$.

There are M quartic monomials anticommuting with a given Q_a, and $L_I^2 Q_a = 4Q_a$ for these monomials. The pairing with operator order I, I, J, J therefore contributes $16M^2$ to $\mathbb{E}_u(Q_a | L_A^4 Q_a)$ before division by $d(d+2)$. For the order I, J, J, I, the product $\Gamma_I Q_a$ is again a quartic monomial. It anticommutes with exactly K quartic monomials: their index sets intersect its four indices in either one or three places. This contraction contributes $16MK$. For the remaining order I, J, I, J, both I and J must anticommute with Q_a and commute with each other. For every fixed I, exactly $M/2$ of the eligible J commute with it. Indeed, fix the three indices of J outside the selected mode pair; of the two possible indices inside that pair, exactly one makes $|I \cap J|$ even. This gives $16M^2/2$, proving α_N.

For I let $S(I)$ be its singly occupied mode pairs and $\nu(I) = |S(I)|$. Quadratic adjoint action preserves Clifford degree. Orthogonality and $\mathbb{E} u_I u_J = \delta_{IJ}/d$ give

$$\mathbb{E}_u \| L_B L_A Q_a \|_{\mathrm{HS}}^2 = \frac{16}{d} \sum_{I : a \in S(I)} \sum_{b \in S(I)} \lambda_b^2.$$

Average over a and use permutation symmetry of the mode pairs together with $\sum_b \lambda_b^2 = 1$. The result is $16 \sum_I \nu(I)^2/(m^2 d)$. The counts for $\nu = 4, 2, 0$ are, respectively, $16\binom{m}{4}$, $4\binom{m}{2}(m-2)$,

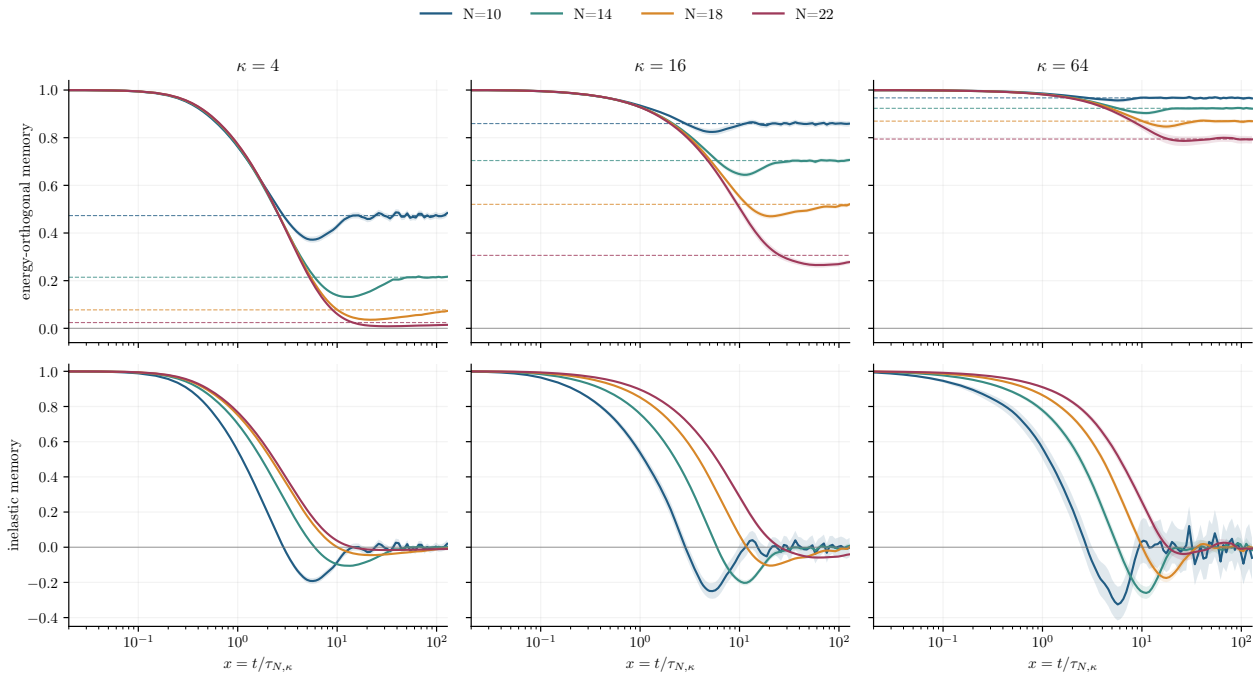


Figure 9: Two conserved-component subtractions applied to the same ensemble data. Top: the collective memory orthogonal to the Hamiltonian, with its residual elastic weight shown by dashed lines. Bottom: the collective inelastic memory after removing the full energy-diagonal projection. Both rows use the deterministic time $x = t/\tau_{N,\kappa}$; the bottom row has the distinct initial scale in (10.11). Bands are paired-bootstrap 95% intervals for the ratios of ensemble means.

and $\binom{m}{2}$. Thus

$$\sum_I \nu(I)^2 = 256\binom{m}{4} + 16\binom{m}{2}(m-2) = \frac{8}{3}m(m-1)(m-2)(4m-9),$$

which simplifies to β_N. All orthogonality steps concern quartic monomials and are valid for $N > 8$ in either parity block. In the fourth-order spherical contractions each paired Clifford label occurs twice; their products therefore have the same scalar trace in both blocks. □

We checked these coefficients using all 672 charge directions, without new disorder sampling. Direct double commutators determine the coefficients of 1, κ, and κ^2 in each realization. Independent energy-basis calculations at $N = 10, 14$ check the fourth frequency moment for one direction per size. Table 6 reports the sample averages of the two nonzero angular coefficients. Bootstrap units are complete disorder samples, with 2,000 resamples. This calculation tests a different operator moment from the initial curvature.

11.1 Positive time averaging and moment bounds

Let $\overline{\mu}_Q$ be the charge- and disorder-averaged symmetric frequency probability measure, let $\pi_\infty = \overline{\mu}_Q(\{0\}) < 1$, and define its normalized inelastic part by

$$\nu = \frac{\overline{\mu}_Q - \pi_\infty \delta_0}{1 - \pi_\infty}.$$

Table 6: Validation of the fourth Liouvillian moment. Each entry is the sample coefficient divided by its exact angular expectation; brackets give 95% bootstrap intervals over complete disorder samples.

N	Samples	$\widehat{\alpha}_N/\alpha_N$	$\widehat{\beta}_N/\beta_N$
10	256	0.9977 [0.9883,1.0076]	1.0075 [0.9904,1.0264]
14	256	1.0000 [0.9968,1.0033]	0.9933 [0.9850,1.0015]
18	128	0.9990 [0.9967,1.0010]	0.9953 [0.9900,1.0009]
22	32	1.0010 [0.9988,1.0033]	1.0040 [0.9952,1.0121]

The disorder expectation is taken before this normalization. For $T > 0$, the exponentially averaged inelastic memory is

$$\mathcal{L}(T) = \frac{1}{T}\int_0^\infty e^{-t/T}\mathcal{C}_{\mathrm{inel}}(t)\,dt = \int \frac{\nu(d\omega)}{1+T^2\omega^2}. \tag{11.3}$$

It decreases continuously and strictly from one to zero. In particular, its half-response time is always finite and unique. This average is useful when the unaveraged autocorrelation has oscillations or several crossings.

Proposition 11.2 (Two-moment memory bounds)**.** *Suppose* $0 < \mu_2 = \int \omega^2\nu(d\omega) < \infty$ *and* $\mu_4 = \int \omega^4\nu(d\omega) < \infty$. *Then*

$$\frac{1}{1+T^2\mu_2} \le \mathcal{L}(T) \le 1 - \frac{T^2\mu_2^2}{\mu_2 + T^2\mu_4}. \tag{11.4}$$

For the present ensemble, $\mu_2 = \gamma_2/(1-\pi_\infty)$ *and* $\mu_4 = \gamma_4/(1-\pi_\infty)$. *The half-response time obeys* $T_{1/2} \ge \mu_2^{-1/2} = \tau_{\mathrm{inel}}$. *If* $\mu_4 < 2\mu_2^2$, *it also satisfies*

$$T_{1/2} \le \sqrt{\frac{\mu_2}{2\mu_2^2 - \mu_4}}. \tag{11.5}$$

If $\mu_4 \ge 2\mu_2^2$, *these two moments alone allow arbitrarily large* $T_{1/2}$ *among symmetric frequency measures without a zero atom.*

Proof. Set $X = \omega^2$. Jensen's inequality for $(1+T^2X)^{-1}$ gives the lower bound. Cauchy–Schwarz gives

$$\mathbb{E}\frac{X}{1+T^2X} \ge \frac{(\mathbb{E}X)^2}{\mathbb{E}[X(1+T^2X)]},$$

which gives the upper bound after using $\mathcal{L} = 1 - T^2\mathbb{E}[X/(1+T^2X)]$. Monotonicity and both endpoint limits follow by dominated convergence and $\nu(\{0\}) = 0$. Solving the upper bound for $\mathcal{L}(T) \le 1/2$ proves (11.5).

For the final assertion, choose $0 < a < \mu_2$ and let X have two values a and $b = (\mu_4 - a\mu_2)/(\mu_2 - a)$, with probability $p = (b-\mu_2)/(b-a)$ at a. This law has exactly $\mathbb{E}X = \mu_2$ and $\mathbb{E}X^2 = \mu_4$. Place each mass symmetrically at $\pm\sqrt{X}$. As $a \downarrow 0$, $p \to 1 - \mu_2^2/\mu_4 \ge 1/2$; the remaining mass at $b \to \mu_4/\mu_2$ makes the limiting $\mathcal{L}(T)$ strictly greater than $1/2$ for every finite T, including the equality case. Its half-response time therefore diverges, although the two moments stay fixed and no member of the sequence has a zero-frequency atom. □

For the measured charge ensemble at $\kappa = 64$, the inelastic moment ratios $\widehat{\mu}_4/\widehat{\mu}_2^2$ are 128.3, 301.0, 517.7, and 825.7 for $N = 10, 14, 18, 22$. The last has a 95% whole-sample bootstrap interval $[770.2, 893.0]$. These are ratios of empirical ensemble moments with the elastic component removed before normalization. They lie well inside the range where two moments alone give no uniform upper half-response time.

The exact fourth moment adds a finite-time constraint to the curvature bound, and also identifies its limitation. Low-frequency inelastic weight can delay relaxation while leaving prescribed low-order frequency moments unchanged. Section 12 examines a concrete mechanism for this separation through near-resonant mixing of quadratic occupation states.

12 Resolved resonances and the time scale of residual memory

The fixed-sample expansion in Proposition J.1 is singular at a quadratic resonance. We now resolve this singularity exactly for an isolated pair, derive its disorder-averaged consequence, and measure the accuracy of the resulting approximation against the full Hamiltonian. The distinction between these three steps is essential: the pair calculation is exact, its averaging theorem has explicit probabilistic hypotheses, and the all-pair approximation to SYK is tested without assuming that these hypotheses control the full many-body model.

12.1 Exact pair weights and a local isolation criterion

Put $\epsilon = \kappa^{-1}$ and temporarily use $\widetilde{H} = B^\circ + \epsilon A^\circ$. Its eigenvectors coincide with those of H_κ°, while its frequencies must be divided by $\sqrt{1+\epsilon^2}$ to recover the physical time convention. For an unordered pair n, l of quadratic occupation states, define

$$\Delta_{nl} = b_n - b_l, \qquad d_{nl} = A^\circ_{nn} - A^\circ_{ll}, \qquad a_{nl} = A^\circ_{nl}, \tag{12.1}$$

$$\delta_{nl} = \Delta_{nl} + \epsilon d_{nl}, \qquad \Omega_{nl}^2 = \delta_{nl}^2 + 4\epsilon^2 |a_{nl}|^2, \qquad L_{nl} = \frac{4\epsilon^2 |a_{nl}|^2}{\Omega_{nl}^2}. \tag{12.2}$$

Write $h_{nl} = d_H(n,l)$ and $w_{nl} = 2h_{nl}/(mD)$. If this two-dimensional block is isolated and all other occupation states are frozen, then

$$\begin{aligned} 1 - \overline{C}_{\widetilde{H}}(t) &= w_{nl} L_{nl} [1 - \cos(\Omega_{nl} t)], \\ 1 - p_\infty = w_{nl} L_{nl}, &\qquad -\overline{C}''_{\widetilde{H}}(0) = 4 w_{nl} \epsilon^2 |a_{nl}|^2. \end{aligned} \tag{12.3}$$

If $\Omega_{nl} = 0$, this block has no inelastic weight and we set $L_{nl} = 0$. To verify (12.3), remove the scalar part of the pair Hamiltonian and rotate the transverse Pauli component into the x direction. Its axis makes an angle with the z axis whose squared sine is L_{nl}. A charge with $q_a(n) = q_a(l)$ is constant on this block. For each of the h_{nl} charges with opposite signs, the block trace contributes $2L_{nl}[1 - \cos(\Omega_{nl} t)]$ to its loss. Division by mD gives the stated weight. This also fixes the factor of two associated with unordered pairs.

The expressions add exactly for disjoint isolated blocks. Summing over *all* nonzero quartic

edges instead defines the unfitted prediction

$$S_{\mathrm{pair}}(\epsilon) = \sum_{n<l} w_{nl} L_{nl},$$
$$C_{\mathrm{pair}}(t) = 1 - \sum_{n<l} w_{nl} L_{nl} \left[1 - \cos\left(\frac{\Omega_{nl} t}{\sqrt{1+\epsilon^2}}\right)\right]. \tag{12.4}$$

This sum is neither an exact decomposition nor a bound for the full model. At a fixed nonresonant sample, however, its leading ϵ^2 coefficient agrees exactly with (J.1). Its initial curvature agrees with the full-model curvature at every ϵ, since

$$-C''_{\mathrm{pair}}(0) = \frac{4\epsilon^2}{1+\epsilon^2} \sum_{n<l} w_{nl} |a_{nl}|^2 = \frac{1}{m} \sum_a \|[H^\circ_\kappa, Q_a]\|^2_{\mathrm{HS}}. \tag{12.5}$$

Here the Hilbert–Schmidt norm uses the normalized block trace. Resumming the detuning changes the elastic weight and higher time coefficients while preserving this exact second moment.

A concrete sufficient condition for local pair accuracy is available from a block resolvent. Write $H = \left(\begin{smallmatrix} H_P & V \\ V^\dagger & H_R \end{smallmatrix}\right)$, where P projects onto the pair and H_P has eigenvalue gap $\Omega > 0$. Let ψ be a normalized eigenvector of H with eigenvalue E and

$$\operatorname{dist}(E, \operatorname{spec} H_R) \geq \eta > 0, \qquad \nu = \|V\|_{\mathrm{op}}, \qquad \sigma = \nu^2/\eta < \Omega/2.$$

Then there is a unique eigenvalue of H_P within σ of E. For its normalized eigenvector ϕ, every charge that is block diagonal with respect to $P \oplus R$ and has operator norm at most one satisfies

$$|\langle \psi, Q\psi\rangle - \langle \phi, Q\phi\rangle| \leq \frac{2\nu^2}{\eta^2} + \frac{2\sigma}{\Omega - \sigma}. \tag{12.6}$$

Indeed, the eliminated component is $(E - H_R)^{-1} V^\dagger P\psi$, of norm at most $(\nu/\eta)\|P\psi\|$. The normalized pair component obeys a 2×2 eigenvalue equation with self-energy $V(E - H_R)^{-1}V^\dagger$, whose norm is at most σ. Its component along the other eigenvector of H_P is bounded by $\sigma/(\Omega - \sigma)$. The trace-distance bound for pure states and the outside probability give (12.6). The difference between the squared charge expectations is at most twice this bound. A sparse graph of near-resonant pairs alone does not imply the spectral separation η or a small self-energy; the numerical graph diagnostic below therefore does not certify a many-body error bound.

12.2 An averaging theorem and two distinct time scales

We next consider an ensemble of exactly isolated two-level problems. The detuning Δ, matrix element a, diagonal shift d, and nonnegative charge weight $w \leq 1$ may be dependent. This dependence is kept explicitly in the conditional density of Δ.

Theorem 12.1 (Resonance averaging for an isolated pair)**.** *Suppose Δ, conditional on (a, d, w), has a density $\rho(\Delta \mid a, d, w)$ bounded by a deterministic finite constant and continuous at zero almost surely. Assume d is finite almost surely, and set*

$$A_0 = \mathbb{E}[w|a|\rho(0 \mid a, d, w)] > 0, \qquad B_0 = \mathbb{E}[w|a|^2] \in (0, \infty). \tag{12.7}$$

For

$$L_\epsilon = \frac{4\epsilon^2|a|^2}{(\Delta+\epsilon d)^2+4\epsilon^2|a|^2}, \qquad \Omega_\epsilon^2 = (\Delta+\epsilon d)^2+4\epsilon^2|a|^2,$$

let $D_\epsilon = \mathbb{E}[wL_\epsilon]$ *be the mean elastic deficit and* $G_\epsilon^2 = \mathbb{E}[wL_\epsilon\Omega_\epsilon^2]$ *the mean initial curvature. As* $\epsilon \to 0$,

$$D_\epsilon \sim 2\pi A_0|\epsilon|, \qquad G_\epsilon^2 = 4B_0\epsilon^2, \qquad \tau_{\mathrm{inel},\epsilon}^2 := \frac{D_\epsilon}{G_\epsilon^2} \sim \frac{\pi A_0}{2B_0|\epsilon|}. \tag{12.8}$$

Moreover, uniformly for $s \geq 0$,

$$\Phi_\epsilon(s) := \frac{\mathbb{E}[wL_\epsilon\{1-\cos(\Omega_\epsilon s/|\epsilon|)\}]}{D_\epsilon} \longrightarrow \Phi(s) = \frac{\mathbb{E}[w|a|\rho(0 \mid a,d,w)F(s|a|)]}{A_0}, \tag{12.9}$$

$$F(z) = \frac{1}{\pi}\int_{\mathbb{R}} \frac{1-\cos(2z\sqrt{1+y^2})}{1+y^2}\,dy. \tag{12.10}$$

For each $\theta \in (0,1)$, *the first time at which the normalized inelastic loss reaches* θ *obeys*

$$t_\theta = \Theta(|\epsilon|^{-1}), \qquad t_\theta/\tau_{\mathrm{inel},\epsilon} = \Theta(|\epsilon|^{-1/2}). \tag{12.11}$$

These statements concern the isolated-pair ensemble and finite sums of disjoint blocks satisfying the same hypotheses.

Proof. The terms with $a = 0$ contribute zero. Otherwise make the substitution $\Delta = 2|\epsilon||a|y - \epsilon d$ in the conditional expectation:

$$\frac{D_\epsilon}{|\epsilon|} = 2\mathbb{E}\left[w|a|\int_{\mathbb{R}} \frac{\rho(2|\epsilon||a|y-\epsilon d \mid a,d,w)}{1+y^2}\,dy\right]. \tag{12.12}$$

The density bound and Cauchy–Schwarz imply an integrable dominating function, since $\mathbb{E}[w|a|] < \infty$. Continuity at zero then gives $2\pi A_0$. The identity for G_ϵ^2 follows by direct cancellation of the denominator. The same substitution in the loss introduces the bounded factor $1-\cos(2s|a|\sqrt{1+y^2})$. Replacing the transformed density by its value at zero costs at most twice its weighted L^1 difference, independently of s. This proves uniform convergence in (12.9), including the normalization by D_ϵ.

The kernel is continuous, $F(0) = 0$, and $0 \leq F \leq 2$. The substitution $u = \sqrt{1+y^2}$ expresses its cosine term as the Fourier transform of an integrable density on $[1,\infty)$, so $F(z) \to 1$ as $z \to \infty$. Weighted dominated convergence gives $\Phi(0) = 0$ and $\Phi(s) \to 1$. There are thus constants $0 < c_\theta < C_\theta < \infty$ for which $\Phi(s) < \theta$ throughout $[0, c_\theta]$ and $\Phi(C_\theta) > \theta$, with strict margins. Uniform convergence and continuity of the finite-ϵ loss place its first crossing between $c_\theta/|\epsilon|$ and $C_\theta/|\epsilon|$. No monotonicity assumption is used. Equation (12.8) completes the proof. □

For each fixed nonzero detuning the deficit is quadratic in ϵ. Averaging gives a linear term because resonant pairs can have order-one mixing. In fact,

$$\lim_{\epsilon\to 0} \frac{\mathbb{E}\left[w\,\mathbf{1}_{\{|\Delta+\epsilon d|\leq 2|\epsilon a|\}}\right]}{|\epsilon|} = 4A_0.$$

The substitution in (12.12), restricted to $-1 \leq y \leq 1$ and applied to the indicator, proves this limit. On this event $L_\epsilon \geq 1/2$ almost surely. The mass in the display is weighted by the same charge factor w as the deficit.

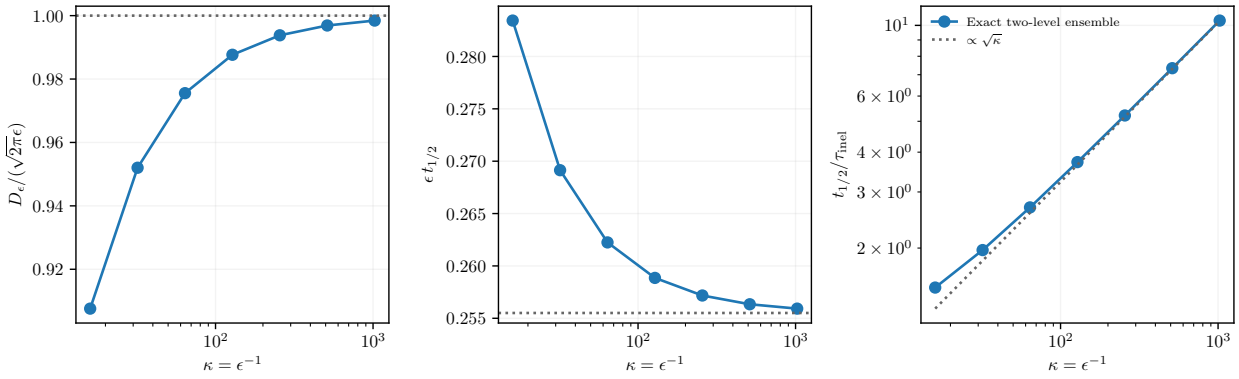


Figure 10: An exactly defined two-level ensemble with Gaussian detuning. The elastic deficit approaches its linear resonance law (left), the first half-loss occurs at a nonzero limiting value of ϵt (middle), and its ratio to the curvature time grows as $\epsilon^{-1/2}$ (right). This figure tests Theorem 12.1; it is not a fit to SYK data.

There is also a nonuniformity in time. Rescaling $u = 2zy$ in (12.10) gives

$$\frac{F(z)}{z} = \frac{2}{\pi}\int_{\mathbb{R}} \frac{1-\cos\sqrt{u^2+4z^2}}{u^2+4z^2}\,du \longrightarrow 2,$$

using the integrable majorant $\min(1/2, 2/u^2)$. Its integral times $2/\pi$ bounds $F(z)/z$ uniformly for $z > 0$. Since ρ is bounded and $\mathbb{E}[w|a|^2] < \infty$, dominated convergence over the pair parameters gives

$$\lim_{s\downarrow 0}\frac{\Phi(s)}{s} = \frac{2\mathbb{E}[w|a|^2\rho(0 \mid a,d,w)]}{A_0}.$$

Thus the limiting loss has a linear cusp, although the initial loss at each fixed nonzero ϵ is quadratic by (12.8). The curvature-based lower time scale is therefore parametrically smaller than a fixed fractional relaxation time in this controlled reduced model.

The kernel also has the finite-interval representation $F(s) = \int_0^{2s} J_0(u)\,du$, where J_0 is the Bessel function. Indeed, Tonelli's theorem applied to (12.10) gives its Laplace transform $2/[p\sqrt{p^2+4}]$ for $p > 0$, which is also the transform of the Bessel integral. This furnishes a finite-interval check of the limiting half-loss time.

As an explicit check, take $w = a = 1$, $d = 0$, and a standard normal Δ in the Hamiltonian $(\Delta/2)\sigma_z + \epsilon\sigma_x$. Gaussian integration gives

$$D_\epsilon = \sqrt{2\pi}|\epsilon|\ \mathrm{erfcx}(\sqrt{2}|\epsilon|), \qquad \tau_{\mathrm{inel},\epsilon} \sim \frac{(2\pi)^{1/4}}{2\sqrt{|\epsilon|}}. \tag{12.13}$$

The first solution of $F(s) = 1/2$ is $s = 0.255505922$. At $\epsilon^{-1} = 16, 64, 256, 1024$, direct integration gives scaled half-loss times $\epsilon t_{1/2} = 0.283428, 0.262244, 0.257176, 0.255923$. The corresponding ratios $t_{1/2}/\tau_{\mathrm{inel},\epsilon}$ are $1.5033, 2.6832, 5.2142, 10.3534$. The asymptotic ratio is $0.322765\sqrt{\epsilon^{-1}}$. We evaluate the oscillatory tail after setting $u = \sqrt{1+y^2}$; tightening the adaptive Fourier quadrature tolerance from 10^{-10} to 10^{-12} changes every scaled half-loss root by less than 6×10^{-13}. These are deterministic integration checks, separate from the SYK sample statistics.

N	D_{64}	S_{64}/D_{64}	S_{2048}/D_{2048}	$f_{4,64}$
10	0.02630	1.0007 [0.9972, 1.0042]	1.00005	0.9540
14	0.06580	1.0049 [0.9947, 1.0142]	1.00023	0.9827
18	0.11599	0.9683 [0.9553, 0.9804]	0.98922	0.9876
22	0.18693	0.8863 [0.8650, 0.9107]	0.97094	0.9913

Table 7: The all-pair prediction compared with exact full-model dephasing, with $D_\kappa = \mathbb{E}[1-p_\infty]$ and $S_\kappa = \mathbb{E}S_{\rm pair}(1/\kappa)$. Brackets are paired pointwise 95% bootstrap intervals. The last column is the Hamming-distance-four fraction of S_{64}. Large-κ agreement improves on these fixed samples; it does not establish an ensemble asymptotic exponent.

12.3 Paired full-model tests and their limits

We reconstruct A° and B° from all saved charge directions: $256, 256, 128, 32$ independent samples at $N = 10, 14, 18, 22$, respectively. The same directions are used at every coupling. The all-pair sum includes the diagonal shifts in (12.2) and has no fitted parameters. Exact dephasing at $\kappa = 4, 16, 64$ is reused; 3360 additional diagonalizations extend the paired calculation to $\kappa = 128, 256, 512, 1024, 2048$. Four additional diagonalizations at $\kappa = 64$, one per size, reproduce the earlier elastic deficits to 1.9×10^{-14}, and (12.5) is verified to relative error 4.5×10^{-16}. Confidence intervals below use 2000 whole-sample bootstrap resamples, paired across couplings; they quantify sampling error and do not bound the approximation error.

Quartic matrix elements connect occupations at Hamming distance two or four. At $\kappa = 64$, four-mode flips account for 95.4% to 99.1% of the pair deficit; at $\kappa = 2048$ they exceed 99.9% for all four sizes. The unresummed perturbative mean is already 4.449 at $N = 22$, $\kappa = 64$, compared with the exact deficit 0.18693 and the resolved pair prediction 0.16568. At $N = 10$ the same unresummed mean is 260.1, dominated by exceptionally small detunings. Resolving individual resonances removes these artificial divergences, but summing overlapping pairs can itself fail: at $\kappa = 4$, its predicted deficit is $1.137, 1.876, 2.777$ for $N = 14, 18, 22$, exceeding the physical upper bound of one.

To quantify a source of this failure, connect two occupations whenever $|\delta_{nl}| \le 2|\epsilon a_{nl}|$. At $N = 22$ the fraction of vertices incident to at least two such edges is $0.9472, 0.3536, 0.03076, 0.001862$ at $\kappa = 4, 16, 64, 256$, respectively. At $\kappa \ge 1024$ this fraction is zero in these sampled graphs, while the pair deficit still underestimates the exact value by 4.11% at $\kappa = 1024$ and 2.91% at $\kappa = 2048$. This threshold graph alone does not explain the remaining discrepancy. At $\kappa = 2048$ the paired 95% interval for the $N = 22$ ratio is $[0.9242, 0.9939]$, so the remaining discrepancy is resolved at the pointwise level.

Elastic agreement is not sufficient for dynamical accuracy. At ten prespecified times spanning $0 \le t/\tau_{N,\kappa} \le 128$, we compare (12.4) with the exact charge correlator, after subtracting each ensemble's own elastic weight and normalizing the remaining weight. At $N = 14$, $\kappa = 64$, the largest observed absolute difference is 0.02425. At $N = 22$, $\kappa = 64$, it reaches 0.2022 at $t/\tau_{N,\kappa} \simeq 16.45$, with paired pointwise 95% interval $[0.1827, 0.2217]$ for the exact-minus-pair difference at that time. The time was selected by maximizing the observed discrepancy over ten points. The interval has no simultaneous coverage guarantee for the maximum. The curvatures agree before inelastic normalization; the later curves differ even after each is normalized by its own inelastic weight.

Four-mode flips dominate the predicted elastic deficit at large deformation. At the two larger sizes the full-model deficits still exceed the pair sums at $\kappa = 2048$. Extending Theorem 12.1

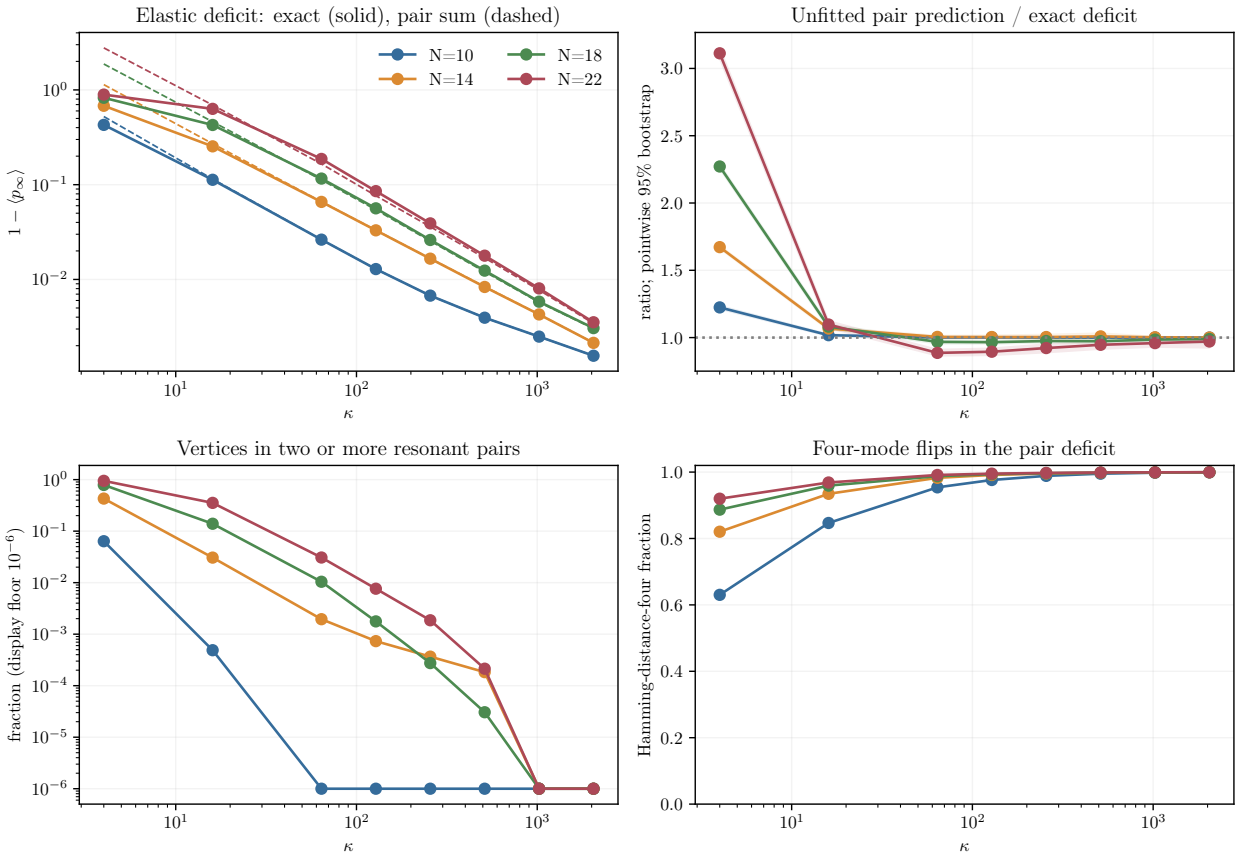


Figure 11: Unfitted resonance predictions from the same directions as the full dephasing calculation. The panels show the mean elastic deficit, the paired prediction-to-exact ratio, the fraction of occupations in multiple threshold-resonant pairs, and the fraction of the predicted deficit carried by four-mode flips. Shading in the ratio panel gives pointwise 95% whole-sample bootstrap intervals. Exact zeros in the overlap fraction are displayed at 10^{-6}, solely for the logarithmic axis; they remain zero in the released data.

to the full Hamiltonian would require bounds on the effect of the complementary states and on the distribution of near-resonant detunings.

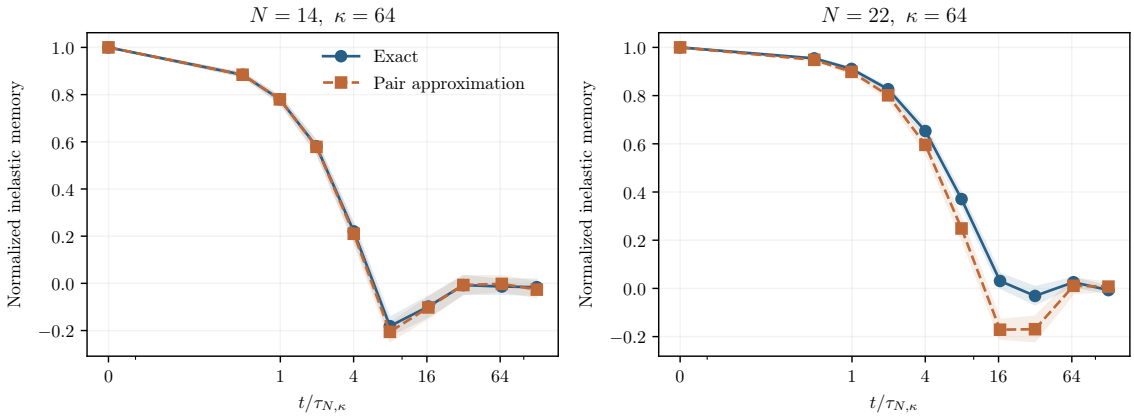


Figure 12: Normalized inelastic memory at $\kappa = 64$, with ensemble subtraction performed before normalization. The pair approximation reproduces much of the $N = 14$ curve but decays too rapidly over part of the $N = 22$ curve. Bands are pointwise 95% paired whole-sample bootstrap intervals. Matching the exact short-time curvature does not fix the later curve.

13 Discussion

Fixing the coupling norms removes one source of spectral fluctuations. The cubic trace gives the first remaining coefficient at short times, and the fourth trace takes its place at the quadratic endpoint. For filtered traces, the two numerical experiments answer different questions. Independent repeats at fixed radii separate the directional cumulant from covariance mixing. At $N = 14$, $\kappa = 4$, and $t = 4$, the three terms in the normalized fourth cumulant of the conditionally centered trace are 0.8098, 0.00494, and 0.00359. In the regression experiment, prediction by low-degree moment features accounts for most of the variance at $t = 0$ but leaves a fourth cumulant at later times. To measure the fourth cumulant at fixed higher moments would require their conditional spectral law or a controlled approximation to it.

The four-size spacing scan resolves a shift of the crossover to larger couplings and a widening between $N = 10$ and 18. A finer grid changes the two smaller-size width estimates by about 0.04. At $N = 14$ and $\kappa = 8$ it takes direct averaging over radial shifts to determine even the sign of the small Gaussian-minus-directional correction. The Gaussian mean is analytic in a strip at every finite size, but the available strip bound grows with N. An inference about a limiting transition would need control of that size dependence.

For the quadratic charges, dephasing and short-time curvature constrain different parts of the frequency distribution. At $N = 22$, $\kappa = 64$, the Hamiltonian accounts for 0.09089 of the charge weight, while the measured total conserved fraction is 0.8131. The all-time floor of the empirical correlation is consequently about 0.6261. The normalized inelastic part reaches half-loss at about 13.85 in units of its estimated inelastic curvature time. For an isolated pair the separation between these times follows from the detuning average. In the full ensemble, four-mode occupation changes carry most of the predicted pair deficit. Even when no occupation belongs to two threshold-resonant pairs in the sample, a discrepancy in the elastic weight remains. Equation (12.6) identifies the additional spectral separation and self-energy estimates that would give control of an individual pair.

The relation between the two measurements can be stated at the level of spectral measures.

Averaging over the m charges gives the two-energy measure

$$\mathcal{M}_Q(dE, dE') = \frac{1}{mD} \sum_{a,\alpha,\beta} |(Q_a)_{\alpha\beta}|^2 \, \delta_{E_\alpha}(dE)\delta_{E_\beta}(dE').$$

Its image under $(E, E') \mapsto E - E'$ is the charge frequency measure. The isospectral Hamiltonians $(\Omega/2)\sigma_z$ and $(\Omega/2)\sigma_x$, for example, have correlations 1 and $\cos(\Omega t)$ for the same charge σ_z. Connecting the spectral cumulants to charge memory in SYK therefore requires the joint law of energies and transition weights.

Data and code. The supplement contains the numerical programs, seed rules and tabulated estimates. The programs generate the realization-level spectra and bootstrap arrays used in the analyses. The distributed data consist of summaries. In the charge simulations, reproducing the individual Hamiltonians across eigensolver implementations also requires the ordered, signed quadratic normal modes used in the original run. See `anc/reproduce.json` for the calculation and the available inputs.

A Radial width fluctuations and short-time baselines

A.1 Width fluctuations and their own crossover

Put

$$w_4(\kappa) = \frac{1}{1+\kappa^2}, \qquad w_2(\kappa) = \frac{\kappa^2}{1+\kappa^2}.$$

The width in (3.3) is the weighted sum $s_\kappa^2 = w_4 R_4^2 + w_2 R_2^2$.

Proposition A.1 (Joint width cumulants)**.** *For $r \geq 2$ and arbitrary $\kappa_1, \ldots, \kappa_r$,*

$$\operatorname{cum}(s_{\kappa_1}^2, \ldots, s_{\kappa_r}^2) = 2^{r-1}(r-1)! \left[\frac{\prod_{j=1}^r w_4(\kappa_j)}{d_4^{r-1}} + \frac{\prod_{j=1}^r w_2(\kappa_j)}{d_2^{r-1}} \right]. \tag{A.1}$$

In particular,

$$\operatorname{Var}(s_\kappa^2) = \frac{2}{(1+\kappa^2)^2} \left(\frac{1}{d_4} + \frac{\kappa^4}{d_2} \right). \tag{A.2}$$

The two variance contributions are equal at

$$\kappa_{\mathrm{rad}} = \left(\frac{d_2}{d_4} \right)^{1/4} = \left[\frac{12}{(N-2)(N-3)} \right]^{1/4} \sim 12^{1/4} N^{-1/2}. \tag{A.3}$$

Proof. The cumulants of a gamma variable R_q^2 with shape $d_q/2$ and scale $2/d_q$ are $\operatorname{cum}_r(R_q^2) = 2^{r-1}(r-1)! d_q^{1-r}$. Multilinearity and independence remove every mixed term in the joint cumulant and give (A.1). The remaining claims follow by taking $r = 2$ and equating its two summands. □

The scale κ_{rad} marks a change in the source of sample-width fluctuations. Its derivation uses no microscopic level statistics. It therefore supplies a model-internal example of a scale with a definite N-dependence that carries no implication of a chaos transition. The variance itself is minimized at $\kappa^2 = d_2/d_4$, which is a different location from the equality of its two contributions.

A.2 Exact short-time spectral fluctuations

To display the observable consequence of width disorder, use the normalized, unfiltered trace

$$z_\kappa(t) = \operatorname{tr}_D e^{-itH_\kappa}, \qquad \delta z_\kappa(t) = z_\kappa(t) - \mathbb{E} z_\kappa(t),$$

and define

$$C_z(t) = \mathbb{E}|\delta z_\kappa(t)|^2, \qquad P_z(t) = \mathbb{E}[\delta z_\kappa(t)^2], \tag{A.4}$$

$$Q_{4,z}(t) = \mathbb{E}|\delta z_\kappa(t)|^4 - 2C_z(t)^2 - |P_z(t)|^2. \tag{A.5}$$

These are trace-normalized quantities; multiplying the trace by D multiplies C_z, P_z by D^2 and $Q_{4,z}$ by D^4.

Theorem A.2 (Short-time width contribution)**.** *At fixed even $N \geq 10$, as $t \to 0$,*

$$C_z(t) = \frac{t^4}{4} \operatorname{Var}(s_\kappa^2) + O(t^6), \qquad P_z(t) = \frac{t^4}{4} \operatorname{Var}(s_\kappa^2) + O(t^6), \tag{A.6}$$

$$Q_{4,z}(t) = \frac{t^8}{16} \operatorname{cum}_4(s_\kappa^2) + O(t^{10}). \tag{A.7}$$

In particular,

$$\lim_{t\to 0} \frac{Q_{4,z}(t)}{C_z(t)^2} = 12\, \frac{w_4^4/d_4^3 + w_2^4/d_2^3}{(w_4^2/d_4 + w_2^2/d_2)^2}. \tag{A.8}$$

For the fixed-radius ensemble, $\operatorname{Var}_\circ(\operatorname{tr}_D(H_\kappa^\circ)^2) = 0$*, and*

$$\operatorname{Var}_\circ\big(\operatorname{tr}_D e^{-itH_\kappa^\circ}\big) = O(t^6). \tag{A.9}$$

Proof. Every Hamiltonian is traceless in the chosen block. Taylor expansion gives

$$z_\kappa(t) = 1 - \tfrac{1}{2}t^2 s_\kappa^2 + \tfrac{i}{6}t^3 \operatorname{tr}_D H_\kappa^3 + O_{L^p}(t^4)$$

for every finite p. The L^p remainder follows from finite Gaussian moments of the finite-dimensional matrix norm; the analogous fixed-radius norm is bounded. Centering yields

$$\delta z_\kappa(t) = -\tfrac{1}{2}t^2(s_\kappa^2 - 1) + \tfrac{i}{6}t^3\big(\operatorname{tr}_D H_\kappa^3 - \mathbb{E}\operatorname{tr}_D H_\kappa^3\big) + O_{L^p}(t^4).$$

The leading real and imaginary terms have no cross contribution to the modulus squared. In P_z, the potential order-t^5 term vanishes by the ensemble symmetry $H \mapsto -H$. The same symmetry makes all expectations entering the real fourth cumulant even in t. Finite Gaussian moments also permit differentiation of these expectations through order ten, so the odd-order term vanishes with an $O(t^{10})$ remainder. The leading fluctuation is real, so the Wick subtraction is $3\operatorname{Var}(s_\kappa^2)^2$ at order $t^8/16$. This proves (A.6)–(A.7). Proposition A.1 gives (A.8). In the fixed-radius ensemble, the centered quadratic term is identically zero, leaving an $O_{L^2}(t^3)$ amplitude. □

Theorem A.2 describes the early-time expansion and supplies an exact calibration of the collective contribution. Its time interval is distinct from an RMT ramp. A nonzero fourth excess already occurs at $\kappa = 0$, where its limiting value is $12/d_4$, and equals $12/d_2$ at the quadratic endpoint. The function in (A.8) is not monotone: direct differentiation gives its minimum $12/(d_2 + d_4)$ at $\kappa^2 = d_2/d_4$. These values arise entirely from the coupling radii.

A.3 Several interaction orders

The same representation applies to independent Gaussian interaction families of degrees in a finite set $\mathcal{Q}$, provided their monomials are mutually orthogonal for the chosen trace. If

$$H_{\boldsymbol{a}} = \frac{\sum_{q\in\mathcal{Q}} a_q A_q}{\sqrt{\sum_q a_q^2}}, \qquad A_q = R_q A_q^{\circ},$$

then

$$s_{\boldsymbol{a}}^2 = \frac{\sum_q a_q^2 R_q^2}{\sum_q a_q^2}, \qquad \frac{H_{\boldsymbol{a}}}{s_{\boldsymbol{a}}} = \sum_q \widetilde{a}_q A_q^{\circ}, \quad \widetilde{a}_q = \frac{a_q R_q}{(\sum_p a_p^2 R_p^2)^{1/2}}. \tag{A.10}$$

With a reference degree q_0 and nonzero coefficients,

$$\log\left|\frac{\widetilde{a}_q}{\widetilde{a}_{q_0}}\right| = \log\left|\frac{a_q}{a_{q_0}}\right| + \log R_q - \log R_{q_0}.$$

The logarithmic coupling displacements have covariance

$$\operatorname{Cov}(\eta_q, \eta_p) = \frac{1}{4}\left[\delta_{qp}\psi_1(d_q/2) + \psi_1(d_{q_0}/2)\right], \qquad q, p \neq q_0. \tag{A.11}$$

This follows from independence of the radii. It identifies a correlated random displacement of a multi-parameter crossover surface, rather than an independent error assigned separately to each observable.

B Conditional means, cumulant estimators, and spectral covariance

B.1 Conditional means and globally centered traces

Numerical estimates formed directly from independent spectra center Z by its disorder mean. Define

$$Y(t) = Z(t) - \mathbb{E}Z(t) = R(t) + A(t), \qquad A(t) = m_{\mathcal{G}}(t) - \mathbb{E}m_{\mathcal{G}}(t). \tag{B.1}$$

Conditional centering therefore changes the observable whenever the conditional mean varies. In particular,

$$\begin{aligned} C_Y(t,u) &= \mathbb{E}C_{\mathcal{G}}(t,u) + C_A(t,u), \\ P_Y(t,u) &= \mathbb{E}P_{\mathcal{G}}(t,u) + P_A(t,u). \end{aligned} \tag{B.2}$$

At equal times the fourth-order correction has the following explicit form. We use the bilinear covariance $\operatorname{Cov}_b(U,V) = \mathbb{E}[UV] - \mathbb{E}U\,\mathbb{E}V$.

Proposition B.1 (Correction for a random conditional mean)**.** *At a fixed time, suppress time arguments and put* $T_{\mathcal{G}} = \mathbb{E}[R|R|^2 \mid \mathcal{G}]$*. Then*

$$Q_Y = Q_R + Q_A + 4\operatorname{Cov}(|A|^2, c_{\mathcal{G}}) + 2\operatorname{Re}\operatorname{Cov}_b(\overline{A}^{\,2}, P_{\mathcal{G}}) + 4\operatorname{Re}\mathbb{E}[\overline{A}T_{\mathcal{G}}]. \tag{B.3}$$

Proof. Use $\mathbb{E}[R \mid \mathcal{G}] = 0$ to expand

$$\mathbb{E}[|A+R|^4 \mid \mathcal{G}] = |A|^4 + \mathbb{E}[|R|^4 \mid \mathcal{G}] + 4|A|^2 c_{\mathcal{G}} + 2\,\mathrm{Re}(\overline{A}^2 P_{\mathcal{G}}) + 4\,\mathrm{Re}(\overline{A} T_{\mathcal{G}}).$$

The second moments are $C_Y = C_R + C_A$ and $P_Y = P_R + P_A$. Subtracting $2C_Y^2 + |P_Y|^2$ and collecting terms gives (B.3). □

Thus a globally estimated fourth cumulant has an exact decomposition into directional fourth cumulants, fluctuations of conditional covariances, and conditional-mean terms. Removing the mean of the intensity $|Z|^2$ does not perform the conditional centering in (4.5). In the numerical results below we state explicitly which centering is used.

B.2 Unbiased second- and fourth-order estimators

Let (z_s, w_s), $s = 1, \dots, n$, be independent copies of $(Z(t), Z(u))$, with $n \geq 4$. Write $d_s = z_s - \overline{z}$, $e_s = w_s - \overline{w}$, and

$$a = \frac{1}{n}\sum_s |d_s|^2, \qquad b = \frac{1}{n}\sum_s |e_s|^2, \qquad g = \frac{1}{n}\sum_s d_s \overline{e_s},$$
$$p = \frac{1}{n}\sum_s d_s e_s, \qquad h = \frac{1}{n}\sum_s |d_s|^2 |e_s|^2. \tag{B.4}$$

The overbar on $\overline{z}, \overline{w}$ denotes the sample mean; elsewhere it denotes complex conjugation.

Theorem B.2 (Finite-sample spectral cumulants)**.** *The estimators*

$$\widehat{C}_Y(t,u) = \frac{n}{n-1} g, \qquad \widehat{P}_Y(t,u) = \frac{n}{n-1} p, \tag{B.5}$$

$$\widehat{Q}_Y(t,u) = \frac{n^2}{(n-1)(n-2)(n-3)} \left\{ (n+1)h - (n-1)\big(ab + |g|^2 + |p|^2\big) \right\} \tag{B.6}$$

are unbiased for the quantities in (4.2) and (4.3), respectively. At equal times,

$$\widehat{Q}_Y(t,t) = \frac{n^2}{(n-1)(n-2)(n-3)} \left\{ (n+1)\frac{1}{n}\sum_s |d_s|^4 - (n-1)\left[2a^2 + \left| \frac{1}{n}\sum_s d_s^2 \right|^2 \right] \right\}. \tag{B.7}$$

Proof. The second-order assertion is the usual sample-covariance identity. For completeness, the fourth-order assertion can be checked directly for four possibly complex variables $X_1, \dots, X_4$. Translation invariance permits us to suppose $\mathbb{E}X_i = 0$. Put

$$\mu_{1234} = \mathbb{E}[X_1 X_2 X_3 X_4], \qquad S = \mu_{12}\mu_{34} + \mu_{13}\mu_{24} + \mu_{14}\mu_{23}, \quad \mu_{ij} = \mathbb{E}[X_i X_j].$$

For independent rows $X^{(s)}$, let m_{ij} and m_{1234} denote the empirical central moments with divisor n, and put $S_m = m_{12}m_{34} + m_{13}m_{24} + m_{14}m_{23}$. If $H = I - n^{-1}\mathbf{1}\mathbf{1}^{\mathsf{T}}$, then $m_{ij} = n^{-1}(X_i)^{\mathsf{T}} H X_j$. Only index patterns with no singleton contribute when these products are averaged. For a fixed row of H,

$$\sum_s H_{rs}^4 = \frac{(n-1)(n^2-3n+3)}{n^3}, \qquad \left(\sum_s H_{rs}^2\right)^2 - \sum_s H_{rs}^4 = \frac{(n-1)(2n-3)}{n^3}.$$

The all-equal pattern and the three pairings therefore give

$$\mathbb{E}m_{1234} = \frac{(n-1)(n^2-3n+3)}{n^3}\mu_{1234} + \frac{(n-1)(2n-3)}{n^3}S,$$
$$\mathbb{E}S_m = \frac{3(n-1)^2}{n^3}\mu_{1234} + \frac{(n-1)(n^2-2n+3)}{n^3}S.$$

For the second identity, the contributions to $\mathbb{E}(m_{ij}m_{kl})$ are $(n-1)^2\mu_{1234}/n^3$, $(n-1)^3\mu_{ij}\mu_{kl}/n^3$, and $(n-1)(\mu_{ik}\mu_{jl}+\mu_{il}\mu_{jk})/n^3$; summing over the three pairings gives the displayed expression. It follows that

$$\mathbb{E}[(n+1)m_{1234} - (n-1)S_m] = \frac{(n-1)(n-2)(n-3)}{n^2}(\mu_{1234} - S).$$

Apply this identity to $(X_1, X_2, X_3, X_4) = (Z(t), \overline{Z(t)}, Z(u), \overline{Z(u)})$. Then $m_{1234} = h$ and $S_m = ab + |g|^2 + |p|^2$. □

The same estimator is the fourth joint k-statistic [Spe86]. An equivalent formula, useful for arbitrary orders and for independent verification, is

$$\widehat{\mathrm{cum}}(X_1, \dots, X_r) = \sum_{\pi \in \mathcal{P}_r} (-1)^{|\pi|-1}(|\pi|-1)! \frac{1}{(n)^{\underline{|\pi|}}} \sum_{\substack{s_1,\dots,s_{|\pi|} \\ \text{all distinct}}} \prod_{j=1}^{|\pi|} \prod_{i \in B_j} X_i^{(s_j)}, \tag{B.8}$$

where $\pi = \{B_1, \dots, B_{|\pi|}\}$ and $(n)^{\underline{b}} = n(n-1)\cdots(n-b+1)$. Independence of the distinct sample rows makes the expectation of each summand the corresponding product of population moments. The moment–cumulant formula therefore proves unbiasedness whenever $n \geq r$ and the required moments exist.

The ratio $\widehat{Q}_Y/\widehat{C}_Y(t,t)^2$ is not itself unbiased. We report the unnormalized estimator together with its second-order scale, and use paired disorder resampling for uncertainty in normalized summaries and differences between ensembles. The plug-in covariance with divisor n has expectation $(1-1/n)C_Y$, so its finite-sample correction matters when comparing small connected signals.

Proposition B.3 (Estimating the conditional mixture terms)**.** *Suppose $B \geq 2$ outer data blocks have independent identically distributed radial draws. Each block contains two conditionally independent batches, each with at least four independent directional realizations from the prescribed conditional law. The directional batches are also independent across outer blocks. If $U_b^{(j)}$ and $V_b^{(j)}$ are conditionally unbiased estimators of $U_{\mathcal{G}_b}$ and $V_{\mathcal{G}_b}$ from batch $j = 1, 2$, then*

$$\widehat{\mathrm{Cov}}_{\mathbb{C}}(U, V) = \frac{1}{B}\sum_{b=1}^{B} U_b^{(1)}\overline{V_b^{(2)}} - \frac{1}{B(B-1)}\sum_{b \neq c} U_b^{(1)}\overline{V_c^{(2)}} \tag{B.9}$$

is unbiased for $\mathbb{E}[U_{\mathcal{G}}\overline{V_{\mathcal{G}}}] - \mathbb{E}U_{\mathcal{G}}\,\overline{\mathbb{E}V_{\mathcal{G}}}$. Consequently all terms in (4.8) have unbiased estimators under this nested sampling design, without knowledge of $m_{\mathcal{G}}$.

Proof. Conditional independence of the two batches makes the expectation of the first average $\mathbb{E}[U_{\mathcal{G}}\overline{V_{\mathcal{G}}}]$. Independence of distinct outer draws makes the expectation of the second average $\mathbb{E}U_{\mathcal{G}}\,\overline{\mathbb{E}V_{\mathcal{G}}}$. Use (B.5) within each batch to estimate conditional covariances and pseudocovariances, and (B.6) to estimate $Q_{\mathcal{G}}$. For real covariance or variance terms, take the real part of (B.9). Averaging the within-batch fourth cumulants estimates $\mathbb{E}Q_{\mathcal{G}}$. □

The two batches and independent outer draws are part of the proposition's assumptions. A single-layer disorder sample can estimate Q_Y, but does not by itself supply conditionally independent replicates at each pair of radii.

B.3 A common covariance measure for spectral statistics

The distinction between short- and long-range spectral probes should also respect their mathematical dependence. Number variance and the connected SFF are two linear measurements of the same second-order spectral covariance.

Proposition B.4 (Finite-window covariance identity)**.** *Let $\nu = \sum_\alpha \delta_{x_\alpha}$ be a random finite spectral measure with $\mathbb{E}\nu(\mathbb{R})^2 < \infty$. Define the finite signed measure on $\mathbb{R}^2$*

$$\mathcal{C} = \mathbb{E}(\nu \otimes \nu) - (\mathbb{E}\nu) \otimes (\mathbb{E}\nu).$$

For bounded Borel functions a, b,

$$\mathrm{Cov}_{\mathbb{C}}\left(\int a\, d\nu, \int b\, d\nu\right) = \iint a(x)\overline{b(y)}\, \mathcal{C}(dx, dy). \tag{B.10}$$

In particular, the two-time spectral covariance is obtained by $a(x) = f(x)e^{-itx}$ and $b(x) = f(x)e^{-iux}$ for a deterministic filter f.

Let I be a bounded deterministic interval, $0 < L < |I|$, and $J_L = \{v : [v - L/2, v + L/2] \subset I\}$. If interval centers are averaged uniformly on J_L, independently of the spectrum, then

$$\begin{aligned} V_I(L) &:= \frac{1}{|J_L|}\int_{J_L} \mathrm{Var}\, \nu([v - L/2, v + L/2])\, dv \\ &= \iint A_{I,L}(x, y)\, \mathcal{C}(dx, dy), \\ A_{I,L}(x, y) &:= \frac{|J_L \cap [x - L/2, x + L/2] \cap [y - L/2, y + L/2]|}{|J_L|}. \end{aligned} \tag{B.11}$$

Here $|\cdot|$ denotes Lebesgue length. For a uniform random center V independent of the spectrum, $V_I(L)$ averages the conditional count variance given V. The variance over both sources of randomness adds $\mathrm{Var}_V\, h(V)$, where $h(v) = \mathbb{E}\nu([v - L/2, v + L/2])$.

Proof. Expand the covariance in the left side of (B.10) and apply Fubini's theorem. The required integrability follows from boundedness of the test functions and $\mathbb{E}\nu(\mathbb{R})^2 < \infty$. For the second assertion take $a = b = \mathbf{1}_{[v-L/2, v+L/2]}$ and integrate over v. For fixed x, y, the two indicator functions are simultaneously one exactly on the intersection defining $A_{I,L}$. □

For a sample-dependent filter, the first identity applies instead to the random weighted measure $\nu_f = \sum_\alpha f_\alpha \delta_{x_\alpha}$ and its own covariance measure. It does not permit a random filter to be moved outside the ensemble expectation.

For a stationary unit-intensity point process whose reduced covariance measure γ has finite total variation, write

$$K^c(\tau) = \int_{\mathbb{R}} e^{-2\pi i \tau r}\, \gamma(dr).$$

Stationarity gives $\operatorname{Var}\nu([0,L]) = \int (L-|r|)_+\,\gamma(dr)$. The Fourier transform of the triangular kernel is $[\sin(\pi L\tau)/(\pi\tau)]^2$, and hence

$$\Sigma^2(L) = \int_{\mathbb{R}} K^c(\tau)\left[\frac{\sin(\pi L\tau)}{\pi\tau}\right]^2 d\tau. \tag{B.12}$$

The integral is absolutely convergent because K^c is bounded under the stated assumption. Formula (B.12) is the standard stationary relation [Meh04]; (B.11) states the corresponding finite-window identity without assuming stationarity. For Poisson statistics $\gamma = \delta_0$ and $\Sigma^2(L) = L$. If the center is a typical Poisson point under stationary Palm sampling and is included in the count, its count has the Palm distribution $1 + \text{Poisson}(L)$ [LP17, Theorem 9.4], so the variance is still L but $\mathbb{E}[(N-L)^2] = L+1$. The interval centers in our number-variance definition are independent of the levels.

If an unfolded window has nonconstant expected density, replacing the true expected count by L introduces the nonnegative term

$$\frac{1}{|J_L|}\int_{J_L} \left(\mathbb{E}\nu([v-L/2, v+L/2]) - L\right)^2 dv.$$

This squared difference in expected counts persists even for a known mean density. Together, the covariance identities explain why different scalar summaries of number variance and the SFF can cross their chosen thresholds at different couplings, even when a single underlying spectral covariance changes.

C Exact initial state and operator scales

We now keep the coefficient radii fixed and specify the quadratic operators whose autocorrelations will be measured. Work with $N = 2m \geq 10$ Majorana modes and diagonalize the quadratic Hamiltonian by a real orthogonal change of modes. In the resulting basis define

$$Q_a = 2i\widetilde{\chi}_{2a-1}\widetilde{\chi}_{2a}, \qquad Q_a^2 = I, \qquad a = 1,\dots,m. \tag{C.1}$$

These even operators commute with the quadratic Hamiltonian and preserve each parity sector. We use the normalized trace tr_D in the chosen parity block and its associated Hilbert–Schmidt norm. For $N > 8$ the quartic norm identities are identical to those obtained from the normalized trace on the full Hilbert space.

Let B° be a fixed quadratic Hamiltonian of unit Hilbert–Schmidt norm. In the orthonormal quartic Clifford basis write

$$A^\circ = \sum_{|I|=4} u_I \Gamma_I, \qquad \Gamma_I = 4\prod_{i\in I}\widetilde{\chi}_i, \qquad \sum_I u_I^2 = 1, \qquad H_r^\circ = \frac{A^\circ + rB^\circ}{\sqrt{1+r^2}}. \tag{C.2}$$

The product defining Γ_I is in increasing order. The vector u is uniform on the real unit sphere in dimension $d_4 = \binom{N}{4}$ and is independent of B°. This is precisely the conditional quartic angular distribution after radial normalization. In the Gaussian ensemble reduced above, $r = \kappa R_2/R_4$ and $H_r^\circ = H(\kappa)/s_\kappa$.

Theorem C.1 (Exact initial scales and charge-memory bound)**.** *Let $|a\rangle$ be any occupation state of B°, and let $b_{1,\mathrm{st}}^2 = \mathrm{Var}_a(H_r^\circ)$ be the first state Lanczos coefficient squared. Angular expectation at fixed B° gives*

$$\mathbb{E}_u \langle a|A^\circ|a\rangle^2 = c_N, \qquad c_N = \frac{3}{(N-1)(N-3)}, \tag{C.3}$$

$$\mathbb{E}_u b_{1,\mathrm{st}}^2 = \frac{1-c_N}{1+r^2}. \tag{C.4}$$

For a quartic index set I, let $\nu(I)$ be the number of quadratic mode pairs with exactly one index in I. Then, for every realization,

$$\|[H_r^\circ, Q_a]\|_{\mathrm{HS}}^2 = \frac{4}{1+r^2} \sum_{|I\cap\{2a-1,2a\}|=1} u_I^2, \tag{C.5}$$

$$\sum_{a=1}^{m} \|[H_r^\circ, Q_a]\|_{\mathrm{HS}}^2 = \frac{4}{1+r^2} \sum_I \nu(I) u_I^2. \tag{C.6}$$

In particular,

$$\mathbb{E}_u \|[H_r^\circ, Q_a]\|_{\mathrm{HS}}^2 = \frac{32(N-4)}{N(N-1)(1+r^2)}. \tag{C.7}$$

The infinite-temperature memory

$$C_a(t) = \mathrm{tr}_D\big(e^{itH_r^\circ} Q_a e^{-itH_r^\circ} Q_a\big) \tag{C.8}$$

obeys, for every real t,

$$C_a(t) \geq 1 - \frac{t^2}{2} \|[H_r^\circ, Q_a]\|_{\mathrm{HS}}^2, \tag{C.9}$$

$$\mathbb{E}_u C_a(t) \geq 1 - \frac{16(N-4)t^2}{N(N-1)(1+r^2)}. \tag{C.10}$$

The same identities hold in either parity block, and also with the normalized trace on the full Hilbert space.

Proof. The Clifford monomials Γ_I are Hermitian, satisfy $\Gamma_I^2 = I$, and are orthonormal in the normalized trace under the stated assumption $N > 8$. The parity-block justification is given below. Spherical symmetry gives $\mathbb{E}_u u_I u_J = \delta_{IJ}/d_4$. An occupation state has a nonzero diagonal matrix element of Γ_I exactly when I consists of two complete quadratic mode pairs. There are $\binom{N/2}{2}$ such sets, and their diagonal matrix elements have modulus one. Therefore

$$\mathbb{E}_u \langle a|A^\circ|a\rangle^2 = \frac{\binom{N/2}{2}}{\binom{N}{4}} = c_N, \qquad \mathbb{E}_u \langle a|(A^\circ)^2|a\rangle = 1.$$

Since $|a\rangle$ is an eigenstate of B°, its variance satisfies the samplewise identity

$$\mathrm{Var}_a(H_r^\circ) = \frac{\mathrm{Var}_a(A^\circ)}{1+r^2},$$

which proves (C.4).

A quartic monomial anticommutes with Q_a precisely when its index set meets $\{2a-1, 2a\}$ in one element. For those monomials the commutator is $2\Gamma_I Q_a$. Right multiplication by Q_a preserves Hilbert–Schmidt orthogonality, so squaring its norm proves (C.5); summing over a proves (C.6). There are $2\binom{N-2}{3}$ quartic sets with exactly one index in a prescribed pair. Consequently,

$$\mathbb{E}_u \|[H_r^\circ, Q_a]\|_{\mathrm{HS}}^2 = \frac{8\binom{N-2}{3}}{(1+r^2)\binom{N}{4}} = \frac{32(N-4)}{N(N-1)(1+r^2)}.$$

For $N > 8$ the normalized trace of a product of two quartic monomials agrees with its normalized trace in either parity block: a difference would require a Clifford monomial of degree N, while the product has degree at most eight. This establishes the asserted parity-block norm identities.

Finally, in an energy basis,

$$C_a(t) = \frac{1}{D}\sum_{j,k} |(Q_a)_{jk}|^2 \cos((E_j - E_k)t).$$

The weights sum to one because $Q_a^2 = I$. Using $1 - \cos x \le x^2/2$ gives

$$1 - C_a(t) \le \frac{t^2}{2D}\sum_{j,k}(E_j - E_k)^2 |(Q_a)_{jk}|^2 = \frac{t^2}{2}\|[H_r^\circ, Q_a]\|_{\mathrm{HS}}^2.$$

Angular expectation proves (C.10). The same spectral argument applies with the full trace or either parity-block trace. □

Corollary C.2 (Seed-dependent local Krylov scales)**.** *For the Liouvillian $\mathcal{L}O = [H_r^\circ, O]$ with initial operator Q_a, the first diagonal Lanczos coefficient is zero and $b_{1,\mathrm{op}}^2 = \|[H_r^\circ, Q_a]\|_{\mathrm{HS}}^2$. For every finite r, the ratio of mean squares is*

$$\frac{\mathbb{E}_u b_{1,\mathrm{op}}^2}{\mathbb{E}_u b_{1,\mathrm{st}}^2} = \frac{32(N-4)}{N(N-1)(1-c_N)} = \frac{32(N-3)}{N^2}. \tag{C.11}$$

The local curvature scales $\tau_{\mathrm{st}} = (\mathbb{E}_u b_{1,\mathrm{st}}^2)^{-1/2}$ and $\tau_{\mathrm{op}} = (\mathbb{E}_u b_{1,\mathrm{op}}^2)^{-1/2}$ therefore obey

$$\frac{\tau_{\mathrm{op}}}{\tau_{\mathrm{st}}} = \frac{N}{\sqrt{32(N-3)}} \sim \sqrt{\frac{N}{32}}. \tag{C.12}$$

Proof. Cyclicity of the trace gives $(Q_a|\mathcal{L}Q_a) = \mathrm{tr}_D(Q_a[H_r^\circ, Q_a]) = 0$, while $\|Q_a\|_{\mathrm{HS}} = 1$. The first Lanczos residual is therefore $\mathcal{L}Q_a$, proving the coefficient identity. Substitution of (C.4) and (C.7), followed by $1 - c_N = N(N-4)/((N-1)(N-3))$, proves the two ratios. □

Both state and operator Krylov complexities have the local expansion $C_K(t) = b_1^2 t^2 + O(t^4)$; the real symmetric Lanczos matrix makes this complexity an even function of time. The scales in the corollary refer to this curvature, and do not specify a peak time or a relaxation time. Their large-N separation is independent of r and is already present at the pure quartic endpoint. It is caused by the initial state and operator prescriptions. The occupation-state result also shows that at $r = 0$ its energy expectation has variance $c_N = O(N^{-2})$, although its mean energy variance is $1 - c_N$. Assigning an energy window from the expectation alone does not make this a microcanonical state. At the other endpoint its first state Lanczos coefficient vanishes by construction. Neither observation establishes a spectral transition.

For $0 < \epsilon < 1$, define the first time at which the angular-averaged memory has fallen by at least ϵ by

$$t_\epsilon = \inf\{t \geq 0 : \mathbb{E}_u C_a(t) \leq 1 - \epsilon\}, \qquad \inf \varnothing = +\infty.$$

Then

$$t_\epsilon \geq \sqrt{\frac{\epsilon N(N-1)(1+r^2)}{16(N-4)}}. \tag{C.13}$$

This is a lower bound on a specified loss of memory. It supplies neither an upper bound nor a statement that the memory eventually decays to its thermal value. It is consequently compatible with both late-time thermalization and persistent conserved components.

D Spectral weights and conditional state references

Radial conditioning fixes one source of variation in spectral observables. State diagnostics contain another source: the weights with which an initial state samples the spectrum. These two effects can be separated without assuming random-matrix statistics. We first give exact identities conditional on the Hamiltonian and its energy window. The same conditional construction provides a reference for both survival probabilities and participation in the quadratic occupation basis. We then identify what Lanczos data retain from these weights while Section 9 derives explicit short-time identities for quadratic occupation states and charges.

D.1 A common energy window for spectral and Fock observables

Let H be a Hermitian operator on a finite-dimensional complex Hilbert space, and let P be a spectral projection of rank $M \geq 1$. All state expectations condition on H, P, and the reference basis $\{|a\rangle\}$. In the SYK application we also condition on the quadratic Hamiltonian, whose normal modes define the occupation basis. Write

$$Z_P(t) = \mathrm{Tr}(Pe^{-itH}), \qquad A_\psi(t) = \langle\psi|e^{-itH}|\psi\rangle, \qquad S_\psi(t) = |A_\psi(t)|^2, \tag{D.1}$$

where ψ is Haar distributed on the unit sphere of $\mathrm{ran}\, P$. The scalar S_ψ is a survival probability. The trace Z_P in the identities below is not centered over disorder; connected spectral quantities enter only when a disorder expectation is subsequently taken.

Theorem D.1 (Conditional Haar identities)**.** *Let $z = Z_P(t)$ and $z_2 = Z_P(2t)$. Then*

$$\mathbb{E}_\psi A_\psi(t) = \frac{Z_P(t)}{M}, \tag{D.2}$$

$$\mathrm{Cov}_\psi\big(A_\psi(t), A_\psi(s)\big) = \frac{MZ_P(t-s) - Z_P(t)\overline{Z_P(s)}}{M^2(M+1)}, \tag{D.3}$$

$$\mathbb{E}_\psi S_\psi(t) = \frac{|z|^2 + M}{M(M+1)}, \tag{D.4}$$

$$\mathbb{E}_\psi S_\psi(t)^2 = \frac{|z|^4 + 2\,\mathrm{Re}(z_2\bar{z}^2) + (4M+8)|z|^2 + |z_2|^2 + 2M^2 + 6M}{M(M+1)(M+2)(M+3)}. \tag{D.5}$$

Here $\mathrm{Cov}_\psi(A, B)$ means $\mathbb{E}_\psi[(A - \mathbb{E}_\psi A)\overline{(B - \mathbb{E}_\psi B)}]$. In particular, the conditional variance of $S_\psi(t)$ is the right-hand side of (D.5) minus the square of (D.4).

In the reference basis, put

$$p_a = \frac{\langle a|P|a\rangle}{M}, \qquad D_{\text{eff}}(P) = \left(\sum_a p_a^2\right)^{-1}. \tag{D.6}$$

For every real $q > 0$,

$$\mathbb{E}_\psi \sum_a |\langle a|\psi\rangle|^{2q} = \frac{\Gamma(q+1)\Gamma(M)}{\Gamma(M+q)} \sum_a \langle a|P|a\rangle^q. \tag{D.7}$$

Consequently,

$$\mathbb{E}_\psi \operatorname{IPR}_2(\psi) = \frac{2M}{M+1}\frac{1}{D_{\text{eff}}(P)}. \tag{D.8}$$

Proof. Choose an orthonormal basis of $\operatorname{ran} P$. If g has M independent standard complex Gaussian coordinates, then $\psi = g/\|g\|$ is Haar distributed and is independent of $\|g\|$. Gaussian contraction [CŚ06] and $\mathbb{E}\|g\|^{2k} = (M)^{\overline{k}}$, where $(M)^{\overline{k}} = M(M+1)\cdots(M+k-1)$, give

$$\mathbb{E}_\psi(|\psi\rangle\langle\psi|)^{\otimes k} = \frac{1}{(M)^{\overline{k}}} \sum_{\pi\in S_k} U_\pi. \tag{D.9}$$

Here U_π permutes the tensor factors of $(\operatorname{ran} P)^{\otimes k}$. For $k = 1, 2$, contraction with the restrictions of e^{-itH} and e^{isH} gives

$$\mathbb{E}_\psi[A_\psi(t)\overline{A_\psi(s)}] = \frac{Z_P(t)\overline{Z_P(s)} + Z_P(t-s)}{M(M+1)}.$$

Subtracting the product of means proves (D.3); setting $s = t$ proves (D.4).

For the fourth moment use (D.9) with the four operators $U, U, U^\dagger, U^\dagger$, where $U = e^{-itH}|_{\operatorname{ran} P}$. Each cycle of a permutation contributes the trace of the product along that cycle. The identity permutation contributes $|z|^4$. The six single transpositions contribute $2\operatorname{Re}(z_2\overline{z}^2) + 4M|z|^2$; the three products of two transpositions contribute $|z_2|^2 + 2M^2$; the eight three-cycles contribute $8|z|^2$; and the six four-cycles contribute $6M$. Their sum proves (D.5).

If $P_{aa} = \langle a|P|a\rangle > 0$, then $v_a = P|a\rangle/\sqrt{P_{aa}}$ is a unit vector in $\operatorname{ran} P$ and $|\langle a|\psi\rangle|^2 = P_{aa}|\langle v_a|\psi\rangle|^2$. For $M > 1$ the last factor has the $\operatorname{Beta}(1, M-1)$ distribution. Its qth moment is $\Gamma(q+1)\Gamma(M)/\Gamma(M+q)$, which follows by integrating the beta density. For $M = 1$ the factor equals one and the same formula holds. Terms with $P_{aa} = 0$ vanish. Summation over a proves (D.7), and $q = 2$ gives (D.8). □

With $K_P(t) = |Z_P(t)|^2/M$, the survival identity reads

$$\mathbb{E}_\psi S_\psi(t) = \frac{K_P(t)+1}{M+1}. \tag{D.10}$$

Thus random initial-state sampling adds a known contribution even for a fixed spectrum. This contribution should be separated before attributing survival fluctuations to disorder. For an ensemble with fixed window rank M, the law of total variance gives the exact decomposition

$$\operatorname{Var}_{H,\psi} A_\psi(t) = \mathbb{E}_H \frac{M^2 - |Z_P(t)|^2}{M^2(M+1)} + \frac{\operatorname{Var}_H Z_P(t)}{M^2}, \tag{D.11}$$

$$\operatorname{Var}_{H,\psi} S_\psi(t) = \mathbb{E}_H \operatorname{Var}_\psi(S_\psi(t) \mid H, P) + \frac{\operatorname{Var}_H(|Z_P(t)|^2)}{M^2(M+1)^2}. \tag{D.12}$$

The first term in each line is caused by state weights at fixed disorder. The second is a spectral fluctuation of the disorder ensemble and may itself be resolved by conditioning on its radial variables. For a random-rank window, the between-disorder terms are instead $\mathrm{Var}_{\mathbb{C}}(Z_P(t)/M)$ and $\mathrm{Var}((|Z_P(t)|^2+M)/(M(M+1)))$, respectively, with $M \geq 1$ almost surely.

Equation (D.8) uses the diagonal of the same projection P as the survival calculation. It therefore accounts for the actual occupation-basis envelope of the energy shell. Counting eigenvalues of H in a window does not by itself count the occupation configurations on which an eigenstate can have support. The reference in (D.8) remains well defined in both situations. It is a conditional null model; no assertion that SYK eigenstates are Haar distributed inside their energy shells is needed for the identity. Since $0 \leq P_{aa} \leq 1$ and $\sum_a P_{aa} = M$, one has $M \leq D_{\mathrm{eff}}(P) \leq \dim \mathcal{H}$. For $P = I$, (D.8) reduces to $2/(\dim \mathcal{H}+1)$. Equation (D.7) concerns the participation moment itself; a mean Rényi entropy requires averaging after taking its logarithm.

D.2 What a state Lanczos chain determines

For a unit state ψ, its spectral measure is

$$d\mu_\psi(E) = \langle\psi|dP_H(E)|\psi\rangle = \sum_j w_j \delta_{E_j}(dE), \qquad w_j = \|P_{E_j}\psi\|^2. \tag{D.13}$$

Only positive weights are included, and the E_j are distinct. The standard spectral-measure correspondence [Gau04] gives a precise statement of the information available to a state Krylov calculation.

Proposition D.2 (Spectral measure and Lanczos equivalence)**.** *If μ_ψ has r atoms, then the cyclic space $\mathcal{K}_\psi = \mathrm{span}\{H^j\psi : j \geq 0\}$ has dimension r. The complete Lanczos matrix, with positive off-diagonal entries, determines μ_ψ uniquely, and conversely μ_ψ determines that matrix. Two state–Hamiltonian pairs have the same complete Lanczos data if and only if their cyclic restrictions are unitarily equivalent by a unitary mapping one initial state to the other.*

If both measures have at least $m+1$ atoms, their leading $(m+1)\times(m+1)$ Lanczos matrices coincide if and only if their moments of orders $0, 1, \ldots, 2m+1$ coincide.

Proof. The map $p \mapsto p(H)\psi$ is an isometry from polynomials with the $L^2(\mu_\psi)$ inner product onto the cyclic space. Polynomial interpolation at the r support points proves that this space has dimension r. Orthogonalizing $1, E, E^2, \ldots$ with positive leading coefficients gives orthonormal polynomials p_n and the Lanczos vectors $p_n(H)\psi$. Multiplication by E has a three-term recurrence, so its matrix is the Lanczos matrix J with positive off-diagonal entries up to its terminal zero. Conversely,

$$\langle e_0, (zI - J)^{-1} e_0\rangle = \int \frac{d\mu_\psi(E)}{z - E}$$

recovers all atoms and weights by its poles and residues. The polynomial isometries also prove the claimed unitary equivalence.

For the finite-depth statement, the Gram matrix of $1, E, \ldots, E^m$ uses moments through order $2m$, and the matrix of multiplication by E in these coordinates uses moments through order $2m+1$. Their orthonormalization therefore determines the leading Lanczos matrix from those moments. Conversely, a closed walk starting at index zero in a tridiagonal matrix cannot visit index $m+1$ and return in fewer than $2m+2$ steps. Hence $\langle\psi, H^k\psi\rangle = (J_m^k)_{00}$ for $0 \leq k \leq 2m+1$, where J_m is the leading $(m+1)\times(m+1)$ block. This proves the converse. □

For a windowed equal-weight state, or the corresponding thermofield double with the Hamiltonian acting on one factor, $w_j = 1/M$ within a nondegenerate window. For a projected occupation state $P|a\rangle/\|P|a\rangle\|$ and a distinct energy E in the window, the corresponding weight is

$$w_E^{(a,P)} = \frac{\langle a|P_E|a\rangle}{\langle a|P|a\rangle}, \qquad P_E \le P, \qquad \langle a|P|a\rangle > 0. \tag{D.14}$$

Here P_E is the full spectral projection at E. At a simple eigenvalue the numerator is $|\langle E|a\rangle|^2$.

Comparing these two prescriptions at the same spectrum separates a change in spectral correlations from a change in the local spectral weights. A Lanczos roughness statistic cannot in general distinguish pairs with the same spectral measure, and it does not recover the operator-size information associated with a chosen tensor-product structure.

E Finite-depth stability under changes of spectral weights

The correspondence in Proposition D.2 also gives a quantitative sufficient condition for stable finite-depth Lanczos data. A common affine rescaling places the two spectral supports in $[-1, 1]$. The bound concerns this fixed energy coordinate, rather than separately chosen rescalings of the two measures.

Proposition E.1 (A Hankel bound for finite-depth Lanczos data)**.** *Let μ, ν be probability measures supported in $[-1, 1]$, and fix $m \ge 0$. Write*

$$g_j(\mu) = \int x^j \, d\mu(x), \quad G_m(\mu) = (g_{i+j}(\mu))_{i,j=0}^m, \quad T_m(\mu) = (g_{i+j+1}(\mu))_{i,j=0}^m.$$

Suppose $\lambda_{\min}(G_m(\mu)) \ge \gamma > 0$, and set

$$\delta = \max_{0 \le j \le 2m+1} |g_j(\mu) - g_j(\nu)|.$$

If $(m+1)\delta \le \gamma/2$, both leading Lanczos matrices $J_m(\mu)$ and $J_m(\nu)$ are defined and

$$\|J_m(\mu) - J_m(\nu)\|_2 \le \frac{6(m+1)}{\gamma}\,\delta. \tag{E.1}$$

In particular, this bound holds separately for the difference of each diagonal coefficient and each included off-diagonal coefficient. If the two Hankel matrices both have smallest eigenvalue at least γ, the factor 6 may be replaced by 3, without the smallness assumption.

Proof. Put $d = m+1$, let $\mu_s = (1-s)\mu + s\nu$, and abbreviate $G(s) = G_m(\mu_s)$ and $T(s) = T_m(\mu_s)$. Since each of the d^2 matrix entries changes by at most δ,

$$\|G'(s)\|_F \le d\delta, \qquad \|T'(s)\|_2 \le \|T'(s)\|_F \le d\delta.$$

Weyl's inequality and the hypothesis give $G(s) \succeq (\gamma/2)I$ on $[0, 1]$. Let $G(s) = R(s)^{\mathsf{T}} R(s)$ be its upper-triangular Cholesky factorization with positive diagonal, and put $C(s) = R(s)^{-1}$. The columns of $C(s)$ are the coefficient vectors of the orthonormal polynomials with positive leading coefficients. Consequently,

$$J(s) = C(s)^{\mathsf{T}} T(s) C(s) = J_m(\mu_s).$$

Multiplication by x on $L^2(\mu_s)$ is a self-adjoint contraction, so its compression $J(s)$ satisfies $\|J(s)\|_2 \le 1$.

Define $L = R'R^{-1}$. Differentiating the Cholesky identity gives

$$X := C^{\mathsf{T}} G' C = L^{\mathsf{T}} + L.$$

Because L is upper triangular, its strict upper entries are those of X and its diagonal entries are one half of the diagonal entries of X. Thus $\|L\|_2 \le \|L\|_F \le \|X\|_F$. Since $\|C\|_2^2 = \lambda_{\min}(G)^{-1} \le 2/\gamma$,

$$\|L\|_2 \le \frac{2d\delta}{\gamma}.$$

Using $C' = -CL$ now yields

$$J' = -L^{\mathsf{T}} J - JL + C^{\mathsf{T}} T' C, \qquad \|J'\|_2 \le \frac{6d\delta}{\gamma}.$$

Integration over $s \in [0,1]$ proves (E.1). If both endpoint Hankel matrices are bounded below by γI, their convex combinations have the same lower bound, and the preceding estimates improve by a factor of two. □

For measures on a fixed set of points in $[-1,1]$ with probability weights w_j and $\widetilde{w}_j$, one may take $\delta \le \sum_j |w_j - \widetilde{w}_j|$. More generally, the mean-value theorem gives $\delta \le (2m+1) W_1(\mu,\nu)$, where W_1 is the Wasserstein distance for cost $|x-y|$. The estimate is a sufficient condition and can be conservative because monomial Hankel matrices become poorly conditioned at large depth. No assertion of uniform stability as m approaches the cyclic dimension follows from it. A statistic involving $\log b_n$ additionally requires the relevant b_n to be bounded away from zero, so exclusion of the terminal part of a Krylov chain has a separate mathematical justification.

F Baseline paired radius calculations

F.1 Sampling design and estimators

We diagonalize the even-parity block at the three sizes in Table 8. For each independent pair of Gaussian coupling vectors, the same directions are used at $\kappa = 0, 1, 4, 16, 64, \infty$, and for both the Gaussian Hamiltonian H_κ and its fixed-radius counterpart H_κ°. There are 7,168 independent paired disorder draws and 86,016 block spectra in total. Samples at different values of κ, and the two ensembles within a draw, are correlated by design. Uncertainty calculations preserve these pairings.

N	Block dimension D	Paired samples	d_2	d_4
10	16	2,048	45	210
14	64	4,096	91	1,001
18	256	1,024	153	3,060

Table 8: Main exact-diagonalization ensembles. Each paired sample contains six deformation values in each of the two coupling ensembles.

The spacing ratio uses the central half of each block by rank. The principal spectral trace instead uses the fixed physical-energy filter

$$f(E) = \exp[-E^2/(2\sigma_f^2)], \qquad \sigma_f = 0.5,$$

in the ensemble-normalized energy units of Section 2. We retain 161 time points: zero and a geometric grid from 0.02 to $1.6\sqrt{2\pi}D$. This endpoint defines a common plotting range in the ensemble-normalized energy units. Neither unfolding nor sample-width division enters these filtered traces. Separately, unfiltered normalized traces are saved at $t = 0.02, 0.04, 0.08, 0.16, 0.32$ to test Theorem A.2.

All spectral cumulants in this appendix use global disorder centering, so their population target is Q_Y, not the conditionally centered Q_R. The covariance, pseudocovariance, and fourth cumulant use Theorem B.2. The normalized summary is $q_4(t) = Q_Y(t,t)/C_Y(t,t)^2$. Its sample ratio, and the sample ratio defining K_f^c, retain ratio bias. Confidence intervals are pointwise 95% percentile intervals from 400 bootstrap resamples of complete disorder draws, using the same resampling weights across each paired scan. The intervals quantify sampling uncertainty at a specified time and do not give simultaneous coverage of an entire curve. Fourth-order quantities are consequently interpreted together with their covariance scale and uncertainty, rather than by the sign of a noisy normalized point alone.

F.2 The radial contribution at short times

Figure 13 tests the change in the leading power of time. In the Gaussian ensemble, $C_z(t)/t^4$ approaches the nonzero value $\mathrm{Var}(s_\kappa^2)/4$. For fixed radii the same ratio approaches zero. Table 9 gives a representative numerical comparison at $N = 14, t = 0.02$. Each exact Gaussian limit lies within its pointwise interval. The much smaller fixed-radius values show directly the removal of the leading radial term. At the quadratic endpoint the cubic trace also vanishes for these sizes, allowing a higher-order onset than the general $O(t^6)$ bound. We do not fit a power law from these five points.

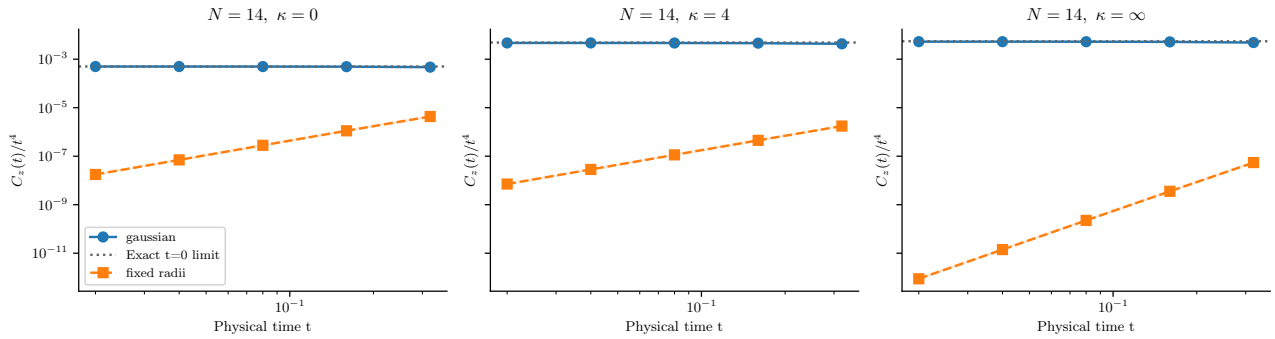


Figure 13: Unfiltered short-time covariance for the paired $N = 14$ ensembles. The plotted quantity is $C_z(t)/t^4$, with $z = D^{-1}\,\mathrm{Tr}_D\, e^{-itH}$. Horizontal reference values are the exact Gaussian limits in (A.6); shaded bands are pointwise 95% paired-bootstrap intervals. The fixed-radius curves tend to zero. This test concerns the early-time Taylor expansion.

Independent Monte Carlo samples of 200,000 radius pairs at each size also verify the exact variance formulas. For example, at $N = 14$, $\mathrm{Var}(\log R_2 - \log R_4) = 0.00605533$ from (3.9), compared with 0.00608381 in this independent sample. Figure 17 in Appendix G shows these

κ	Gaussian estimate [95% interval]	Exact limit	Fixed-radius estimate
0	$4.9826\,[4.7641, 5.1640] \times 10^{-4}$	4.9950×10^{-4}	1.7635×10^{-8}
4	$4.6810\,[4.4832, 4.9068] \times 10^{-3}$	4.8688×10^{-3}	7.1116×10^{-9}
∞	$5.2829\,[5.0589, 5.5399] \times 10^{-3}$	5.4945×10^{-3}	8.8262×10^{-13}

Table 9: Values of $C_z(t)/t^4$ at $N = 14, t = 0.02$, compared with the exact Gaussian $t \to 0$ coefficient. The power of ten in the second column applies to both the point estimate and the interval.

radial comparisons. This test uses only the coupling distribution and requires no matrix diagonalization.

F.3 Filtered spectral variance and fourth cumulants

The fixed physical-energy window retains smooth spectral fluctuations at $t = 0$, where $Z_f(0) = \mathrm{Tr}_D\, f(H)$ is random. Their contribution is substantial. At $N = 14, \kappa = 4$, we obtain

$$\begin{aligned} \widehat{K}^c_{f,\mathrm{G}}(0) &= 0.122817 \quad [0.116969, 0.128013], \\ \widehat{K}^c_{f,\circ}(0) &= 0.003504 \quad [0.003315, 0.003718]. \end{aligned} \tag{F.1}$$

Thus changing the radius ensemble can strongly change a connected quantity even when no local level correlations have been estimated. The unfiltered identity at $t = 0$ would instead give zero variance.

Figure 14 compares the complete filtered curves and their normalized fourth cumulants at $N = 14$. Fixing the two radii does not uniformly reduce q_4: in early-time portions of the $\kappa = 4$ and quadratic-endpoint curves, its fixed-radius value is larger. The second-order scale is strongly reduced, and the remaining trace distribution is different. Consequently the numerical comparison at equal nominal κ cannot be identified with subtraction of a single nonnegative term in (4.9). The effective coupling enters the conditional cumulants. The additional terms due to the random conditional mean enter the global cumulant through (B.3). Section 6 evaluates these conditional terms with a separate independent nested sample. The calculations in this appendix supply the baseline comparison and the spectra used to check Theorem 5.1.

F.4 Local spectral comparison and endpoint calibration

The central spacing ratios provide a complementary comparison (Fig. 15). At $N = 14$, their Gaussian means at $\kappa = 0, 1, 4, 16, 64, \infty$ are respectively

$$0.59940, \quad 0.59964, \quad 0.59333, \quad 0.47041, \quad 0.40648, \quad 0.39278.$$

Across the measured intermediate points and all three sizes, the largest absolute difference between the two ensemble means is below 7×10^{-4}. This is a statement about this finite-size scan; the convolution law does not impose such a small bound on an arbitrary response curve.

At either pure endpoint, the two spectra differ only by a positive scalar, so their spacing ratios coincide samplewise. The observed agreement therefore checks scale invariance. The quadratic endpoint itself has appreciable finite-size dependence:

$$\begin{aligned} N = 10: &\quad \langle r \rangle_\infty = 0.45272 \quad [0.44614, 0.45814], \\ N = 18: &\quad \langle r \rangle_\infty = 0.38437 \quad [0.38068, 0.38824]. \end{aligned} \tag{F.2}$$

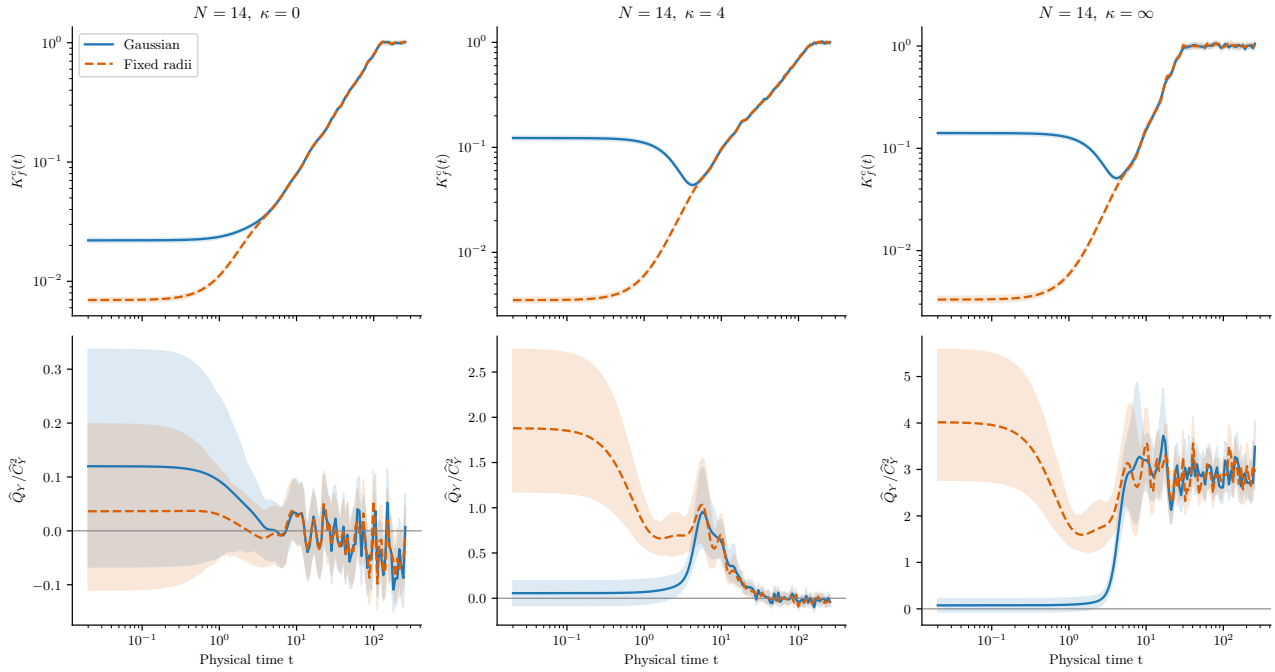


Figure 14: Gaussian and fixed-radius ensembles at $N = 14$, with the fixed physical filter $\sigma_f = 0.5$. The upper row gives connected form factors normalized by $\mathbb{E}\,\mathrm{Tr}_D\, f(H)^2$; the lower row gives $q_4 = Q_Y/C_Y^2$, including the pseudocovariance subtraction in Q_Y. Shaded bands are pointwise 95% paired-bootstrap intervals. The samples are globally centered. Fixing radii changes both the second-order scale and the normalized fourth cumulant.

In particular, a Poisson reference cannot replace the actual $N = 10$ quadratic ensemble. The combination of strong early-time covariance changes and small spacing-ratio changes illustrates the distinct dependence of these observables on the coupling ensemble. It supplies no thermodynamic phase boundary.

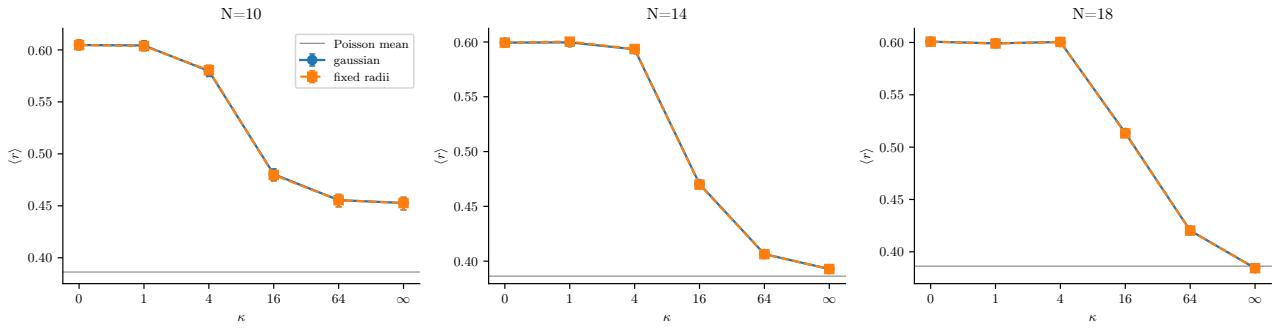


Figure 15: Central-half spacing ratios for the paired ensembles at $N = 10, 14, 18$, with pointwise 95% bootstrap intervals. The Gaussian and fixed-radius endpoint values agree samplewise. The horizontal line is the Poisson reference. Horizontal positions enumerate the sampled couplings; the finite-size quadratic endpoint is computed directly from the quadratic ensemble.

F.5 A conditional Gaussian control

To test the statistical mechanism separately from the SYK dynamics, let G be a proper complex Gaussian with $\mathbb{E}|G|^2 = 1$, independent of the two radii, and set

$$\xi = \sqrt{C_R}\, G, \qquad C_R = w_4 R_4^2 + w_2 R_2^2. \tag{F.3}$$

Every conditional fourth cumulant is zero, while

$$\frac{Q_\xi}{(\mathbb{E}|\xi|^2)^2} = 2\,\mathrm{Var}(C_R) = 4\left(\frac{w_4^2}{d_4} + \frac{w_2^2}{d_2}\right) > 0. \tag{F.4}$$

The whitened variable $\xi/\sqrt{C_R} = G$ has zero fourth cumulant. This is a direct instance of Theorem 4.1.

We simulate 2,000,000 such samples using $d_2 = 45, d_4 = 210$. At $\kappa = 4$, the exact normalized excess is 0.0788049 and the estimate is 0.0782879, with block standard error 0.0015199. The whitened estimate is -0.0007701, with block standard error 0.0012620. The errors use 100 independent blocks of 20,000 samples. Figure 16 records the full comparison. This control validates the variance-mixture mechanism and the estimator; it does not assume that the conditional SYK trace is Gaussian.

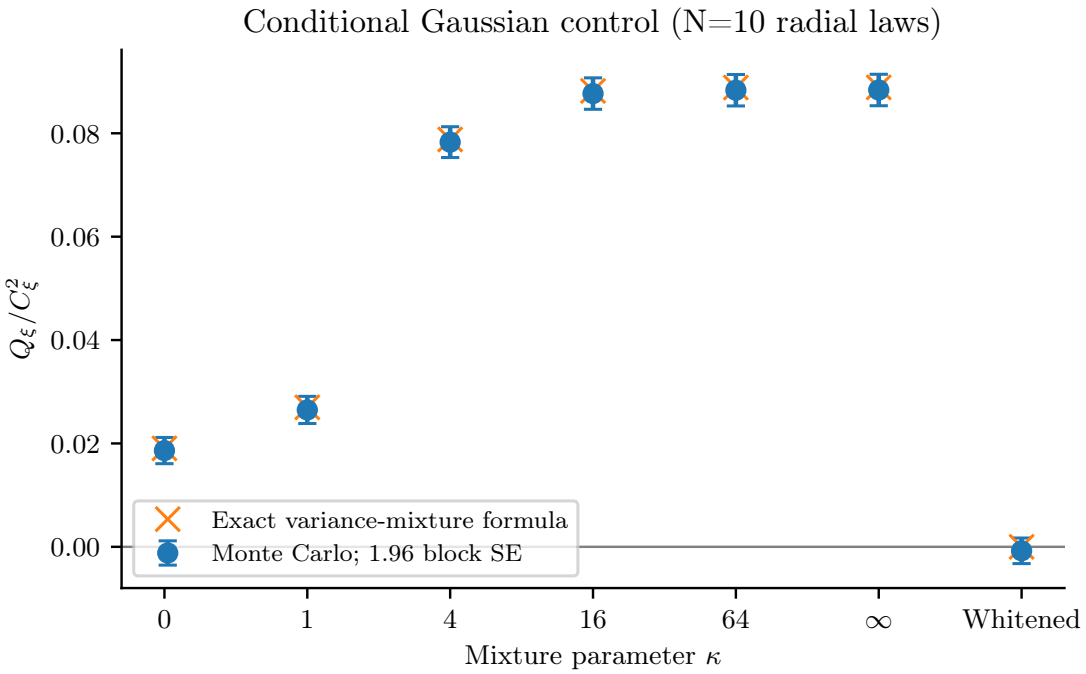


Figure 16: Independent synthetic control with conditionally proper complex Gaussian amplitudes. The unconditional fourth excess follows (F.4); dividing each amplitude by its known conditional standard deviation gives the proper Gaussian reference. The samples here are generated from (F.3) and are separate from the SYK samples. Error bars are 95% normal intervals based on the block standard errors.

The supplied programs generate the paired spectra, filtered traces and resampling weights. Appendix G gives the algebraic checks and synthetic controls.

G Independent numerical checks

The computational material separates deterministic identities, ensemble estimation, and synthetic controls. The deterministic implementation checks include the Majorana anticommutator, Hermiticity, parity, and the antiunitary action at $N = 8, 10, 12, 14$. The $N = 8$ calculation checks symmetry only; the radial theorems and the main numerical ensembles use $N > 8$.

For the explicit matrix tests, the Frobenius-norm discrepancy in $H_\kappa = s_\kappa H^\circ_{u_\kappa}$ is at most 1.81×10^{-15}. The occupation-state variance identity for b_1^2 agrees to absolute error 7.22×10^{-16}. Every saved main spectrum has the predicted normalized squared width within 4.00×10^{-15}. The quadratic full-space spectrum is also checked against the subset sums of its single-particle energies at $N = 14$, with maximum absolute discrepancy 8.44×10^{-15}.

The projector-Haar participation formula is tested with 50,000 state draws for an explicit rank-16 projection in dimension 64. Its predicted mean IPR is 0.09044548; the empirical mean is 0.09043030 with standard error 0.00009563. Proper and improper complex Gaussians and a uniform phase on the unit circle test the fourth cumulant estimator with known population values. Simulations of the count laws Poisson(L) and $1 + \text{Poisson}(L)$ check the mean squared deviations L and $L + 1$ in Section B.3.

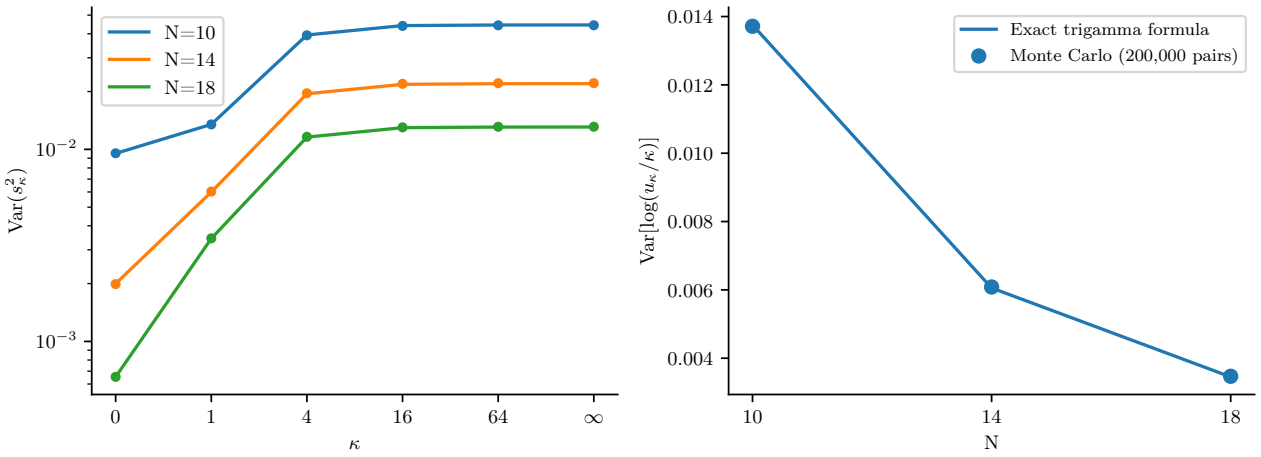


Figure 17: Independent checks of the coupling-radius laws. Monte Carlo points use 200,000 independent radius pairs at each size; curves or reference values follow the exact width variance and trigamma formulas. These draws are independent of the main diagonalization sample.

These checks test algebra, normalization, and sampling formulas. They do not constitute numerical tests of the complete charge-memory curve or of all terms in the nested fourth-cumulant decomposition. Machine-readable configuration and validation files record the random streams, sample sizes, tolerances, and software versions. The original ensemble calculations used Python 3.12.14, NumPy 2.3.5, SciPy 1.17.0, and single-threaded BLAS. The supplement gives the environment and commands for regeneration.

H Coarse-grid crossover and finite-size drift

This appendix compares the original coarse grid with the refined estimates of Section 8 and quantifies the sensitivity to interpolation.

H.1 Paired computation and operational crossings

We compute independent disorder samples at $N = 10, 14, 18, 22$, with even-parity block dimensions $16, 64, 256, 1024$ and sample counts $2048, 2048, 512, 128$, respectively. These sizes have the same unitary symmetry class for the quartic single-parity block. The deformation grid is $\kappa \in \{0, 2, 4, 8, 12, 16, 24, 32, 48, 64, 96, 128, \infty\}$. Every sample uses the same two angular coupling directions and the same Gaussian radii for both ensembles and the entire grid. We compute the adjacent-gap ratio from the central 50% of levels by rank, retaining only triples entirely inside that window. The program records the spectra, radii and resampling counts. This scan uses disorder samples independent of the baseline experiment in Appendix F.

Let $\bar{r}^{\circ}_N(\kappa)$ denote the directional-ensemble mean spacing ratio and define

$$p_N(\kappa) = \frac{\bar{r}^{\circ}_N(0) - \bar{r}^{\circ}_N(\kappa)}{\bar{r}^{\circ}_N(0) - \bar{r}^{\circ}_N(\infty)}. \tag{H.1}$$

Both endpoints are measured at each finite N; in particular, the quadratic endpoint is not replaced by the Poisson number. Positive rescaling leaves the spacing ratio invariant, so the two ensembles have identical paired endpoint ratios. The endpoint means and normalizing denominator are re-estimated in each bootstrap replicate. We use 1000 resamples of complete paired samples. The reported 95% intervals are pointwise percentile intervals. Because the endpoints vary with N, a relative threshold does not correspond to the same absolute mean ratio at every size. We therefore also release the crossing of the common raw threshold $\langle r \rangle = 0.5$ as a normalization sensitivity check; it is not used to replace the prespecified response crossings.

An operational monotone curve is constructed by clipping the response to $[0, 1]$ and applying equal-weight isotonic regression to the interior grid, with endpoints fixed at zero and one. Crossings at response levels $q = 0.25, 0.5, 0.75$ are obtained by linear interpolation in $\log \kappa$ between finite positive grid points, with no extrapolation. This is a stated numerical definition; it is not a proof of monotonicity. The largest adjustment to a reported mean response was 0.0273. The minimum fraction of bootstrap replicates with a bracketed crossing was 1.0000. Raw unprojected means are also released. The operational logarithmic width is

$$W_N = \log \frac{\kappa_{0.75,N}}{\kappa_{0.25,N}}. \tag{H.2}$$

The directional logarithmic widths are 0.951, 1.166, 1.338, 1.335 for $N = 10, 14, 18, 22$, respectively. They increase from the first to the third size. The final change is -0.0033 with interval $[-0.1365, 0.1250]$, so subsequent sharpening is not resolved. All crossing intervals are conditional on the stated interpolation rule; a separate released table compares PCHIP and coarsened-grid crossings. For example, at $N = 10$, the operational width is 0.95081 with sampling interval $[0.908, 0.998]$, whereas PCHIP gives 0.88355 and the coarsened grid gives 1.23901. This sensitivity is separate from the quoted sampling interval.

For a compact description of the drift, we regress the four measured $\log \kappa_{0.5,N}$ against $\log N$ and repeat the regression on the smallest and largest three sizes. This regression is a finite-range summary; neither a power-law ansatz for the asymptotic crossover nor a critical exponent follows from four sizes. The released table additionally gives adjacent-size local slopes. Variation with size selection and response threshold is part of the uncertainty in any proposed extrapolation. The directional slope changes from 1.611 using all four sizes to 2.028 using the largest three. The common raw-ratio threshold 0.5 gives crossings $11.31, 11.49, 18.92, 27.64$ at $N = 10, 14, 18, 22$, respectively. For the first two sizes, these compare with response-median crossings 8.52 and

N	$\kappa_{0.25}$	$\kappa_{0.5}$	$\kappa_{0.75}$	W_N
10	5.49 [5.14, 5.87]	8.52 [8.05, 9.01]	14.20 [13.50, 14.93]	0.951 [0.908, 0.998]
14	7.05 [6.82, 7.29]	11.86 [11.58, 12.15]	22.63 [22.02, 23.23]	1.166 [1.136, 1.196]
18	11.90 [11.54, 12.30]	20.68 [19.90, 21.53]	45.37 [42.75, 48.05]	1.338 [1.285, 1.391]
22	17.64 [17.10, 18.19]	29.54 [28.11, 31.11]	67.01 [58.37, 76.74]	1.335 [1.206, 1.453]

Table 10: Fixed-radius directional crossings and logarithmic widths. Brackets give pointwise 95% paired-bootstrap intervals, including uncertainty in the measured finite-size endpoints. These are definitions of finite-size response crossings, not transition points.

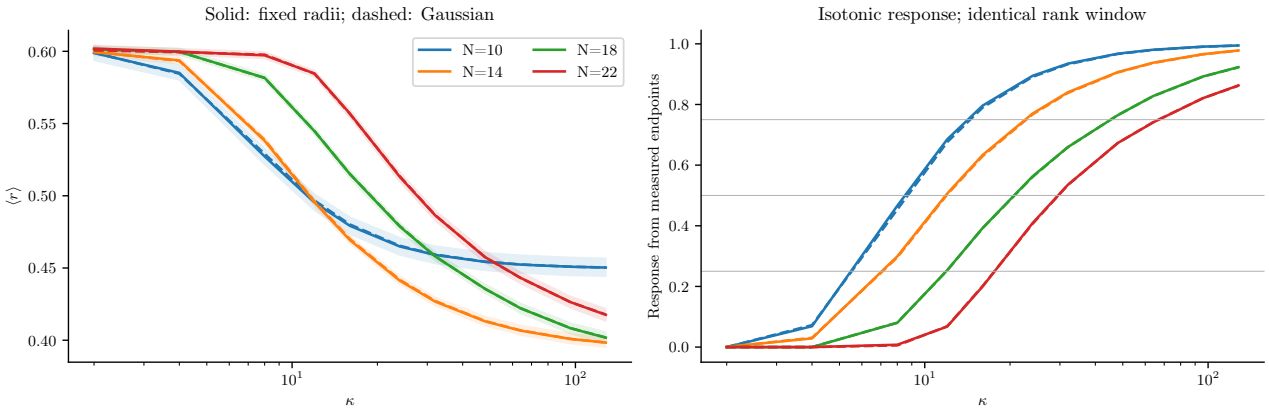


Figure 18: Original paired spacing curves. Solid curves use fixed radii and dashed curves use Gaussian radii. Left: raw mean ratios, with pointwise intervals for the directional ensemble. Right: response normalized by measured finite-size endpoints and projected monotonically using the stated procedure.

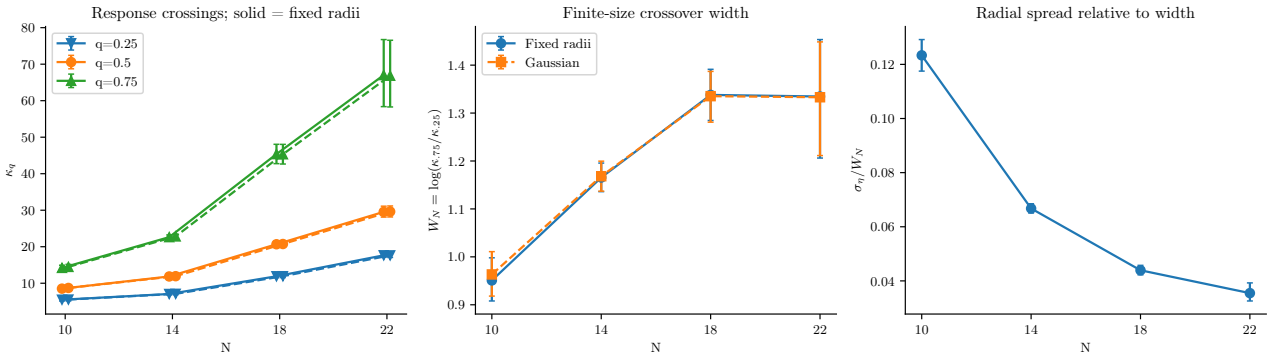


Figure 19: Finite-size drift of the three operational crossings, their logarithmic width, and the ratio of radial log-coupling spread to the directional width. Both ensembles use the same physical rank window and paired disorder.

11.86. Endpoint normalization therefore matters to the smallest-size drift. Detailed drift and interpolation-resolution tables appear in Appendix I.

H.2 Radial spread relative to the directional width

Theorem 3.2 applies directly to this spacing statistic: the Gaussian curve is the directional curve convolved in $x = \log \kappa$. The endpoint means agree, so the same relation holds for the exactly normalized response. The radial variable obeys $e^{2\eta} \sim F(d_2, d_4)$, with mean m_η and variance v_η given by Eqs. (3.8)–(3.9). Set $\sigma_\eta = \sqrt{v_\eta} = O(N^{-1})$; meanwhile $m_\eta = O(N^{-2})$.

Width and crossing control. Write $P_N(x) = p_N(e^x) = F_N((x - \xi_N)/W_N)$ and suppose that $\|F_N'\|_\infty \le L_1$ and $\|F_N''\|_\infty \le L_2$, with constants L_1, L_2 uniform in N for any large-N conclusion. The curvature bound (3.10) and a mean-value estimate for the shift by m_η imply

$$\|\mathbb{E}_\eta P_N(\,\cdot + \eta) - P_N\|_\infty \le \frac{L_1 |m_\eta|}{W_N} + \frac{L_2 v_\eta}{2W_N^2}. \tag{H.3}$$

Consequently σ_η / W_N controls centered radial smoothing under the stated derivative assumptions. A width of order one makes this effect small at large N; a width of order N^{-1} can retain order-one smoothing. The finite numerical grid does not verify uniform derivative bounds, and the four available sizes do not determine the asymptotic width law. In the present data the relative radial spread decreases from 0.123 at $N = 10$ to 0.0355 at $N = 22$, while the directional width remains of order one.

If $P_N'(x) \ge m > 0$ on an interval containing both q-crossings and the uniform convolution error there is at most ϵ, the mean-value theorem also gives

$$|\log \kappa_{q,G} - \log \kappa_{q,\circ}| \le \epsilon / m. \tag{H.4}$$

These sufficient conditions connect a controlled smoothing error to crossing drift without assigning a transition or critical exponent to either curve.

We integrate the exact radial-ratio law independently of the angular data using 32768 midpoint quantiles of $F(d_2, d_4)$, and compare against 8192 quantiles. The maximum resulting change in a predicted ratio is 7.74×10^{-8}. Interpolation of the directional curve in log coupling is an additional approximation. We compare linear interpolation, shape-preserving cubic interpolation (PCHIP), and a coarsened grid, restricting quantitative comparison to $4 \le \kappa \le 96$ to reduce sensitivity to the auxiliary endpoint extensions. The radial shift has unbounded support, so this restriction does not remove tail dependence on those extensions; for example, at $N = 10$, $\kappa = 96$, $\Pr(96e^\eta > 128) = 0.00378$. The interpolation-method spread is a sensitivity diagnostic, not a proven discretization bound. In particular, interpolating a single realization across this grid need not resolve its fine spectral motion; the shifts therefore serve only as an interpolation diagnostic.

Of the 36 interior pointwise intervals for the direct estimate minus the linear-convolution prediction, 16 contain zero. The linear interpolant therefore does not resolve the small convolution correction quantitatively on this grid. In particular, its knots introduce slope discontinuities, which can create an artificial contribution of order σ_η where a smooth curve has a centered correction of order σ_η^2. The substantial linear–PCHIP and grid-coarsening sensitivities identify insufficient directional interpolation resolution. The count of intervals is descriptive. Direct sampling in Section 8 eliminates the interpolation step at ten size–coupling pairs.

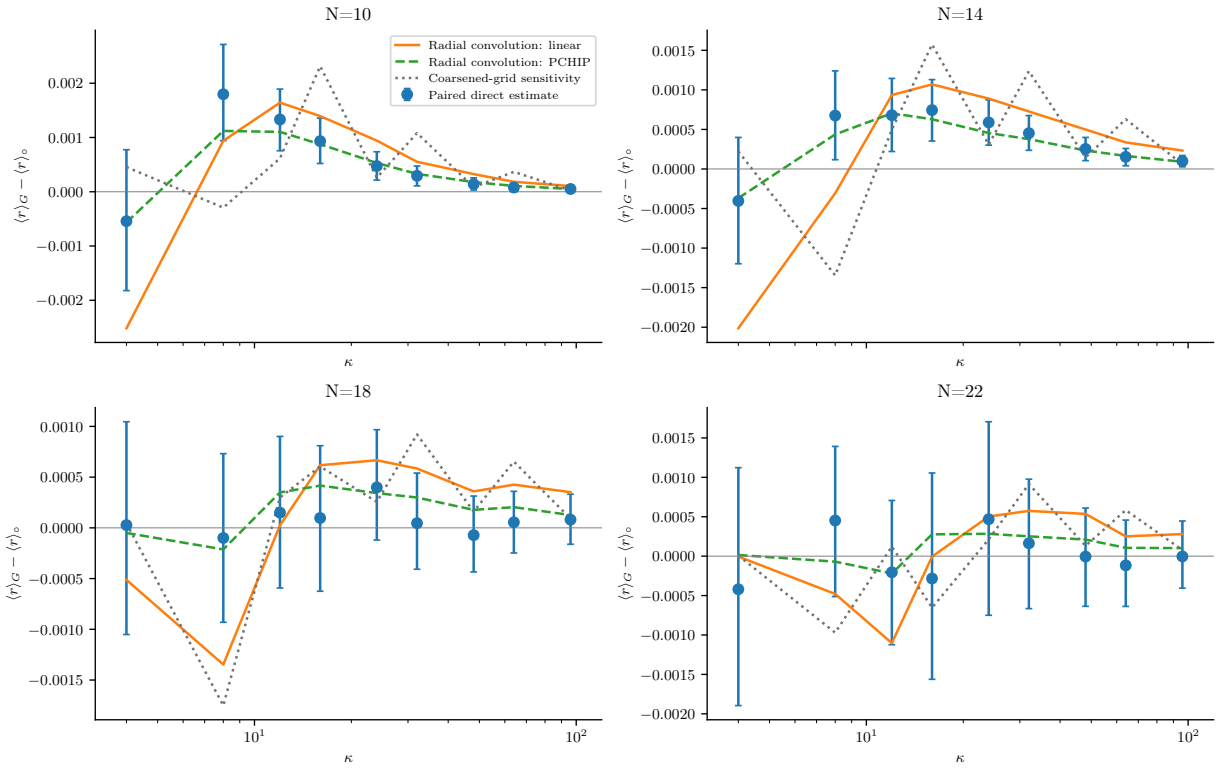


Figure 20: Direct paired changes in the spacing statistic compared with the independently integrated radial convolution and interpolation sensitivities. Error bars are pointwise 95% bootstrap intervals.

I Directional drift and interpolation resolution

These tables document size-selection and interpolation sensitivity for the calculations in Section H. The bootstrap intervals quantify disorder sampling under the declared extraction rule. Neither the fit-range variation nor the interpolation-method spread is included as a probabilistic error bar.

The small quadrature refinement difference controls only the integration of the chosen interpolant. It does not measure the overall error of the radial-convolution prediction. At a piecewise-linear knot, unequal one-sided slopes generate a local term proportional to $\mathbb{E}|\eta| = O(\sigma_\eta)$; a smooth mean curve instead has centered smoothing of order σ_η^2 under the stated curvature assumption. Refining radial quadrature cannot remove this angular-interpolation artifact. The nonzero Gaussian-ratio tails also retain some dependence on endpoint extensions.

For example, at $N = 10$, the operational width is 0.95081 with sampling interval $[0.908, 0.998]$, whereas PCHIP gives 0.88355 and the coarsened grid gives 1.23901. This sensitivity is separate from the quoted sampling interval.

J Nonresonant expansion of the elastic weight

The occupation identity in (10.8) admits a direct perturbative interpretation for a fixed quadratic spectrum. Let $B^\circ|n\rangle = b_n|n\rangle$ in the chosen parity block and write $q_a(n) = \langle n|Q_a|n\rangle \in \{-1, 1\}$. The overall normalization of H_κ° does not affect its eigenvectors.

Sizes	Descriptive log–log slope	Pointwise 95% interval
10,14,18,22	1.611	[1.518, 1.696]
10,14,18	1.479	[1.352, 1.598]
14,18,22	2.028	[1.905, 2.149]

Table 11: Sensitivity of the directional median-crossing drift summary to the size range. These slopes are not identified with critical exponents.

N	σ_η	σ_η/W_N	$\max\lvert\Delta_{\mathrm{pred}}\rvert$	Linear–PCHIP	Median CI half-width
10	0.1173	0.1233	2.52e-03	1.95e-03	2.61e-04
14	0.0778	0.0668	2.01e-03	1.64e-03	2.86e-04
18	0.0588	0.0439	1.35e-03	1.13e-03	5.44e-04
22	0.0474	0.0355	1.10e-03	8.84e-04	9.15e-04

Table 12: Radial convolution compared with its finite-grid and sampling resolution. Maxima and median interval widths use the interior grid. The last column concerns the directly sampled Gaussian-minus-directional mean ratio.

Proposition J.1 (Fixed-sample elastic deficit)**.** *Suppose B° has simple spectrum in the block, and fix A°. As $\kappa \to \infty$,*

$$1 - p_\infty = \frac{1}{mD\kappa^2} \sum_{n \neq l} \frac{|A^\circ_{ln}|^2}{(b_n - b_l)^2} \sum_{a=1}^{m} [q_a(n) - q_a(l)]^2 + O(\kappa^{-3}). \tag{J.1}$$

The sum uses ordered pairs. The coefficient of each matrix element is four times the occupation Hamming distance. The remainder is a fixed-sample statement and may depend on the smallest gap of B°.

Proof. Put $\epsilon = 1/\kappa$ and apply the nondegenerate eigenvector expansion to $B^\circ + \epsilon A^\circ$. Since every Q_a is diagonal in this basis, its expectation in the eigenvector continued from $|n\rangle$ is

$$\langle Q_a \rangle_n = q_a(n) + \epsilon^2 \sum_{l \neq n} \frac{|A^\circ_{ln}|^2 [q_a(l) - q_a(n)]}{(b_n - b_l)^2} + O(\epsilon^3).$$

The first-order off-diagonal eigenvector correction contributes only at second order to this expectation. Normalization supplies the term proportional to $-q_a(n)$. Using $2q_a(n)[q_a(l) - q_a(n)] = -[q_a(l) - q_a(n)]^2$, then summing $1 - \langle Q_a \rangle_n^2$ over n, a, proves (J.1). Finite-dimensional analytic perturbation applies in a neighborhood of zero because all unperturbed eigenvalues are separated. □

This expansion weights occupation-changing quartic matrix elements by the inverse square of their quadratic detuning. A small quadratic gap can therefore make a fixed-sample coefficient large. Averaging (J.1) over a random quadratic spectrum requires separate control of these denominators and of resonant samples. The proposition does not justify an inverse-square law for the disorder-averaged elastic deficit.

For a separate $N = 10$ example, order the quadratic mode magnitudes increasingly and assign the sign of the Pfaffian to the first mode, with the other four positive. We use the independent quartic draw in this frame. The smallest quadratic block gap is 0.0199263 and the coefficient of κ^{-2} in (J.1) is 36.8538. Direct spectral dephasing gives

κ	366.863	733.726	1467.453	2934.906
$\kappa^2(1-p_\infty)$	34.5062	35.6280	36.2271	36.5369

Here $\|A^\circ\|/(\kappa \min_{n\neq l}|b_n - b_l|)$ decreases from 1/4 to 1/32. The supplement records the five signed frequencies used here. The code regenerates the quartic draw with seed 2026111879 and sample index 190001.

References

[Ata+13] Y. Y. Atas, E. Bogomolny, O. Giraud, and G. Roux. "Distribution of the ratio of consecutive level spacings in random matrix ensembles". In: *Phys. Rev. Lett.* 110, 084101 (2013). DOI: 10.1103/PhysRevLett.110.084101. arXiv: 1212.5611.

[Bag+25] M. Baggioli, K.-B. Huh, H.-S. Jeong, K.-Y. Kim, and J. F. Pedraza. "Krylov complexity as an order parameter for quantum chaotic–integrable transitions". In: *Phys. Rev. Research* 7, 023028 (2025). DOI: 10.1103/PhysRevResearch.7.023028. arXiv: 2407.17054.

[BMW25] V. Balasubramanian, J. M. Magan, and Q. Wu. "Quantum chaos, integrability, and late times in the Krylov basis". In: *Phys. Rev. E* 111, 014218 (2025). DOI: 10.1103/PhysRevE.111.014218. arXiv: 2312.03848.

[Ber+21] M. Berkooz, N. Brukner, V. Narovlansky, and A. Raz. "Multi-trace correlators in the SYK model and non-geometric wormholes". In: *JHEP* 09, 196 (2021). DOI: 10.1007/JHEP09(2021)196. arXiv: 2104.03336.

[Bri69] D. R. Brillinger. "The calculation of cumulants via conditioning". In: *Ann. Inst. Statist. Math.* 21 (1969), pp. 215–218. DOI: 10.1007/BF02532246.

[Cha+25] S. Chapman, S. Demulder, D. A. Galante, S. U. Sheorey, and O. Shoval. "Krylov complexity and chaos in deformed Sachdev–Ye–Kitaev models". In: *Phys. Rev. B* 111, 035141 (2025). DOI: 10.1103/PhysRevB.111.035141. arXiv: 2407.09604.

[Che+25] L. Chen, B. Mu, H. Wang, and P. Zhang. "Dissecting quantum many-body chaos in the Krylov space". In: *Phys. Rev. Lett.* 134, 190403 (2025). DOI: 10.1103/PhysRevLett.134.190403. arXiv: 2404.08207.

[CŚ06] B. Collins and P. Śniady. "Integration with respect to the Haar measure on unitary, orthogonal and symplectic group". In: *Commun. Math. Phys.* 264 (2006), pp. 773–795. DOI: 10.1007/s00220-006-1554-3. arXiv: math-ph/0402073.

[DB23] J. Dieplinger and S. Bera. "Finite-size prethermalization at the chaos-to-integrable crossover". In: *Phys. Rev. B* 107, 224207 (2023). DOI: 10.1103/PhysRevB.107.224207. arXiv: 2303.16019.

[Erd+26] J. Erdmenger, K.-B. Huh, H.-S. Jeong, and J. F. Pedraza. "Unfolded Krylov complexity: Universal chaotic dynamics without false positives". In: *Phys. Rev. D* 114, 086021 (2026). DOI: 10.1103/tgwh-w5kp. arXiv: 2609.02228.

[Gar+18] A. M. García-García, B. Loureiro, A. Romero-Bermúdez, and M. Tezuka. "Chaotic–integrable transition in the Sachdev–Ye–Kitaev model". In: *Phys. Rev. Lett.* 120, 241603 (2018). DOI: 10.1103/PhysRevLett.120.241603. arXiv: 1707.02197.

[Gau04] W. Gautschi. *Orthogonal Polynomials: Computation and Approximation*. Oxford: Oxford University Press, 2004. DOI: 10.1093/oso/9780198506720.001.0001.

[Gly90] P. W. Glynn. "Likelihood ratio gradient estimation for stochastic systems". In: *Communications of the ACM* 33.10 (1990), pp. 75–84. DOI: 10.1145/84537.84552.

[HJP24] K.-B. Huh, H.-S. Jeong, and J. F. Pedraza. "Spread complexity in saddle-dominated scrambling". In: *JHEP* 05, 137 (2024). DOI: 10.1007/JHEP05(2024)137. arXiv: 2312.12593.

[Iss18] L. Isserlis. "On a formula for the product-moment coefficient of any order of a normal frequency distribution in any number of variables". In: *Biometrika* 12.1–2 (1918), pp. 134–139. DOI: 10.1093/biomet/12.1-2.134.

[JV20] Y. Jia and J. J. M. Verbaarschot. "Spectral fluctuations in the Sachdev–Ye–Kitaev model". In: *JHEP* 07, 193 (2020). DOI: 10.1007/JHEP07(2020)193. arXiv: 1912.11923.

[LP17] G. Last and M. Penrose. *Lectures on the Poisson Process*. Cambridge: Cambridge University Press, 2017. DOI: 10.1017/9781316104477.

[LT25] A. Legramandi and N. Talwar. "The moments of the spectral form factor in SYK". In: *JHEP* 08, 108 (2025). DOI: 10.1007/JHEP08(2025)108. arXiv: 2412.18737.

[Maz69] P. Mazur. "Non-ergodicity of phase functions in certain systems". In: *Physica* 43 (1969), pp. 533–545. DOI: 10.1016/0031-8914(69)90185-2.

[Meh04] M. L. Mehta. *Random Matrices*. 3rd ed. Amsterdam: Elsevier/Academic Press, 2004.

[Mon+21] F. Monteiro, T. Micklitz, M. Tezuka, and A. Altland. "Minimal model of many-body localization". In: *Phys. Rev. Research* 3, 013023 (2021). DOI: 10.1103/PhysRevResearch.3.013023.

[Nan+22] D. K. Nandy, T. Čadež, B. Dietz, A. Andreanov, and D. Rosa. "Delayed thermalization in the mass-deformed Sachdev–Ye–Kitaev model". In: *Phys. Rev. B* 106, 245147 (2022). DOI: 10.1103/PhysRevB.106.245147. arXiv: 2206.08599.

[NRY18] T. Nosaka, D. Rosa, and J. Yoon. "The Thouless time for mass-deformed SYK". In: *JHEP* 09, 041 (2018). DOI: 10.1007/JHEP09(2018)041. arXiv: 1804.09934.

[Spe86] T. P. Speed. "Cumulants and partition lattices II: generalised k-statistics". In: *J. Austral. Math. Soc. Ser. A* 40.1 (1986), pp. 34–53. DOI: 10.1017/S1446788700026483.

[Suz71] M. Suzuki. "Ergodicity, constants of motion, and bounds for susceptibilities". In: *Physica* 51 (1971), pp. 277–291. DOI: 10.1016/0031-8914(71)90226-6.

[WJS20] M. Winer, S.-K. Jian, and B. Swingle. "Exponential ramp in the quadratic Sachdev–Ye–Kitaev model". In: *Phys. Rev. Lett.* 125, 250602 (2020). DOI: 10.1103/PhysRevLett.125.250602. arXiv: 2006.15152.

[YLX17] Y.-Z. You, A. W. W. Ludwig, and C. Xu. "Sachdev–Ye–Kitaev model and thermalization on the boundary of many-body localized fermionic symmetry-protected topological states". In: *Phys. Rev. B* 95, 115150 (2017). DOI: 10.1103/PhysRevB.95.115150. arXiv: 1602.06964.